technische universität
dortmund

Universitätsmedizin Essen
Westdeutsches
Protonentherapiezentrum (WPE)

# Determination of surface and skin dose in proton beam therapy

**Dissertation**
**zur Erlangung des akademischen Grades**
**Doktor der Naturwissenschaften**

vorgelegt von
Ajvar Kern
geboren in Semipalatinsk

Lehrstuhl für Experimentelle Physik IV
Fakultät Physik
Technische Universität Dortmund
2024

| | |
|---|---|
| Erstgutachter: | Prof. Dr. Kevin Kröninger |
| Zweitgutachter: | PD. Dr. Christian Bäumer |
| Prüfungsvorsitz: | Prof. Dr. Jan Kierfeld |
| Prüfungsbeisitz: | Dr. Michael Paulus |

Datum der Disputation: 28.10.2024

## Abstract

The basis for the application of proton therapy is the physical knowledge and thus the characterization of the proton beam with its depth dose distributions and the spot sizes for various energies. Together with a dose calibration, they form the basis of a beam model for the treatment planning system. The problem is, that the treatment planning system generally does not accurately calculate the first micro- and millimeters of the proton depth dose curve. Additionally, there is limited experimental data available for the superficial proton depth dose curve.
The skin is the largest human organ and is involved in every irradiation, which means, it is exposed to the risk of side effects and long-term damage. The aim is to determine the dose delivered to the depth of the skin in proton therapy.
In the first step of this thesis, the surface and skin dose of the depth dose curves is measured at various energies. In order to determine the dose in the skin depth in proton therapy, various detectors are used which are particularly suitable for shallow depth measurements. These include ionization chambers, thermoluminescence detectors and radiochromic films. In addition, the surface and skin doses are compared with a Monte Carlo simulation.
The second section of this thesis examines the skin dose from various clinical perspectives. There, the impact of different proton beam techniques, the energy-reducing block (range shifter) or the air gap between the proton beam exit (the nozzle) to the detector on the skin dose are discussed.

## Kurzfassung

Die Grundlage für die Anwendung der Protonentherapie ist das physikalische Wissen und damit die Charakterisierung des Protonenstrahls mit seinen Tiefendosisverteilungen und den Spotgrößen für verschiedene Energien. Sie bilden mit einer Dosiskalibrierung die Grundlage eines Strahlenmodells für das Bestrahlungsplanungssystem. Das Problem dabei ist, dass die ersten Mikro- und Millimeter der Protonen Tiefendosiskurve durch das Bestrahlungsplanungssystem ungenau berechnet werden und es generell nur wenige experimentelle Daten für die oberflächliche Protonen Tiefendosiskurve gibt.
Die Haut ist das größte menschliche Organ und ist bei jeder Bestrahlung involviert, wodurch diese auch dem Risiko von Nebenwirkungen und Langzeitschäden ausgesetzt ist. Ziel ist es, die Dosis in der Hauttiefe in der Protonentherapie zu spezifizieren.
Im ersten Schritt dieser Arbeit wird zunächst die Oberflächen- und Hautdosis der Tiefendosiskurven bei verschiedenen Energien vermessen. Um die Dosis in der Hauttiefe in der Protonentherapie zu spezifizieren, kommen verschiedene, besonders für geringe Eintrittstiefen geeignete, Detektoren zum Einsatz. Dazu zählen Ionisationskammern, Ther-

molumineszenzdetektoren und radiochromatische Filme. Zusätzlich werden die Oberflächen- und Hautdosen mit einer Monte Carlo Simulation verglichen.
Im zweiten Schritt der Arbeit wird die Hautdosis unter verschiedenen klinischen Aspekten betrachtet. So wird erörtert, welche Auswirkungen verschiedene Protonenstrahltechniken, ein energiereduzierender Block (Range Shifter) oder der Luftabstand zwischen Protonenstrahlausgang (der Nozzle) und dem Detektor auf die Hautdosis haben.

## Publications related to this work

- A. Kern, C. Bäumer, K. Kröninger, L. Mertens, B. Timmermann, J. Walbersloh and J. Wulff. Determination of surface dose in pencil beam scanning proton therapy. *Medical Physics*, 47(5):2277-2288, 2020.
- A. Kern, C. Bäumer, K. Kröninger, J. Wulff, B. Timmermann. Impact of air gap, range shifter and delivery technique on skin dose in proton therapy. *Medical Physics*, 48(2):831-840, 2021.

## Conference and colloquium contributions

- A. Kern, C. Bäumer, K. Kröninger, L. Mertens, B. Timmermann, J. Walbersloh und J. Wulff. Bestimmung der Oberflächendosis im Pencil-Beam-Scanning Modus in der Protonentherapie. 49th Annual Meeting of the DGMP, Nürnberg , Germany, 2018. Oral presentation.
- A. Kern, C. Bäumer, K. Kröninger, L. Mertens, B. Timmermann, J. Walbersloh and J. Wulff. Determination of surface dose in pencil beam scanning proton therapy. ESTRO 37, Mailand, Italy, 2019. Poster.
- A. Kern, C. Bäumer, K. Kröninger, L. Mertens, B. Timmermann, J. Walbersloh and J. Wulff. Determination of surface dose in pencil beam scanning proton therapy. Particle Colloquium, Essen, Germany, 2019. Oral presentation.
- A. Kern. Bestimmung der Hautdosis in der Protonentherapie. Particle Colloquium, Essen, Germany, 2020. Oral presentation.

## Thesis related to this work

- L. Mertens. Messung der in der Protonentherapie auftretenden Hautdosis mit Thermolumineszenzdosimetern. Master's thesis, TU Dortmund, 2018.
- A. Landmann. Untersuchungen zur Ermittlung der Hautdosis in der Protonentherapie mittels UV-Klebestreifen. Bachelor's thesis, TU Dortmund, 2019.

This dissertation is based on publications of partial results, which are indicated at the beginning of the respective chapters.

# Contents

# Chapter 1

# Introduction

Radiation therapy is one of various potential treatment modalities for malignant tumors, in addition to e.g. chemotherapy and surgery. The conventional type of treatment is the photon therapy. The younger area of radiation therapy is the proton therapy, where the number of proton facilities is further growing, with approx. 113 centers worldwide and many more under construction or in planning stage [1].
One advantage of proton therapy compared to photon therapy is the different depth dose distribution, which facilitates an optimal treatment volume coverage, while reducing the absorbed dose in the surrounding organs at risk. The skin is the biggest organ of a human and protects the internal organs against external influences. The basic structure of the skin can be taken from Figure 1.1. There are mainly three different skin layers. Located from the surface into the interior, they are called: Epidermis, dermis and subcutis. The Epidermis is containing the stratum corneum, which consists of several layers of dead cells that form the outermost layer. The flexibility of the skin results from the dermis, which locates the collagen fibres. The second task of the dermis is to supply the skin with blood and lymph vessels. The subcutis contains the fatty tissue, larger blood vessels and nerves. It is the last layer in front of the muscles. Figure 1.1 shows the basal cell layer (stratum germinativum), which lies between the epidermis and dermis. This layer is sensitive due to the stem cells, which are precursor of the corneum cells. The layer contains also the melanin, which defines the skin color and tanning [2, 3].

The first skin radiation damage was observed as a side effect of the first applied X-rays within the first months after the discovery by Wilhelm Konrad Roentgen [4, 5]. Since then a lot of literature was published for skin damage caused by irradiation, including treatments by X-rays or proton therapy. In order to quantify and predict possible radiation-induced skin reactions, an accurate skin dose determination is essential. In general, there is a lack of dosimetric data for very superficial dose determination in proton therapy, but more widely studied in photon therapy [6], [7], [8], [9], [10]. Superficial means in this context the scale of micrometer range, and in detail a skin dose depth definition of

70 $\mu$m water equivalent depth according recommendations of the international commissions ICRP 60 and ICRU 39 [2, 11]. The same depth of 70 $\mu$m is also used to define the depth of the basal cell layer, although humans have a variation of skin thickness based on gender, skin type and body region [12, 13, 14]. From the dosimetric point of view, the lack of data might be related to the limitations of the required equipment to measure in such narrow depths, e.g. at 70 $\mu$m. Further, treatment planning systems (TPS) are also limited, first in form of the resolution of the input of the computed tomography (CT) and magnetic resonance tomography (MRT) data, which are in the order of tenth of a millimeter, and second in the processing of the data by painting an organ or by calculating the dose distribution on the dose grid in order of 1 mm or higher.
The aim of this work is to investigate the proton surface depth dose distribution in the first micro- and millimeter range and to quantify the skin dose at the depth of 70 $\mu$m. Further, the skin dose is characterized in more detail in the context of technical and clinical characteristics. Various detectors and a Monte Carlo code are applied and compared to each other.

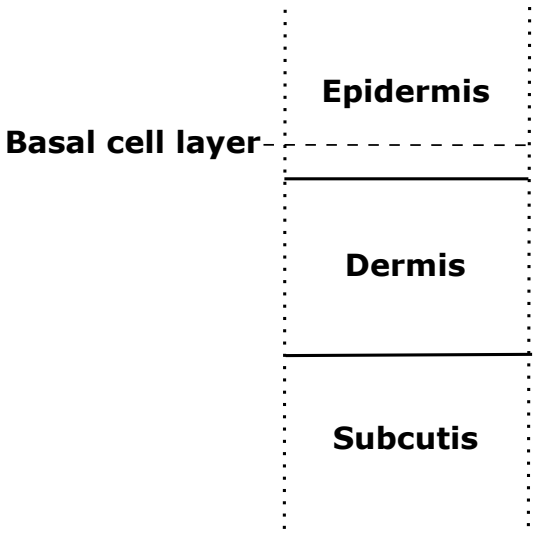


**Figure 1.1:** Simplified structure of the skin layers.

This thesis demonstrates: The theoretical backgrounds of the proton beam therapy and the here used detector physics. Further, the West German Proton Therapy Centre Essen (WPE) will be introduced where all measurements were performed and thus the components of a proton therapy system with the TPS. Chapter 3 presents the material and methods starting with the detectors used, which are in detail the ionization chambers, the thermoluminescence detector and the radiochromic films. This section will be completed by introducing TOPAS, a Monte Carlo simulation tool [15]. The next Chapter 4 is a pre-

liminary work chapter, where various preinvestigations for the three detector types and TOPAS are determined and presented. Chapter 5 summarizes the setup and the results for the determination of the surface and skin dose of pristine Bragg peaks. The following chapter introduces the impact on skin dose by applying and changing clinical parameters. With Chapter 7, a surface extrapolation factor was developed. The final Chapters 8 and 9 are containing the discussion and the summary and outlook of this work.
Parts of this dissertation were already published in Refs. [16, 17].

# Chapter 2

# Basic Principles Of Proton Beam Therapy

## 2.1 Physical Fundamentals

### 2.1.1 Proton Interactions In Matter

Matter is the basis for a physical body, e.g. that of a human being. A more precise description of matter is the definition as a mixture of nuclei and the electrons at rest [18]. The main types of interaction of protons in matter are with atomic electrons and with the atomic nucleus. A schematic representation of the interactions of protons is shown in Figure 2.1. The electromagnetic interaction occurs with free electrons, which is called inelastic coulomb scattering (Fig. 2.1 a)). The protons continuously lose kinetic energy and are slowed down. Because of the high mass of the protons compared to the electrons, the path is almost straight. Due to the minimal energy loss of the protons through the inelastic interaction, electrons are released by the ionized atom, which deposit their low kinetic energy locally [19]. Through the process of "stopping" the protons lose all their energy and stop in matter. Since the interactions have multiple discrete and random energy losses, the protons do not all stop at one depth. As a result of the range straggling, every monoenergetic field has an energy distribution, an energy straggling [20]. Figure 2.1 b) illustrates the elastic Coulomb scattering of proton and nucleus which is the main interaction with the nucleus. The increased mass of the nucleus deflects the protons from their previous trajectory [18]. Through the process of "scattering", also called multiple Coulomb scattering, all deflections of the protons result in an angular spread, which has an influence on the field width [20]. A third interaction involves the non-elastic nuclear reaction with a nucleus. The direct impact of the proton into the nucleus results in the emission of secondary particles such as protons, neutrons, deuterons, tritons or other heavier particles. This type of interaction occurs less frequently, about 20% of the protons, but it has an impact to the depth dose curve through the secondary particles [18, 19, 20].

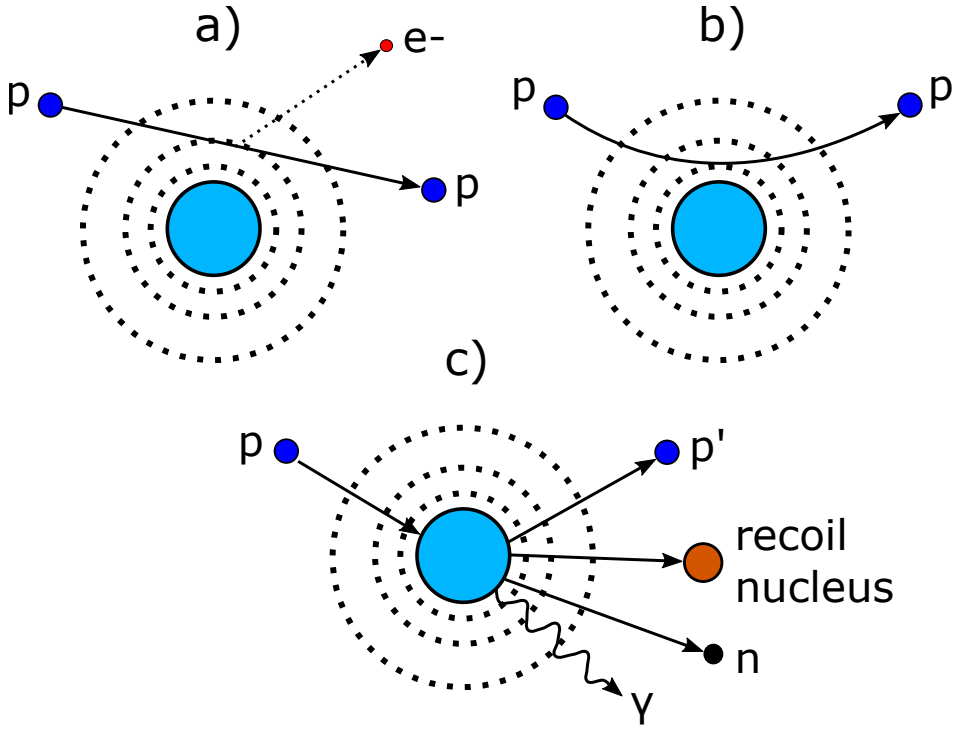


**Figure 2.1:** Schematic overview of the proton interactions: (a) inelastic Coulomb scattering with free electrons; (b) elastic Coulomb scattering with the nucleus; (c) non-elastic nuclear reactions. Reproduction according to Ref.[19].

### 2.1.2 Dosimetric Proton Basics

Assuming a beam of protons hits a material with a density $\rho$, e.g. a technical phantom or the human tissue. Then the proton beam will slow down until it stops. This kinetic energy loss $dE$ on the path $dx$ is the energy loss rate of ions, which is defined as the stopping power $S$:

$$S = -\frac{dE}{dx} \quad ; \quad \left[\frac{\text{MeV}}{\text{cm}}\right]. \tag{2.1}$$

More generally, and independent of the material, is the definition of the mass stopping power defined as

$$\frac{S}{\rho} = -\frac{dE}{\rho\, dx} \quad ; \quad \left[\frac{\text{MeV}}{\text{g/cm}^2}\right], \tag{2.2}$$

where $\rho$ (g/cm$^3$) describes the local density of the absorbing material. The theoretical fundamentals of stopping power for charged particles were given around 1933 by Bethe

[21] and Bloch [22] and are as follows

$$\frac{S}{\rho} = -\frac{dE}{\rho\, dx} = 4\pi N_A r_e^2 m_e c^2 \frac{Z}{A}\frac{z}{\beta^2}\left(ln\frac{2m_e c^2\gamma^2\beta^2}{I} - \beta^2 - \frac{\delta}{2} - \frac{C}{Z}\right) \quad , \tag{2.3}$$

with the variables:

| | | | |
|---|---|---|---|
| $N_A$ | = Avogadro's number | $r_e$ | = classical electron radius |
| $m_e$ | = mass of an electron | $c$ | = speed of light |
| $Z$ | = atomic number of absorbing material | $z$ | = charge of the projectile |
| $A$ | = atomic weight of absorbing material | $\beta$ | $= \frac{v}{c}$; with $v$ as velocity |
| $I$ | = mean excitation energy | $\gamma$ | $= \frac{1}{1-\beta^2}$ |
| $\delta$ | = density correction | $C$ | = shell correction . |

The last two terms of Eq. 2.3 add the relativistic theory and quantum mechanics [19]. In the case of protons, Eq. 2.3 will be translated to Eq. 2.4 by filling the physical constants and negligible the correction factors, because of the therapeutic energy range between 3-300 MeV of protons [20]. Here, the mass stopping power ratio for protons includes only the energy loss to free atomic electrons

$$\frac{S}{\rho} = -\frac{dE}{\rho\, dx} = 0.3072 \cdot \frac{Z}{A}\frac{1}{\beta^2}\left(ln\frac{W_m}{I} - \beta^2\right) \quad ; \qquad \left[\frac{\text{MeV}}{\text{g/cm}^2}\right], \tag{2.4}$$

where

$$W_m = \frac{2m_e c^2\beta^2}{1-\beta^2} \tag{2.5}$$

can be defined as the maximum energy $W_m$ of a secondary electron.
According to ICRU 85, the absorbed dose $D$ is expressed as the ratio of the mean local energy $d\bar{\epsilon}$ by ionizing radiation to a mass $dm$ with the density $\rho$ and the volume $dV$:

$$D = \frac{d\bar{\epsilon}}{dm} = \frac{1}{\rho}\cdot\frac{d\bar{\epsilon}}{dV} \quad ; \qquad [\text{Gy}]\,. \tag{2.6}$$

The absorbed dose is measured in Gray (Gy), where 1 Gy is equivalent to 1 J/kg [23]. A further calculation of the absorbed dose can be performed using the stopping power [20]. The formula is as follows

$$D = \Phi \times \frac{S}{\rho} \tag{2.7}$$

and contains the particle fluence $\Phi$, which represents the number of protons $dN$ crossing e.g. an area $dA$ [24]:

$$\Phi = \frac{dN}{dA} \quad ; \qquad \left[\frac{\text{protons}}{\text{cm}^2}\right]. \tag{2.8}$$

In other words, the dose can vary from point to point and depends on the number of particles and their energy loss.

### 2.1.3 Depth Dose Distribution

The visual representation of the stopping power is presented in a Bragg curve in Figure 2.2a). It can be divided into different regions. An important region for this work is the build-up region at the beginning of a Bragg curve.

- **Build-up region:** A first experimental observation of the build-up was made by Carlsson & Carlsson in 1977 [25]. The result was a smaller build-up than expected. The build-up region of a proton beam can be separated into an electronic build-up [26, 27] and a protonic build-up [28, 29]. The electronic build-up has a very short range and reaches approximately the order of 1 mm at an energy of 200.0 MeV [30]. As discussed in section 2.1.1, high-energy protons can release secondary electrons (delta rays) which can cause further ionization in the local tissue. The maximum transferred energy of a delta ray can be estimated by the proton energy. Thus, with the corresponding electron mass $m_e$, proton mass and energy $m_p$ and $E_p$, the following estimation is given

  $$E_e^{max} = 4\frac{m_e}{m_p}E_p \approx \frac{E_p}{500} \quad ; \qquad [\text{MeV}]\,, \tag{2.9}$$

  allowing a further estimation of the electron range [20]. It was noted that the build-up at low energies cannot always be observed [19]. This may happen when additional material is placed upstream a surface, for example an energy absorber or a patient mask, in which the electron equilibrium, i.e. the end of the build-up, is reached. Also an overlay with the protonic build-up is possible [25]. The main part of the protonic build-up consists of secondary protons and can reach several centimeters [28, 30, 31]. The secondary protons are generated from the non elastic nuclear interactions of protons with the nucleus, e.g. $^{16}$O(p,2p)$^{15}$N [32, 33]. Recent publications by Kelleter et al. [30] and Pfuhl et al. [31] separated the two build-ups with Monte Carlo simulations and measurements. A similar term for the protonic build-up is the nuclear build-up.
  In contrast, there is only an electronic build-up visible for a photon depth dose

curve, which is more long-ranged and enabling the skin sparing (compare Figure 2.2 b)) [34].

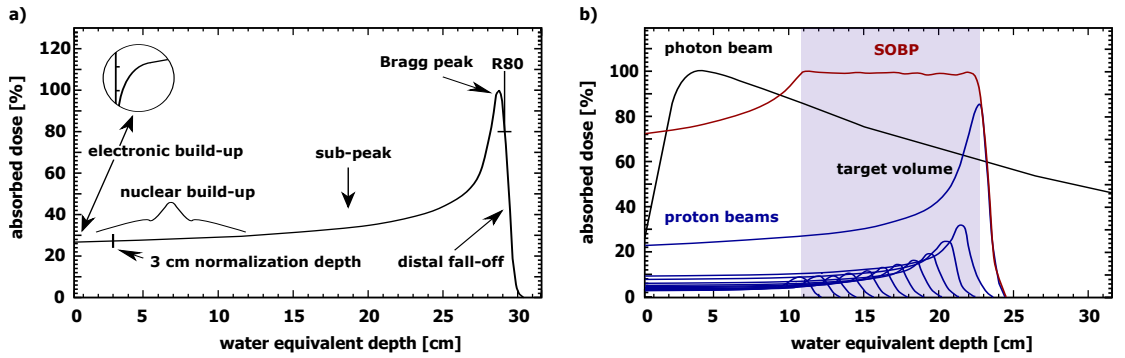


**Figure 2.2:** (a) Depth dose curve of a pristine, monoenergetic proton beam in water (reproduction according Ref. [19]). The characteristic depth dose curve is common for protons and other heavy charged particles: a low entrance dose including a build-up up to the Bragg peak, where the entire dose is deposited within a few millimeters. (b) Depth dose curve of a spread-out Bragg peak (SOBP, reproduction according Ref. [35]). A SOBP (red) can be formed by a certain number of modulated and weighted Bragg peaks (blue) of various energies and cover a target volume. In contrast to the proton beam, the photon beam (black) shows a continuous dose deposition in depth and allows less protection of healthy tissue.

- **Sub-peak region:** This region between the build-up and proximal of the peak is the result of various physical processes. These include: A $1/v^2$ dependence of the proton stopping power, the reduction of secondary protons or the release of further secondary particles by the nuclear interactions, and for very small fields a reduction of the proton fluence on the central axis as a result of the missing equilibrium of lateral multiple Coulomb scattering [19].

- **Bragg peak:** The Bragg peak is the dose maximum of the depth dose curve of charged particles or protons. At the end of the Bragg peak the stopping power increases strongly and the protons reach a velocity of $v$=0 m/s. They are completely absorbed in the medium. Figure 2.2 a) shows a certain peak width, that means, that not all particles stop at the same depth. Instead, they have small variations in range. The so-called range struggling or energy smearing is attributed to the scattering processes and is more pronounced for higher energies (Figure 2.3). An important dosimetric quantity is $R80$, which is the range at a dose of 80%. It describes the mean projected range of a proton and therefore the range at which 50% of the protons have stopped [24, 36, 37].

- **Distal fall-off region:** This distal course of a Bragg peak is used for the potential protection of organs at risk in proton therapy. It is a contribution of range struggling

and changes only slightly for various materials [38]. The energy width also depends on the facility, i.e. the respective energy selection system [39].

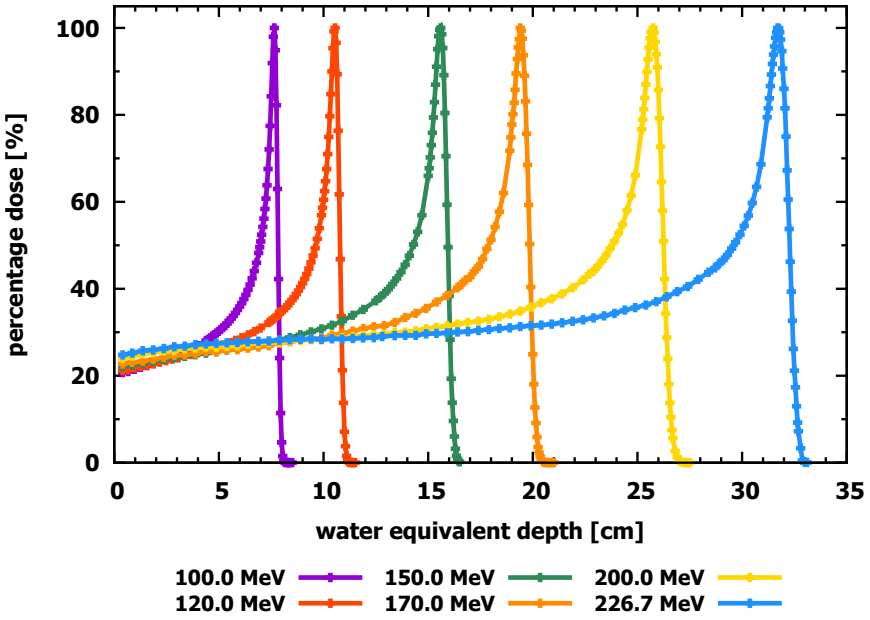


**Figure 2.3:** Measured pristine Bragg peaks in a water tank at the West German Proton Therapy Centre Essen. From left to right one can see the quasi-monoenergetic fields of 100.0 MeV, 120.0 MeV, 150.0 MeV, 170.0 MeV, 200.0 MeV and 226.7 MeV. The width of the Bragg peak becomes wider for higher energies and the peak to plateau ratio decreases, as a result of the scattering process and the contamination of the secondary particles. The data was recorded at WPE.

In a clinical application a single Bragg peak is not sufficient to cover a tumor or a treating volume homogeneously. Therefore, a so-called spread-out Bragg peak (SOBP) is required. The SOBP is modulated by several proton energies consisting of various intensities and weightings. Figure 2.2 b) depicts a modulated SOBP with pristine Bragg peaks. A more detailed description, as well as an analytical method about the modeling of a SOBP can be found in Ref. [40, 41]. The energy-range relationship serves as basis for this modeling [42]:

$$R \approx a \cdot E^b = 0.00244 \cdot E^{1.75} \quad ; \qquad \left[\frac{\mathrm{g}}{\mathrm{cm}^2}\right]. \tag{2.10}$$

The applied values are used to determine the range in water for the energies 100-200 MeV.

- **Photon depth dose**: The build-up effect of the photon beam is long-ranged and much greater and more visible than the build-up effect of protons. A comparison

between the two build-up effects is shown in Figure 2.2 a) and b). Typical clinical photon beams are 6 MV, 10 MV and 15 MV, respectively. A higher energy provides a longer build-up effect. This can be attributed to the secondary electrons liberated by the ionization. The energy transferred to the electrons lies in the MeV range and corresponds to a range of several millimeters. With increasing photon energy, the forward scattering of secondary electrons in the beam direction increases (Compton effect). Therefore, the dominant interaction of photons in this energy range is the Compton effect, which is defined as the inelastic scattering of a photon by an atomic electron. The dose maximum is the result of the secondary electrons, where the same number of secondary electrons are released as are stopped [24].

## 2.2 Detector Physics

### 2.2.1 Ionization Chamber

Ionization chambers (IC) are one of the most important and widely used types of detectors for dosimetry. This is due to their simple design, easy handling and the well studied physical functionality.
The simplest configuration of an IC is an electrical charged plate capacitor. As shown in Figure 2.4 a), two plane parallel metallic plates (electrodes: anode and cathode) are supplied by a voltage source. There is an enclosed gas between the electrodes, which often consists of air [24]. As already observed by C.W. Röntgen, the air is ionized by external irradiation [43]. In a primary ionization, negative charged electrons and positive charged ions are created according to the reaction

$$X + p \rightarrow X^{+} + p + e^{-} \tag{2.11}$$

with $X$ and $p$ defined as atom and loaded particle respectively [44]. The applied voltage produces an electric field between the electrodes. For a parallel plate chamber as shown in Figure 2.4, the electric field $\vec{E}$ is defined by the voltage $U$ and the plate spacing $d$:

$$\vec{E} = \frac{U}{d} \tag{2.12}$$

The field lines apply from the positive anode to the negative cathode. In an optimum case, the electron-ion pairs are collected without loss and accelerated according to their opposite polarity. The charge or the current can be read out with an electrometer [45].
It is important to choose the appropriate chamber with regard to design and size in the respective radiation field as well as the choice of voltage. The charge or current depends on the selected chamber voltage. The current/charge-voltage characteristics are classified

with increasing voltage into the following regions: Recombination, ion saturation (operational range of an ionization chamber), proportional counter and Geiger-Müller counter.

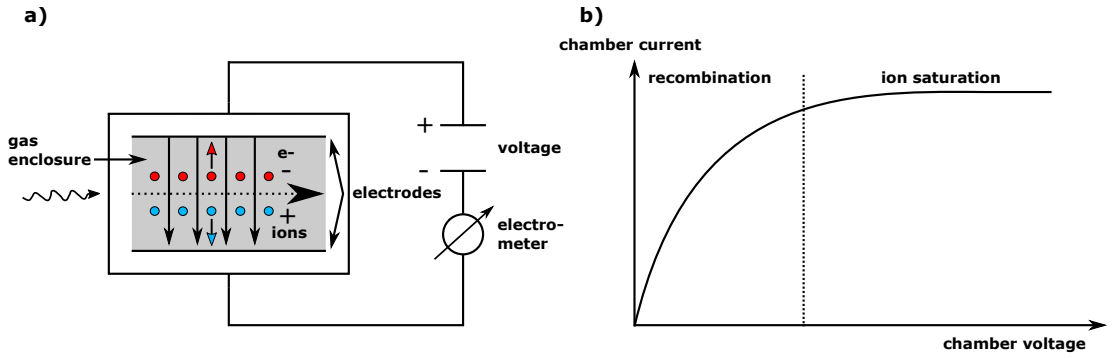


**Figure 2.4:** (a) Basic elements of a conventional ionization chamber. The setup consists of a voltage source, a readout device e.g. an electrometer and the ionization chamber. The gas volume enclosed within the chamber is surrounded by two metal electrodes. Through ionization, positive (ions) and negative (electrons) charges are created, which are attracted by the electric field to the opposite electric charge of the electrode. (b) Current-voltage diagram. Chambers which operate in the ion saturation region are called ionization chambers. Most electron-ion pairs are collected in this region (reproduction according Ref. [24]).

To achieve reproducible and almost loss-free measuring results, ionization chambers must be operated in the ion saturation region at their working voltage. This range is shown in Figure 2.4 b) as the asymptotic saturation of the current. With respect to Figure 2.4 a), almost all electron-ion pairs are collected by the applied chamber voltage. Chambers which operate in the ion saturation region are called ionization chambers (IC). The effect of a small applied voltage is a weak electric field and the charges are slowly accelerated to the electrodes accordingly. This allows many electron-ion pairs to recombine, which means that the charge is neutralized and the count is lost (Figure 2.4). Gas amplification occurs at higher voltages. It does not remain at primary ionizations, but then further secondary ionizations occur.
The IC's are used in a variety of designs, for example, parallel plate chambers, cylinder- or thimble chambers and spherical chambers. In clinical dosimetry mainly thimble and parallel plates IC's are applied. There are code of practice protocols for calculating the absorbed dose, such as the IAEA TRS-398 or the ICRU 78 for protons [46, 47]. The calculation of the absorbed dose $D_{w,Q}$ in water ($w$) for a proton beam with the beam quality $Q$ can be calculated under reference conditions with the formula as follows:

$$D_{w,Q} = M_Q \cdot N_{D,w,Q_0} \cdot k_{Q,Q_0} \quad . \tag{2.13}$$

$M_Q$ is the reading of the electrometer corrected by some further correction factors such as temperature and pressure or electrometer calibration. $N_{D,w,Q_0}$ is an individual chamber calibration factor, which is determined according to a defined absorbed dose at the reference quality $Q_0$ e.g. in $^{60}Co$ (cobalt-60). The correction between the beam qualities $Q_0$ and $Q$ is given by $k_{Q,Q_0}$ [46].
Further information and more theory on how to determine the absorbed dose can be found in the recommended protocols [46, 47].

### 2.2.2 Thermoluminescence

The effect of luminescence is divided into the subgroups of fluorescence, delayed fluorescence and phosphorescence. The common characteristic is the external excitation by some means. Only the duration and the emission spectrum are varying. A prompt emission of visible radiation occurs by fluorescence. A much slower emitting and a longer wavelength light is called phosphorescence. The delayed fluorescence exhibits a longer emission time with the same emission spectrum [45]. Thermoluminescence is a special mechanism and can be assigned to phosphorescence due to the delayed emission.
Thermoluminescence is based on light emission after a doped insulator or semiconductor is irradiated and then heated. The phenomenon can be explained with the one-trap-one-recombination-center model in the band model [48]. Figure 2.5 sketches the important valence band and the conduction band in the band model for the explanation. The valence band is the highest occupied energy band and is filled with electrons in insulators and semiconductors. The conduction band is in contrast empty. In between there is a band gap which the electrons are able to overcome when the material is irradiated, i.e. by supplying energy. The energy difference must correspond to the energy difference between the two bands. In the conduction band, the electrons can move freely and return to the ground state (valence band). However, the result is no thermoluminescence. The effect can only occur if there are defects in the material, so-called traps in the usually pure material (see traps between the bands in Fig. 2.5). This allows the electrons and the holes to be bound by the traps between the two bands [45].
In this work lithium fluoride is doped with magnesium and titanium (written as: LiF:Mg, Ti). This leads to traps for the electrons induced by magnesium and recombination centers for the holes induced by titanium [49].
When ionizing radiation with an energy greater than the band gap of 13.6 eV is deposited in LiF, an electron hole pair is created [49]. The electrons reach the conduction band where they can move freely. The same applies to the holes in the valence band. On the one hand, the electron can return directly, recombine with a hole and the released energy is emitted by a photon. On the other hand, Figure 2.5 a) shows how the electrons are bound in the traps and the holes in the recombination centers. With external energy in

form of heat, the trapped electrons can be released from the traps. The electrons return to the conduction band, where they are again free to move and fall back into the valence band. As sketched in Figure 2.5 b), the holes are located in their recombination center and can recombine with the incoming electrons, which leads to the emission of light. By the application of heat this process is called thermoluminescence [50].

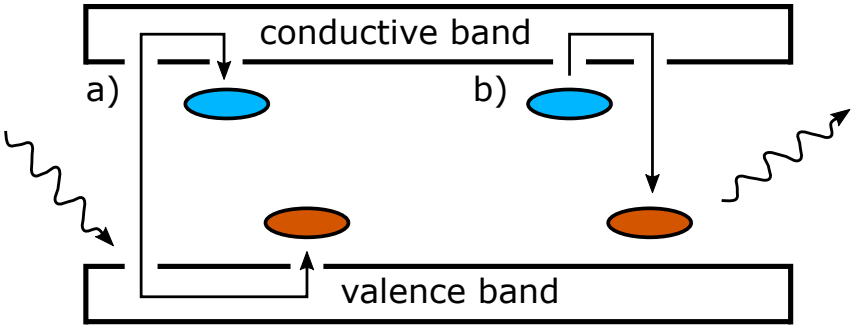


**Figure 2.5:** Sketch of the one-trap-one-recombination-center model between the valence band (bottom) and the conduction band (top). The colors blue and brown show the traps for the electrons and the holes. a) The external irradiation induces an electron-hole pair, which is caught by the traps. b) The thermoluminescence light is emitted by the released electron from its trap and the recombination with the hole. Reproduction according Ref. [51].

### 2.2.3 Chemical Detector

With the application of chemical detectors ionizing radiation can be detected by a chemical reaction. There are a number of chemical detectors available such as discoloration caused by a substance dissolved by oxidation, color and transparency changes of inorganic substances like crystals or glasses as well as polymerization processes with a change in absorption behavior [24]. The last-mentioned will be introduced in more detail.

- **Radiochromic film:** Radiochromic films are based on diacetylene, an unsaturated hydrocarbon compound. The effect of ionizing radiation causes a polymerization, i.e. a synthesis reaction of the individual hydrocarbon compounds and polydiacetylene is formed. The radiochromic films turn bluish in color and show a largely dose-proportional absorption behavior in the visible wavelength range (approx. 500-700 nm). The advantage of this type of chemical detectors is an easy handling under

normal room light and they do not require any further manual chemical processing [24, 52].

## 2.3 Proton Beam Therapy System at West German Proton Therapy Centre Essen

The West German Proton Therapy Centre Essen (WPE) has installed an IBA (Ion Beam Applications, Louvain-la-Neuve, Belgium) Proteus® Plus proton therapy system. Next to the Cyclotron, the WPE has four treatment rooms. The first room has a two-part solution: a 90° fixed horizontal beam line and a further 90° eye line. The three additional treatment rooms are equipped with a 360° rotating isocentric gantry. An overview of the design of the entire proton therapy system and the corresponding rooms from left to right is shown in Figure 2.6.

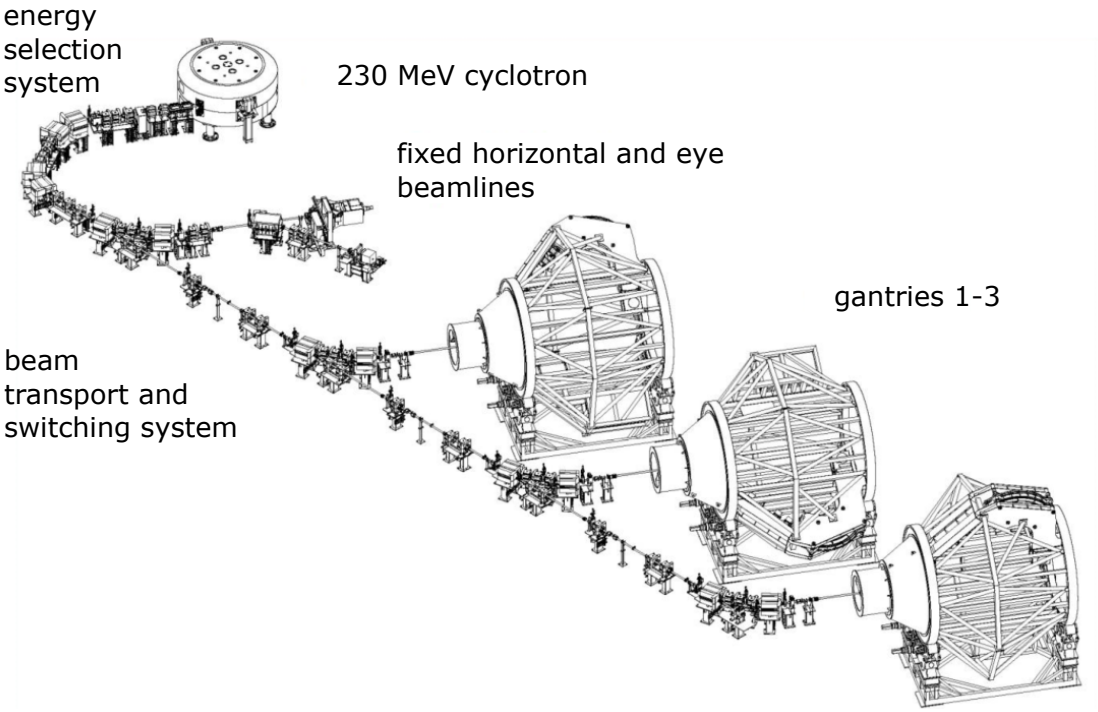


**Figure 2.6:** The IBA proton therapy system at WPE. The layout shows from top to bottom: the cyclotron, the energy selection system, the beam transport and switching system with its dipoles and quadrupoles, the 90° fixed beam treatment room including the eye line and the three 360° gantry treatment rooms [53].

### 2.3.1 Components Of A Proton System

#### Isochronous Cyclotron

The isochronous cyclotron at WPE can generate a maximum clinical energy of 226.7 MeV at isocenter. The minimum clinical energies of 100.0 MeV or 82.5 MeV for the eye treatment room [54] are achieved by degrading the energy within the energy selection system, which has the shape of a wheel-mounted wedge. In general, an isochronous cyclotron consists of the following components: A radio frequency (RF) system, a strong magnet, a proton source and an extraction system [55].
The protons are produced in the center of the cyclotron by the so-called Penning effect. The H2 gas is enclosed between a heated and unheated cathode and a hollow anode with an exit window. Electrons are generated by the heated cathode, which ionize the gas and a plasma is formed. The design is optimized to achieve a very high ion yield. The extraction is done by an extraction anode with a negative potential [56].
The isochronous cyclotron has a continuous beam character, also known as continuous wave. The difference to the classical cyclotron is an increase of the radial magnetic field change $B(r)$ to compensate the relativistic mass increase $m(r)$. The term isochronous gives an indication of a constant orbital period. The following equation describes the cyclotron frequency:

$$\omega = \frac{qB(r)}{m(r)} = \text{constant.} \tag{2.14}$$

To ensure that the particle trajectories are always focused, the poles are azimuthally segmented and divided into so-called valleys and hills. The valleys correspond to a weaker and the hills to a stronger magnetic field. Thus, axial defocusing can be avoided by the increasing radial magnetic field. The dees of the RF system are usually placed in the valleys. The protons are electrostatically deflected in their longest turn by a deflector [55, 57].

#### Beam Transport

After extraction of the protons, the beam transport takes place in a vacuum tube. As mentioned before, depending on the beam requirements, the energy of the proton beam will be degraded. This is done in the energy selection system (Figure 2.6). In addition to the wheel-mounted wedge with its varying thickness, a magnetic analyzer and an energy slit are installed in the beam path. The interaction with the degrader causes angular scattering and energy blur. The energy selection system therefore extracts the protons that do not have the corresponding proton trajectory and energy sharpness $\Delta E$. Both

parameters have an influence on the dose rate and the protons depth dose curve [56]. Further transport to the treatment rooms is supported by dipole and quadrupole magnets. The former ones are responsible for bending and the latter ones for focusing the proton beam [57].

### 2.3.2 Nozzle

The last part of the beam transport system at the end of the beam line is called nozzle. The nozzle contains all components for the individual delivery technique. IBA distinguishes between a dedicated pencil beam nozzle and a universal nozzle. The nozzles are located in the rotating 360° gantry or are mounted horizontally (fixed beam treatment room).
At WPE there are two dedicated pencil beam nozzles and two universal nozzles. All three available delivery techniques pencil beam scanning (PBS), uniform scanning (US) and double scattering (DS) can be applied at the universal nozzle.

### 2.3.3 Beam Delivery Techniques

The proton beam coming from the beam line is a pencil beam and has to be shaped laterally and longitudinally in the nozzle in order to irradiate a 3D volume. The aim is to create an SOBP of several individual modulated Bragg peaks as shown in Figure 2.2. This works slightly different for each technique and is described in the following subsections for the three beam delivery techniques PBS, US and DS. A distinction is made between two types of nozzles. A dedicated PBS nozzle (Figure 2.8 b)), which was developed especially for the PBS technique, and a universal nozzle (Figure 2.8 a)), where all three techniques can be applied.

#### Double Scattering

Double Scattering (DS) is a passive method of spreading a narrow beam using scattering elements. At WPE, it consists of a pair of scatterer called primary and secondary scatterers, see Figure 2.7 upper drawing. The aim is to provide an appropriate spread and a uniform beam to irradiate the whole target volume [24]. The primary scatterer, also known as a flat scatterer, is made of a high-Z material (Z = atomic number) and is manufactured from lead. The high-Z material has the largest amount of scattering (multiple Coulomb scattering) with the smallest energy loss [58]. Due to the strong scattering, the narrow proton beam is broadened to a Gaussian profile. With an additional aperture, the so-called single scattering can be applied. This technique is mainly used in ocular

treatment because of the small field sizes and the sharp penumbra [54, 59, 60].
For a larger homogeneous field size a contoured scatterer is required. As shown in Figure 2.7, the second scatterer consists of two materials, a combination of a central inner high-Z material and an outer low-Z material. The parabolic design of the thicker high-Z material spreads more protons laterally. The result is a homogeneous dose distribution in the isocenter.
Figure 2.7 illustrates an additional beam forming component located between the scattering elements. The beam modulation of a SOBP is generated with a continuously rotating range modulator wheel (RMW) to obtain several Bragg peaks of various depths [61]. A step (layer thickness) in the RMW corresponds to a Bragg peak and a sequential irradiation of these various steps is performed. The rotation frequency of the RMW is 10 Hz. A RMW has various thicknesses and materials. The materials can be low-Z materials like Lexan, carbon, aluminum or a high-Z material like lead. The low-Z materials are intended to reduce the scattering of the beam. An RMW built by IBA consists of three different tracks (modulator pattern), which are selected by moving the RMW to the correct track position. To cover as many combinations of range and modulation as possible, there is a so-called multiple energy modulator consisting of three RMWs. Eight of the nine tracks are used for DS. One track with constant step thickness and positioning is reserved for US and works as a variable range shifter (RS) [58].

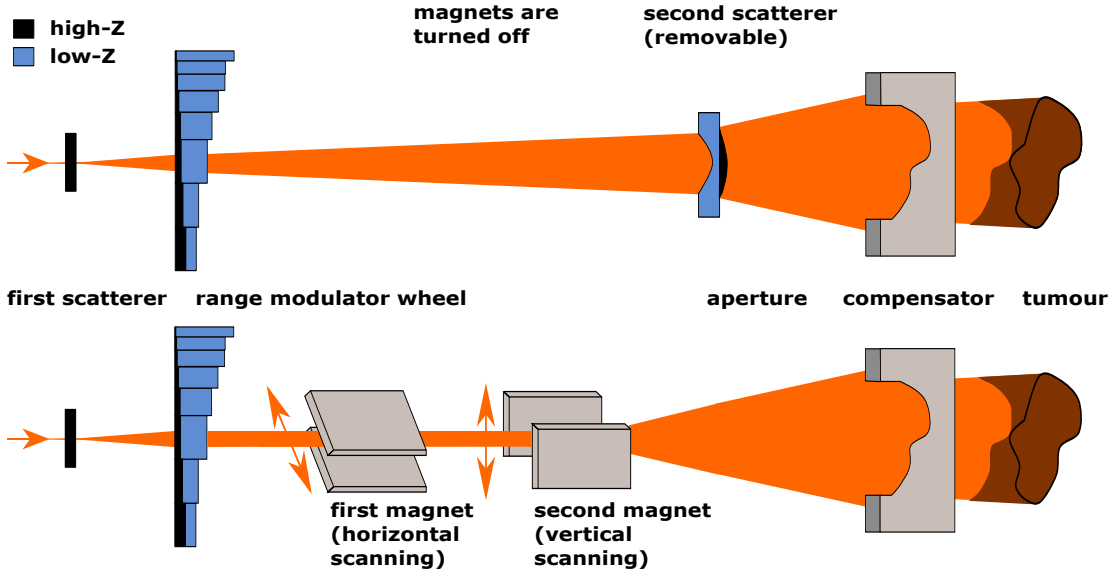


**Figure 2.7:** Schematic illustration of double scattering and uniform scanning. Both techniques are delivered with the universal nozzle. The upper illustration shows the double scattering mode. As the name suggests, two scatterers are required, the first and second scatterer (contoured scatterer). In uniform scanning mode, the second scatterer is extended and the scanning magnets are turned on. Uniform dose delivery is performed according to a defined scan pattern. Reproduction according to Ref [35].

To obtain a flat SOBP for a specific energy further aspects have to be considered. The scattering power for each step of the RMW must be equal. If not and combined with a long drift distance to the isocenter, the results are fluence changes in the isocenter. One way to compensate the scattering power is to introduce a scatter-compensated wheel by high-Z material steps. Another option is to fine-tune the beam current as a function of RMW position to adjust the number of protons hitting a RMW step [58].
Patient-specific apertures and range compensators are mounted on the so-called snout. A snout is available in various diameters. The snout can be moved along the beam axis and the mounted components are the last two beam elements of the nozzle in front of the patient (see Figs. 2.7, 2.8). Due to proton scattering, one tries to bring the aperture and the range compensator close to the patient as possible. A larger air gap leads to an increase in the lateral penumbra.
An aperture is made of brass (high-Z material) and is designed to define the proton field in lateral direction in beam's eye view. Since the aperture shape represents a 2D projection of the target volume including the safety margin, a separate aperture is required for each field. The passive scattering elements in nozzle and snout, such as the aperture or the scatterer, lead to the production of unwanted dose contributions from neutrons [62, 63].
The range compensators, made of polymethyl methacrylate (PMMA), are located behind the aperture. The individual compensator pixels reduce the distal range of the protons and provide an adaptation of the depth variation within the calculated interaction path. PMMA material is added or removed accordingly to adjust the distal SOPB end. A unique compensator is milled for each field and patient.

#### Uniform Scanning

In addition to DS, the US delivery technique is implemented in the universal nozzle. However, not all components of DS are used, see Figure 2.7. US is a combination of a passive (DS) and an active (PBS) proton delivery technique.
The interaction at the beginning of the nozzle is similar to DS. The beam hits the first scatterer where the beam broadens to the desired spot size. As mentioned in subsection *Double Scattering*, a track with constant step thickness and positioning in the RMW exists only for US. Therefore, the RMW operates as an energy degrader for US. Like in PBS, energy layers do exist for a SOBP. The difference to PBS is a uniform dose of the layer. This is achieved by the two scanning magnets inside the universal nozzle. The scanning algorithm delivers with constant frequency a zigzag pattern, which is nearly rectangular [64, 65]. Due to the rectangular scan area and the uniform dose, an aperture and a compensator are required again. They are inserted into the snout like in DS and are used for lateral and distal field adaption. In US, larger field sizes as well as higher

proton ranges can be applied without problems. This is because the efficiency of the system is increased with less scattering material than with DS.

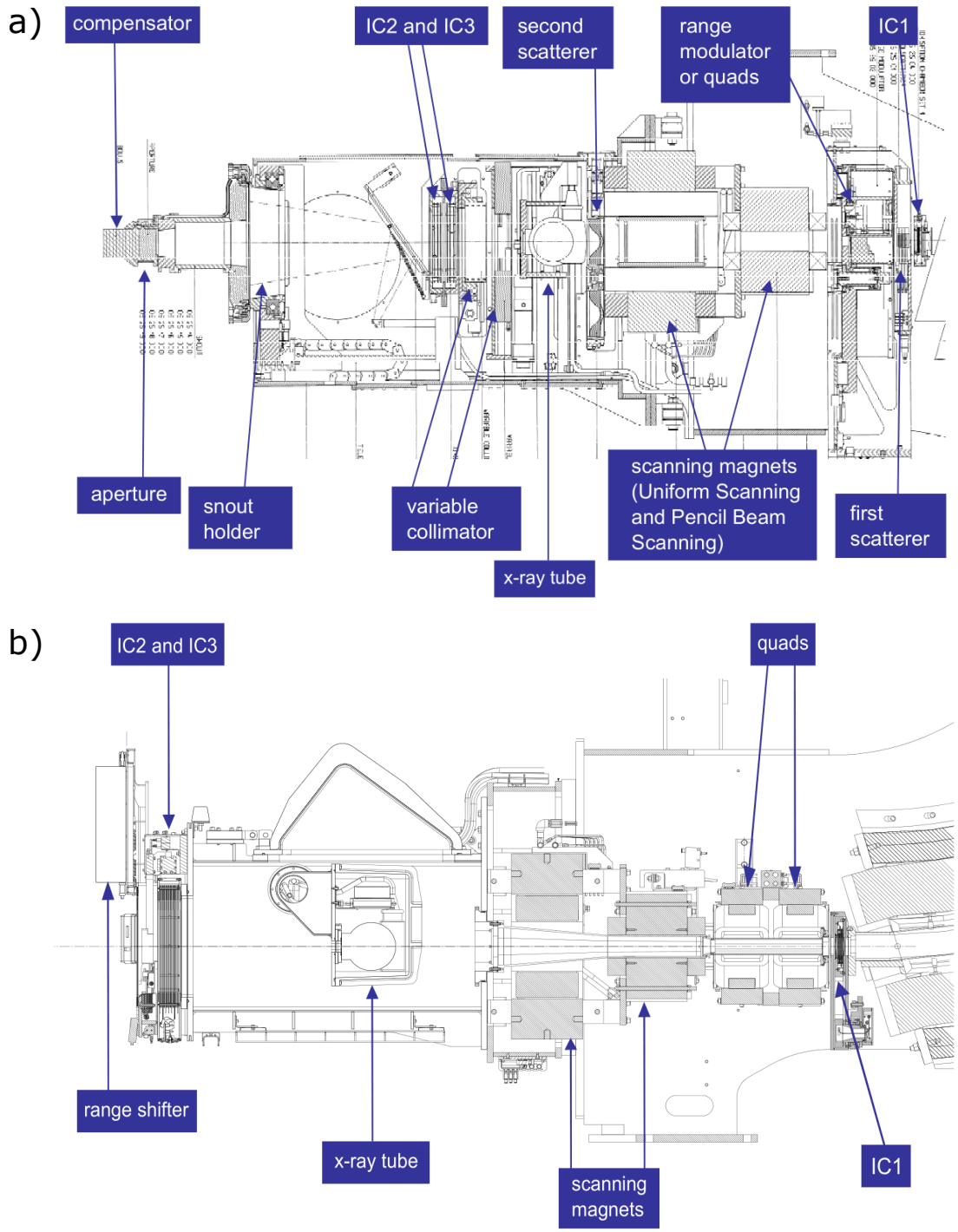


**Figure 2.8:** Technical drawings of the IBA nozzles. a) Universal nozzle supporting the delivery techniques uniform scanning (US), double scattering (DS) and pencil beam scanning (PBS). b) Dedicated pencil beam scanning nozzle. A detailed description of the various components can be found in the subsection 2.3.3.

### Pencil Beam Scanning

The latest of the three delivery techniques is the PBS with the associated PBS dedicated nozzle. A technical drawing is shown in Figure 2.8 b). With regard to the universal nozzle, the PBS dedicated nozzle was designed in order to keep the scatter and therefore the production of secondary particles low.
The following components are located inside the nozzle, starting from the beginning to the exit: IC1, quadrupole magnets (quads), scanning magnets, x-ray tube, IC2/3 and a movable range shifter. The ICs are responsible for monitoring the beam. In IC1, the centering of the beam is checked, in IC2/3 a more precise sampling of the position and thus the size and shape of the pencil beam as well as the dose in monitor units are determined. A detailed design of the two 320 mm x 320 mm parallel plate ionization chambers (IC2/3) consisting of Mylar® foils can be found in Courtois et al. which were also applied for the dedicated nozzles at WPE [66]. The magnets are used to focus the beam (quads) and to scan in lateral direction (dipoles). One of two x-ray tubes is located inside the nozzle and can be retracted as needed to provide images in beams eye view. At WPE, there are three different range shifter (RS) in various thicknesses (RS25, RS51, RS74 with the number as water equivalent thickness in mm) to pull back the proton beam, when treating tumors close to the surface. The scanning is performed in discrete steps as spot scanning (see Figure 2.9) [67]. The intensity of a spot is defined by the dwell time. This means the dose per spot increases when the beam spends more time in a spot. As outlined in Figure 2.10, a volume is enclosed from back to front with the single energy layers. The first layer is scanned laterally with the most distal range (highest energy). This is done in the y-direction until all required spots in a row have been scanned. Then, the next row is changed in x-direction. After finishing the layer, the energy degrader switches to the next lower energy and the lateral scan process is repeated. The result is an irradiation of a 3D volume with a SOBP as shown in Figure 2.2b).

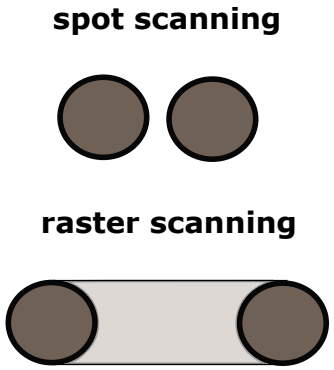


**Figure 2.9:** Two scanning modes in pencil beam scanning. The upper one shows the step and shot method. The system emits a spot, interrupts and moves on to emit the next spot (step and shot mode, spot scanning). Below is the raster mode. The spot is scanned continuously, there are no interruptions between the spots (raster scanning).

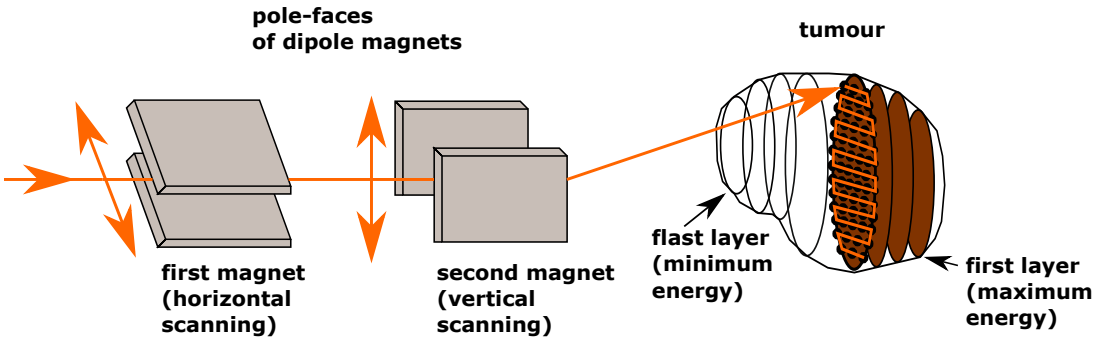


**Figure 2.10:** Schematic illustration of the PBS technique. The scanning of an energy layer is performed with two dipoles for the x- and y-direction. The energy degrader adjusts the energy or range in a volume. Reproduction according to Ref [68].

In PBS, there are further clinical properties like spot size, spot spacing, spot weight and energy spacing. The distribution of the particles is statistical and describes the physical parameters position and angle (2D phase space) as Gaussian distribution [69]. The spot size as beam sigma ($\sigma_{x,y}$) of a proton beam is therefore described by the Gaussian shape and is defined by the full-width at half maximum. Magnitudes of spot sizes are shown in Table 2.1. The lowest energy of 100.0 MeV has a $\sigma_{x,y}$ of approx. 5.43 mm and for the maximum energy approx 2.72 mm at isocenter. The spot spacing describes how close two spots are positioned to each other. A lower spot spacing may be suitable for small volumes. The clinical parameter for spot intensity is the spot weight. In the clinical range, 0.02 MU to 8 MU per spot are used. The energy spacing describes the distance between two consecutive energies or Bragg peaks. The ranges for R80 for the corresponding energies are listed in Table 2.1.

| Energy | Spot size $\sigma_{x,y}$ [mm] | R80 [mm] |
|---|---|---|
| 100.0 | 5.43 | 77.06 |
| 120.0 | 4.67 | 106.82 |
| 150.0 | 3.92 | 157.92 |
| 170.0 | 3.65 | 196.64 |
| 200.0 | 3.10 | 259.63 |
| 226.7 | 2.72 | 322.29 |

**Table 2.1:** Beam data for clinical beams at WPE.

## 2.4 Treatment Planning System

The treatment planning system (TPS) together with a care management software provide the basis for patient management and treatment planning. At WPE, RayStation from RaySearch (RaySearch Laboratories AB, Stockholm, Sweden) is clinically used for patient treatment planning. The TPS is very powerful and provides all common dose engines for photon, electron, proton and carbon ion treatment planning.
The following Figure 2.11 sketches four essential work steps within the TPS. It includes: 1.) computed tomography (CT)/ magnetic resonance imaging (MRI); 2.) contouring; 3.) physical planning; 4.) quality assurance (QA).

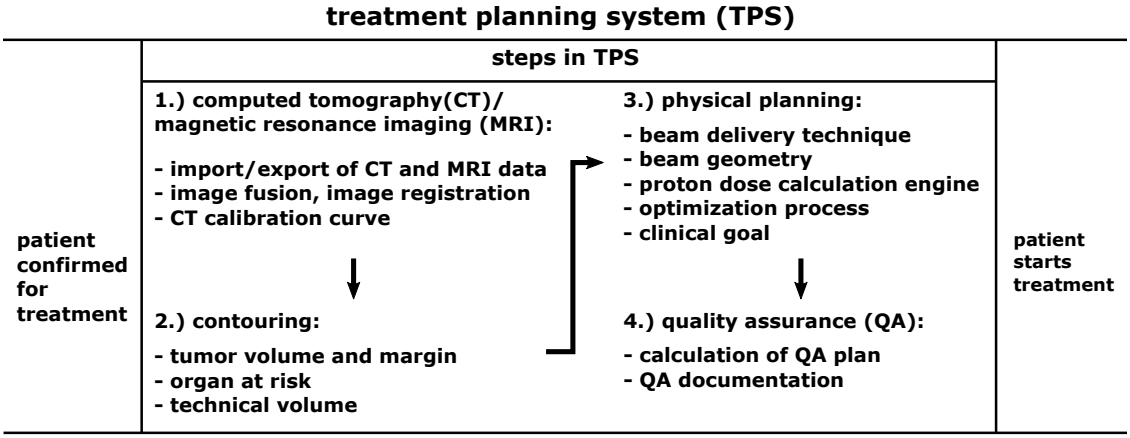


**Figure 2.11:** Sketch of the main work steps in TPS after patient is confirmed for treatment: 1.) computed tomography (CT)/ magnetic resonance imaging (MRI); 2.) contouring; 3.) physical planning; 4.) quality assurance (QA). The processing of the steps are performed by doctors and physicists. The following tasks from the sketch are handled by physicists: Import/export of CT and MRI data, selecting the calibration curve (1.)), contouring of technical volumes (2.)) as well as the steps in 3.) and 4.)

A first impression of treatment planning with some clinical parameters is provided by step 3, which will be presented in more detail in the following subchapter.

### 2.4.1 Physical Planning

At the beginning, doctors are contouring the tumor volume with the associated safety margins and organs at risk based on CT and MRI images. Tumor volumes are usually defined in radiotherapy according to the international ICRU report as gross tumor volume (GTV), clinical tumor volume (CTV) and planning target volume (PTV) [47, 70, 71].
When selecting the proton delivery technique, the tumor localization is evaluated. In

many cases, the PBS technique is used, which concerns the head as well as the pelvic region of a patient. The US technique can be used in patients where sparing of an organ at risk with direct tumor localization is required. The sharp field definition by the aperture is also useful for very small field geometries. Thus, a sharper lateral penumbra is achieved for US and DS compared to the PBS technique. The lateral penumbra is defined as the 80-20% dose fall-off of the beam profile in beams eye view direction [72]. If the tumor volume is in a region of motion, such as the thorax, the DS or PBS technique can be applied [73, 74, 75]. The continuous and complete irradiation of a target volume in DS can deliver a lot of dose within a short time.
After the choice of delivery technique, the next step is to define the beam geometry. The number of fields depends on the tumor extension and location. Typically, between 2-5 proton fields are required to achieve a suitable uniform dose coverage and robustness with respect to translation and density. Due to the rotating gantry, a variety of angles can be approached. But the collision between the nozzle and snout with a patient must be avoided. This is particularly the case if an extendable snout or extended RS is present. There are also nozzles that are designed to operate at a fixed distance. During planning, the aim is to achieve the shortest possible air gap between the snout with the beam-modifying accessory and the patient, so that an appropriate minimal lateral penumbra can be obtained. The location of the tumor also affects the choice of the proton energy. Because of the lower limits of the provided proton energy by the cyclotron installed at WPE with 82.5 MeV (eye line) and 100.0 MeV, energy absorbers are used to pull back the Bragg peak to shallow depths. For this reason, a thick RS (such as the RS74) is applied for superficial tumors. Figure 2.12 shows energy absorbers that can be realized as a range shifter in a) (here shown a RS51) or as a range compensator in c) (patient compensator), which are placed between the nozzle and the patient. Materials with a low atomic number, such as plastic or water, are preferred for the construction of an RS. They provide the least amount of scattering when shifting the range [58]. Proton interactions in the RS material scatter protons and increase the lateral penumbra [76]. For a given air gap between the beam modifier and the patient the angular variance is translated to a spatial broadening in any delivery technique. This motivates the use of small air gaps [77]. In patient planning for the US and DS technique, patient-specific apertures and range compensators are required as mentioned in section 2.3.3. An aperture and patient-specific range compensator are presented in Figure 2.12 b) and c). The TPS automatically generates the appropriate aperture cutout and the individual compensator pixel thickness for each proton field depending on the selected PTV or CTV contour. Manual adjustments of both structures are necessary for further dose optimization.
Two different proton dose calculation engines are provided in RayStation. For all three proton techniques PBS, US and DS the Pencil Beam (PB) algorithm is implemented [78].

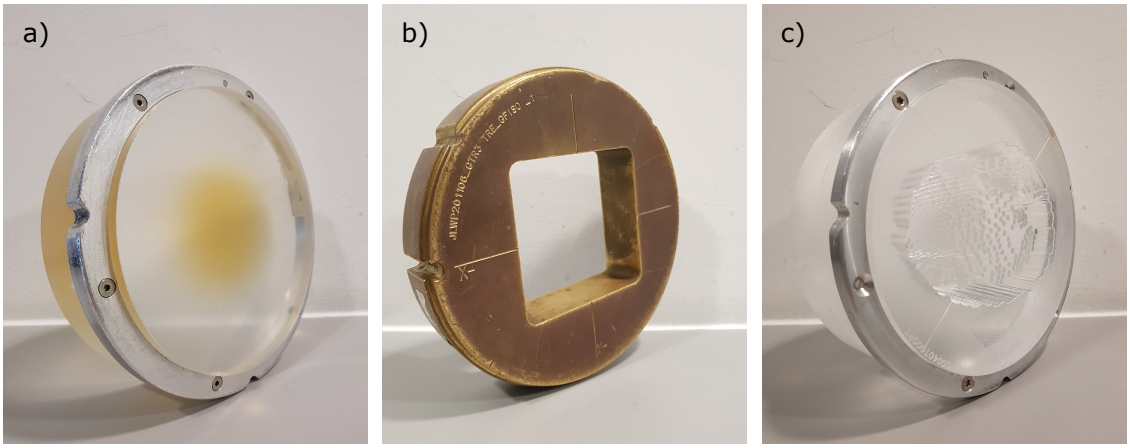


**Figure 2.12:** Accessories for proton beam modification. In TPS, beam modifications can be selected in patient planning. a) range shifter (RS): Depending on the snout shape, RS are round or rectangular. RS are made of polymethyl methacrylate (PMMA) and can be manufactured in various thicknesses to reduce the proton entrance energy and therefore the range of the protons. b) An aperture made of brass which limits the proton beam in a square shape. Patient apertures have a cutout in the geometry of the target volume. c) An example of a patient range compensator. One can clearly see the geometry of the target volume as well as the individual compensator pixels, which are of varying thickness to form the distal dose shape.

In addition, a clinical Monte Carlo (MC) algorithm is available for PBS since RayStation version 6 [79]. Important for all algorithms is the quality of the input data, obtained during the commissioning of the respective system.
The PB algorithm is a very fast dose calculation algorithm and is based on analytical approximations [80, 81]. As the name *Pencil Beam* suggests, the algorithm decomposes a proton spot into a large number of narrow beamlets. The individual pencil-like beams are transported along their beam axis into the patient, which is modeled as a stack of semi-infinite plate layers [82]. Due to the material allocation from the central PB to the plate of the respective depth, the algorithm has disadvantages against lateral inhomogeneities and heterogeneous geometries along the beam [83]. The dose calculation is performed for each voxel according to a specified grid. The grid limit of a voxel amounts to 1x1x1 mm. The dose in RayStation is determined by the lateral proton fluence $\Phi$ and the longitudinal integrated depth dose [82]. The lateral proton fluence is obtained from the data of the phase space parameters along the beam axis given by stopping power, multiple Coulomb scattering (MCS) and non-elastic nuclear interaction ([82, 84]). The Bethe-Bloch equation 2.3 without the additional terms in section 2.1.2 is the basis for the stopping power model in RayStation. MCS and nuclear interactions are responsible for the lateral spread of protons. In RayStation, MCS is described by the Fermi-Eyges theory, which is a transport equation for the Gaussian distribution for a path in the slab

[85]. As mentioned before, the lateral inhomogeneities are not included because only the primary proton Gaussian distribution (core) is considered and not the so-called nuclear halo [86]. The halo is a low dose region around the core created by the nuclear interactions [82] [87]. The problem of accurate modeling of the halo occurs especially with large air gaps and when applying RS [82]. The nuclear scattering was optimized according to a Gaussian correction term of Soukup et al. [88].
In RayStation, Monte Carlo (MC) is available for the PBS technique. It is a so-called fast MC algorithm, which is intended for clinical purposes. The computation time is reduced in contrast to general purpose MC algorithms like TOPAS or FLUKA, but the required accuracy for radiotherapy is reached [82, 89, 15]. The Monte Carlo algorithm of TOPAS is presented in more detail in the upcoming chapter 3.2.
The principle of MC simulations is to solve the proton transport equation in a geometry by random numbers and probabilities from density distributions. For this purpose, the physical processes have to be modeled very accurate. The probability of the density function corresponds in the simulation to the probability of a physics interaction. A history represents the trajectory of a particle. For a large number of particles, the MC simulation approximates the measured dose while reducing the uncertainty proportional to $1/\sqrt{(N)}$ [83, 90].
The initiation of protons of a spot is similar to the PB algorithm and is generated by the phase space parameters of the beam model upstream of the patient or the beam modification accessory. Basically, random primary protons are started from the proton source and transported through the geometry: beam modifying accessories, air gap, and patient. The determination of the dose is tracked by the energy deposition of the particles in the respective grid voxel. The dose calculation speed for clinical application of the RayStation MC dose engine is achieved by some simplifications [82]:

- **Particle transport** Accurate tracking (Class II) of the particles is done for primary and secondary protons [91]. For heavier particles like deuterons and alphas the energy loss is modeled by the continuous slowing down approximation [92]. There is no transport of neutrons and gammas in the geometry and other particles such as secondary electrons are neglected. However, the former is taken into account by the commissioning data, since the entire dose spectrum is measured. The latter is due to the fact that secondary electrons are generated at low energies and therefore usually have short ranges of <1 mm, which is within the smallest RayStation voxel size. As a result, the build-up effect in the TPS is not properly represented.

- **Particle interaction** Nuclear absorption, MCS and energy straggling are disregarded for some secondaries such as deuterons and alphas. Non-elastic nuclear reactions are taken of precomputed cross section libraries of published ICRU 63 data [32]. Further simplification concerns elastic scattering of protons on hydrogen

and nuclei.

It should be mentioned that the RayStation MC algorithm provides a more accurate dose calculation than the PB algorithm. This is especially the case for complex geometries and density variations, which have been discussed in various publication [93, 94, 95, 96]. Further information and details on the dose calculation algorithms can be obtained from the RayStation manual [82].

The clinical goals are determined by the doctors. They often follow the table of QUANTEC [97, 98, 99]. There, guidelines or dose tolerances are specified for various volumes of organs at risk. To achieve these clinical goals, so-called objectives and constraints are defined for the PBS technique. An objective function represents an optimization problem that needs to be minimized. Two selectable objecitves are e.g. *uniform dose* or *max dose* and are expressed as a relative weight (a weight of 100 is 100 times more important than a weight of 1). The RayStation optimizer has reached the solution for the two examples when a region of interest (ROI) in the entire volume and an ROI satisfies a maximum dose that is equal to or less than the defined dose. A multitude of objectives can influence each other and lead to conflict. Constraints are needed to fulfill requirements without compromise [100].
The optimization for the passive techniques US and DS is less complex. There, ROIs are defined as *treat* and *protect*. Further manual optimization is performed by modifying the aperture shape and compensator pixel length to adjust the lateral and distal dose distribution.

# Chapter 3

# Materials and Methods

## 3.1 Detector Types

### 3.1.1 Ionization Chambers

#### IBA PPC05

The PPC05 plane-parallel ionization chamber in Figure 3.1 a) is manufactured by IBA Dosimetry (Ion Beam Applications Dosimetry, Schwarzenbruck, Germany). The corresponding electrometer DOSE 1 in Figure 3.1 b) for the readout of the IC is also produced by IBA Dosimetry. The IBA PPC05 IC is suitable for dosimetry applications of photons, electrons and protons. The energy range according to the IBA product catalog for protons amounts to 40-230 MeV [101]. The IC is designed for a wide range of applications, i.e. it can be used in air, in a solid or in a water phantom. The last two can be combined with the PPC05 IC for depth dose curve measurements under broad field conditions. A compact list of the most important properties of the PPC05 IC is shown in Table 3.1. The IC consists of a chamber body, a stem and the associated cable with the TNC (threaded) triaxial connector. Due to the design, the chamber is vented and water-protected. The chamber body has a diameter of 30.0 mm and a thickness of 14.0 mm. The two electrodes are made of two different materials. The entrance window as the outer electrode is composed of the air-equivalent plastic C-552 (1.76 g/cm$^3$) in terms of chemical compositions and has a physical thickness of 1 mm. The inner collecting electrode is graphitized polyetheretherketone (PEEK, (1.32 g/cm$^3$)) with a diameter of 9.9 mm, defining the active volume of the IC of 46.0 mm$^3$ with the corresponding air gap of 0.6 mm between both electrodes. A guard ring at the level of the collecting electrode provides a stable electric field (E-Field) between the two electrodes. The DOSE 1 electrometer ensures the recommended polarization voltage of +300 V [102].

The DOSE 1 is a high performance reference class electrometer that fulfills the requirement for radiation therapy according to the IEC 60731 and AAPM ADCL protocols [103]. The accuracy and the wide range of resolution of the DOSE 1 allow a compatibility with a variety of detectors. Depending on the setting, the charge (dose) or the current (dose rate) is measured. The bias voltage is adjustable up to ± 500 V in 1 V steps. The electrometer can be set and operated via the built-in display. Remote connection is achieved with the included PC software or by extending the detector cables. The connection of the chambers is realized by a triaxial TNC socket. With a dimension of 25.9 cm [L] x 25.9 cm [W] x 16.5 cm [H] and a weight of 3.5 kg, the DOSE 1 is portable and flexible to position [104].

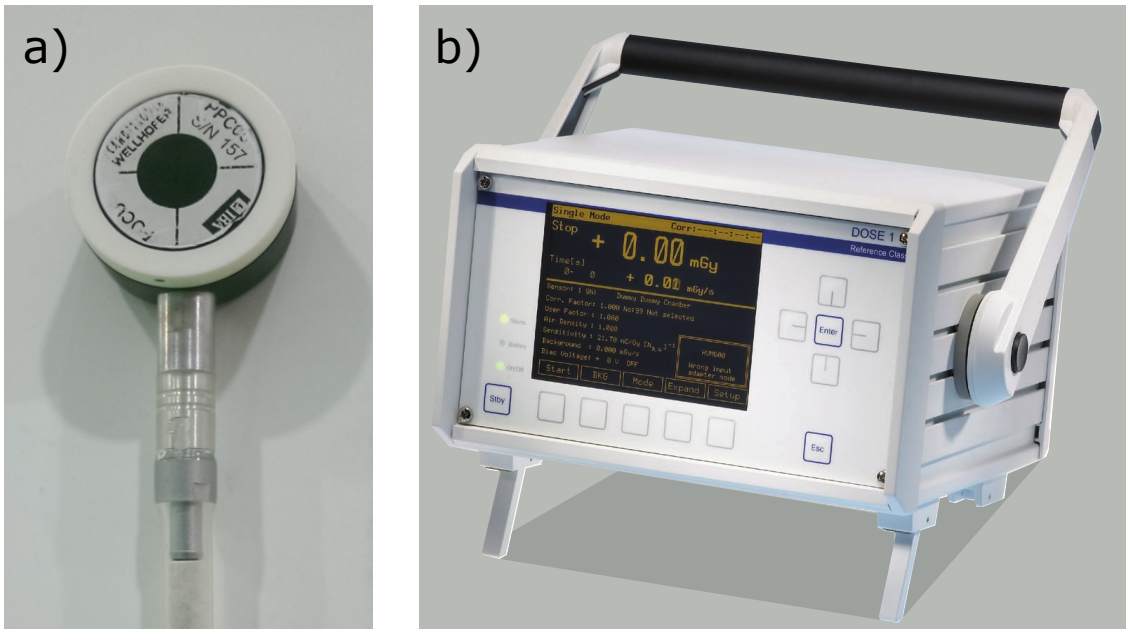


**Figure 3.1:** a) Photo of the IBA PPC05 plane-parallel ionization chamber. b) Photo of the IBA DOSE 1 electrometer, which is used to read out the PPC05 IC (reproduction according Ref. [104]).

| | |
|---|---|
| Measuring quantity: | Absolute dosimetry of electron, photon & proton beams in radiotherapy |
| Positioning: | In air, solid or water phantom |
| Chamber type: | vented ionization chamber |
| Circular shaped electrode, inside and outside: | 9.9 mm & 20.0 mm in ⌀ |
| Electrode material, inside and outside: | polyetheretherketone (PEEK) graphitized & Shonka-C552 |
| Electrode mass density: | 1.32 g/cm³ & 1.76 g/cm³ |
| Electrode separation: | 0.6 mm |
| Entrance window thickness (Shonka-C552): | 1 mm |
| Energy ranges for protons: | 40 to 230 MeV |
| Polarizing voltage: | +300 V |
| Field size: | $\geq$ 4 cm x 4 cm |
| Reference point: | Inner side of the entrance window |
| Chamber body dimension: | 30.0 mm in ⌀ & 14.0 mm in thickness |
| Connector type: | TNC triaxal connector |
| Electrometer: | IBA DOSE 1 |

**Table 3.1:** Technical data of the IBA PPC05 plane-parallel ionization chamber [102].

#### PTW Extrapolation Ionization Chamber Type 23391

Figure 3.2 depicts two devices of the manufacturer PTW (Physikalisch-Technische Werkstätten Dr. Pychlau GmbH, Freiburg, Germany): a) a photo of the PTW extrapolation plane-parallel ionization chamber type 23391 and b) a photo of the PTW TANDEM electrometer. PTW's in-house developed connection system type M of the extrapolation IC requires a corresponding PTW electrometer. Already in 1952, an extrapolation IC was designed to perform dosimetry with beta sources [105]. The IC is suitable for dose and dose rate measurements of photons and electrons [106, 107, 108, 109].
The PTW extrapolation IC type 23391 has a cylindrical shape and a micrometer screw on the back side. The body diameter measures 12.5 cm and has a body thickness of 7.9 cm. The micrometer screw extends the length of the chamber to 15.5 cm. Adjusting the micrometer screw (accuracy of $\pm$ 1 $\mu$m) results in a displacement of the inner collecting electrode. This reduces the air gap between the two electrodes from a maximum of 25.5 mm to 0.5 mm. The inner electrode is made of an unknown tissue-equivalent material and has a diameter of 30.0 mm surrounded by a guard ring. It suggests the material Shonka A-150 (Ref. [110]) due to the black color and according to Ref. [111].

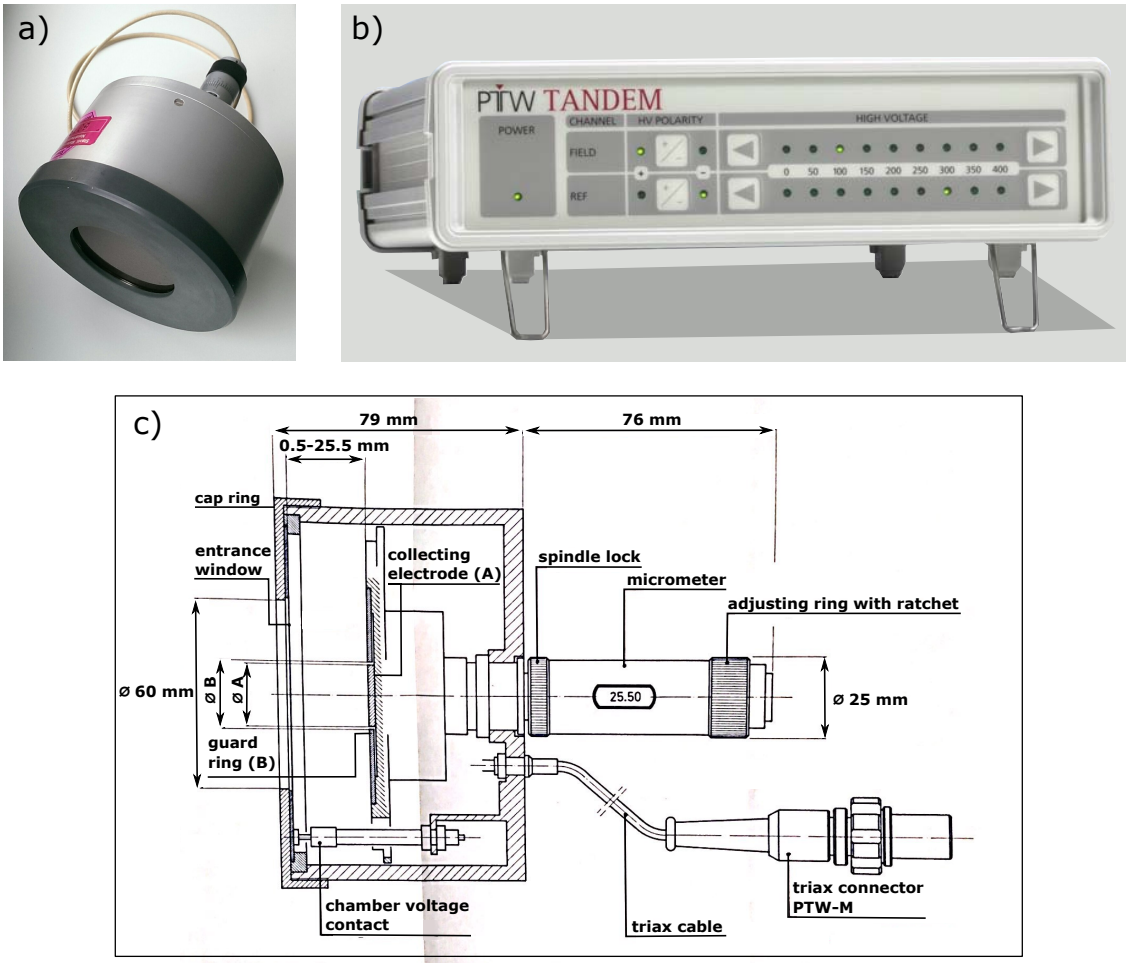


**Figure 3.2:** a) Photo of the PTW extrapolation plane-parallel ionization chamber type 23391. b) Photo of the PTW TANDEM electrometer, which is used to read out the extrapolation IC (reproduction according Ref. [112]). c) Technical drawing and cross section of the PTW extrapolation IC type 23391 (reproduction according Ref. [106]).

Figure 3.2 a) and c) show a screw-on cap ring with a circular cutout on the front side of the chamber. Behind there is the front entrance window, which is fixed by the cap ring. The 60.0 mm entrance window consists of a Kapton® (polyimide) film and is stretched on a circular aluminum sheet with a cutout. Three entrance windows are available with various thicknesses: 25, 50 and 75 $\mu$m. The entrance window is replaced by switching off the chamber voltage and unscrewing the cap ring. This requires the correct orientation of the entrance window, which is placed with a small round hole in the aluminum sheet on the corresponding pin of a narrow retaining ring, which in turn is correctly positioned in the chamber by another pin. Figure 3.2 c) sketches the voltage contact within the chamber in the technical drawing. At the rear, a triax cable exits the chamber for connection to an electrometer [106]. Due to the design of the extrapolation IC, the actual

volume, the chamber voltage and the detector response depend on the selected electrode distance.

| | |
|---|---|
| Measuring quantity: | Dose & dose rate measurements for electrons & photons |
| Positioning: | In air on patient table |
| Chamber type: | Vented ionization chamber |
| Circular shaped electrode, inside and outside: | 30.0 mm & 60.0 mm in ⌀ |
| Electrode material, inside and outside: | Tissue equivalent material & Kapton® |
| Electrode separation: | Variable from 0.5 to 25.0 mm |
| Entrance window thickness (Kapton®): | 25, 50 & 75 $\mu$m |
| Energy ranges for protons: | 40 to 230 MeV |
| Polarizing voltage: | Max. ±400 V, dependent on electrometer & electrode distance |
| Reference point: | Inner side of the entrance window |
| Chamber body dimension: | 12.5 cm in ⌀ & 7.9 cm in thickness |
| Connector type: | PTW M triaxal connector |
| Electrometer: | PTW TANDEM |

**Table 3.2:** Technical data of the PTW extrapolation plane-parallel ionization chamber type 23391. [106, 112, 113].

The PTW TANDEM is a dual channel electrometer and is certified according to the IEC 60731 protocol [103]. It is suitable in radiation therapy for absolute measurements of dose and dose rate. The TANDEM is available in various versions, which differ in the type of connector. The device used in this work had a PTW connector type M and the power supply was provided by the TBA CONTROL UNIT T41013. Two detectors can be connected by the dual channel interface, called field detector and reference detector. Figure 3.2 shows the front panel of the PTW TANDEM without the TBA CONTROL UNIT. Through the panel interface and the LED light, the power button, the polarity and the high voltage can be set and recognized. The electrometer provides a bias voltage between 0 and ± 400 V in steps of 50 V [112]. Alternative control or by remote as well as further settings are possible with the TanSoft software [114]. The PTW TANDEM measures 32.4 cm [L] x 25.7 cm [W] x 8.1 cm [H] and has a weight of 2.9 kg [112].

### IBA Zebra

The IBA commercial multi-layer ionization chamber (MLIC) Zebra (Ion Beam Applications Dosimetry, Schwarzenbruck, Germany) is a detector to measure scanned pencil beams or SOBPs in a single measurement [115]. A photo of the Zebra detector is shown in Figure 3.3. In addition, the corresponding software OmniPro-Incline (Ion Beam Applications Dosimetry, Schwarzenbruck, Germany) and a high-sensitivity multichannel electrometer with Tera06 ASICS technology are required [116]. The MLIC Zebra detector, as well as the similar MLIC device Giraffe (variation in electrode diameter) have been evaluated at WPE and also in other papers against other ionization ICs in combination with a water tank [117, 118, 119]. The Zebra is suitable as a fast and efficient setup for determining the range and depth dose curve in QA or as a tool to measure the water-equivalent thickness.

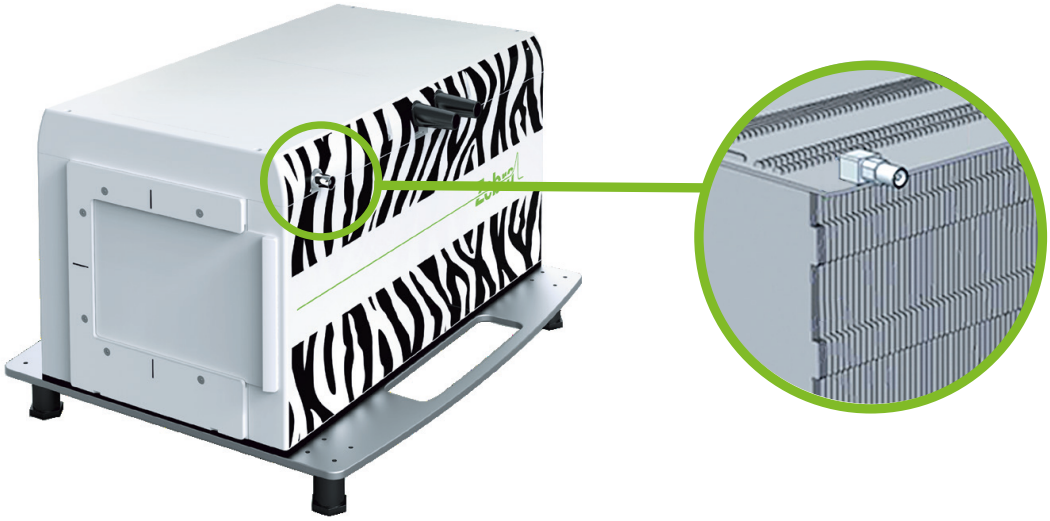

**Figure 3.3:** The IBA multi-layer ionization chamber (MLIC) Zebra detector is an important and time-saving device to measure Bragg Peaks and spread-out Bragg Peaks in a single measurement. This is achieved by the construction of 180 stacked electrodes (reproduction according Ref. [120]).

The Zebra Detector has 180 air-vented plane-parallel ICs connected in series with an electrode diameter of 2.5 cm. The electrode separation is approximately 1 mm [120]. The multichannel electrometer provides a simultaneous readout of all electrodes, allowing energy range measurements from 2 mm up to 330 mm water equivalent depth. By a suitable choice of the electrode material with Polyimide and Duraver (Isola GmbH, Duren, Germany), which is composed of Polyimide and glass, a water equivalent device with an electrode thickness of 1 mm and an electrode mass density of 2 g/cm$^3$ is achieved

[117]. This results in a water equivalent thickness of approx. 1.85 mm per channel. In the OmniPro-Incline software, a channel is translated as a bin and describes the depth axis in the z-direction. The dimension of the MLIC is 43.9 cm [L] x 17.5 cm [W] x 19.5 cm [H] [120]. The device can be placed on the treatment table by aligning the marks using the gantry lasers.
A daily uniformity calibration must be performed for the use of the zebra. This means a beam calibration with the maximum energy of 226.7 MeV at WPE. This adjusts the signal as relative dose to the target dose value of the reference measurement in water (at WPE measured with the IBA PPC05 IC), i.e. the sensitivity of each electrode is corrected. Therefore, the proximal section of the Bragg peak is preferred for dose calibration. The choice of the highest energy covers this section accordingly and allows calibrated depths of up to approx. 280 mm. The procedure is performed in OmniPro-Incline. Furthermore, a fast analysis of the data can be realized by the software.

| | |
|---|---|
| Measuring quantity: | Pristine & spread-out Bragg peak |
| Positioning: | Patient table, optional nozzle mount |
| Chamber type: | Vented ionization chambers |
| Circular shaped electrode: | 2.50 cm in ⌀ |
| Electrode material: | Mixture of Polyimide & Duraver (mixutre of glass and Polyimide) |
| Electrode mass density: | 2 g/cm$^3$ |
| Electrode separation: | 1 mm |
| Channels: | 180 |
| Water equivalent thickness/channel: | ≈1.85 mm/channel |
| Energy range: | 2 mm to 330 mm water equivalent depth |
| Polarizing voltage: | -150 V |
| Field size: | 10 cm x 10 cm |
| Reference point: | On the markers for three axes (x,y,z) |
| Electrometer: | 4 TERA ASICs (each contains 64 electrometers) |
| Device dimension: | 43.9 cm [L] x 17.5 cm [W] x 19.5 cm [H] |

**Table 3.3:** Technical data of the IBA multi-layer ionization chamber (MLIC) Zebra detector [120, 119, 121].

### EXRADIN T1

For the sake of completeness, the last chamber EXRADIN T1 (Standard Imaging, Middleton, WI, USA) ionization chamber is introduced (see Figure 3.4). Its type is called miniature Shonka chamber or thimble chamber with a design resembling a pen. The T1 IC is suitable for absolute dosimetry of photons, electrons and protons and can be applied in water, in air and into a phantom. A summary of the IC data can be found in Table 3.4. The collecting volume consists of a guard, a collector and a shell. The collecting electrode is centered in the volume (compare Figure 3.4 b)) and is surrounded by air and the shell. Every part of this IC is made from tissue-equivalent plastic called A150. The readout is done via the electrometer IBA DOSE 1 with a corresponding bias voltage of +300 V and a TNC triaxal connector.


**Figure 3.4:** a) Photo of the EXRADIN T1 ionization chamber [122]. b) Technical drawing of the miniature Shonka IC [123].

| | |
|---|---|
| Measuring quantity: | Absolute dosimetry of electron, photon & proton beams in radiotherapy |
| Positioning: | In air, solid or water phantom |
| Chamber type: | Miniature Shonka Chamber |
| Collecting volume: | 0.056 $cm^3$ |
| Collecting diameter: | 1.0 mm |
| Outside diameter of shell: | 6.0 mm |
| Electrode material, inside and outside: | T1 Shonka tissue equivalent plastic A150 |
| Wall thickness (Shonka-A150): | 1 mm |
| Polarizing voltage: | +300 V |
| Reference point: | 4.0 mm from tip of chamber |
| Connector type: | TNC triaxal connector |
| Electrometer: | IBA DOSE 1 |

**Table 3.4:** Technical data of the EXRADIN T1 ionization chamber [123].

### 3.1.2 Thermoluminescence Detector

In this work thermoluminescence detectors (TLD) are applied, which were provided by the MPA NRW (Materialprüfungsamt NRW, Dortmund, Germany). The detectors are based on lithium fluoride doped with magnesium and titanium. A preliminary study of TLD skin dose measurements in proton therapy were investigated during a master thesis project by L. Mertens [124] and contributed to this work.

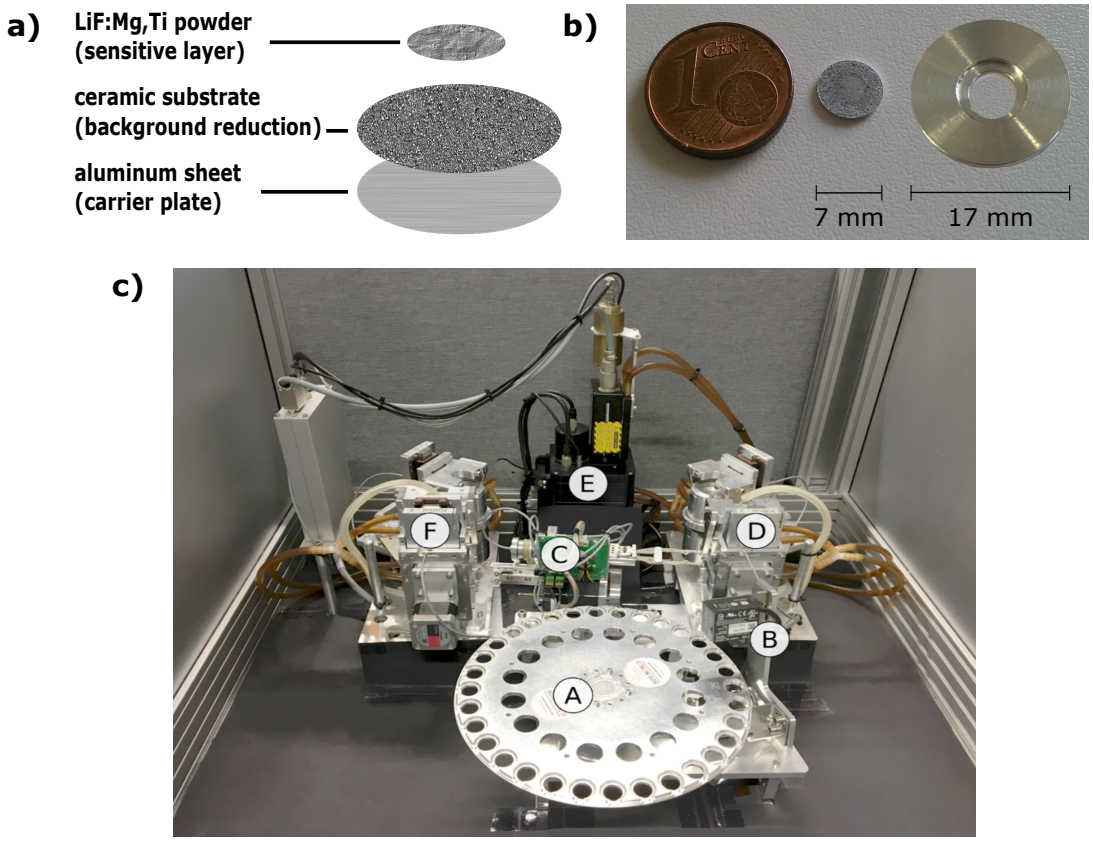


**Figure 3.5:** a) Schematic representation of a TL-DOS detector showing the three layers from bottom to top: Aluminum sheet as carrier plate, a sprayed ceramic substrate and the sensitive layer with lithium fluoride doped with magnesium and titanium (LiF:Mg,Ti, reproduction according Ref. [125]). b) The 1 cent coin on the left is compared with the TLD used in this work (center). On the right there is the corresponding adapter for the readout in the TL-DOS system. The conventional TLDs for the TL-DOS system feature the adapter size on the right side of the Figure 3.5 b). c) The TL-DOS TLD prototype reader, which consists of the following components: A) carousel for 32 detectors, B) bar-code scanner, C) gripping robot for transportation, D) pre-heating unit at 155°C, E) main readout unit with a heating plate at a constant temperature (300°C) and a photo multiplier tube and F) annealing unit (extracted from Ref. [51, 125]).

A photo of the detector is presented in the center of Figure 3.5 b). The associated readout device is called TL-DOS (thermoluminescence dosemeter system) prototype in Figure 3.5 c). As part of the restructuring of film dosimeters (also known as X-ray badges) for photon radiation detection in the whole-body dosimetry to a more modern automated TLD system in 2022 at MPA, the TL-DOS readout was an initial prototype for the transition [126]. In general, TLDs can report deposited dose for a variety of radiation types [127]. A schematic representation of the TLD detector is given in Figure 3.5 a). The sensitive thermoluminescent material that is used here in the form of powder is named MT-N and is produced by the company Radcard - TLD Dosemeters (Krakow, Poland). The natural LiF material exhibits the composition of the two isotopes $^{6}$LiF:Mg,Ti (∼5%) and $^{7}$LiF:Mg,Ti (∼95%) [51, 128]. The enrichment of an isotope affects the detection of radiation types. Thus, Li-7 (MT-7) is sensitive to photon irradiation and Li-6 (MT-6) is sensitive to photon and neutron mixed fields. The latter detects neutrons by neutron capture, producing an alpha particle that induces the signal in the TLD [129].
The carrier material of the powder is an aluminum sheet, which is shown in Figure 3.5 a) below. A flame spray layer in form of a ceramic substrate is sprayed on the surface of the aluminum to reduce the background signal. Then, the lithium fluoride powder must be hot pressed onto the ceramic substrate in a sintering process. The amount of LiF:Mg,Ti powder can range between 1 mg and 35 mg, depending on the application. By default, TLDs of TL-DOS are provided with 15 mg of LiF:Mg,Ti, whereas in this work 2 mg were produced to achieve a low amount of the powder layer. This requirement results in the smaller TLD design for the application in this work, which can be seen in the center of Figure 3.5 b). The TLDs are 7 mm in diameter and the thickness of the aluminum is 0.5 mm. A bar-code is located on the back side of the aluminum sheet for detector identification. The standard detectors of the TL-DOS are larger with a diameter of 17 mm. The aluminum core is 10 mm and contains a frame. Since the TL-DOS is designed for these larger TLDs, the small TLDs in this work must be used with an adapter ring. An adapter ring for enlargement is presented in Figure 3.5 b) on the right [51, 125, 124, 130]. A compact overview of the TLD data is provided by Table 3.5.
The TL-DOS readout prototype is responsible for the automated analysis of the TLDs. A photo of the device with the various stations is given in Figure 3.5 c). The reader consists of seven stations, labeled as A) to F) in the photo. Up to 32 detectors can be placed in the carousel (A) in the outer track. A TLD is identified via the bar code scanner. An important component of the reader is the gripping robot. By grabbing, holding and transporting the TLD, three stations can be approached: D), E), F). At the beginning of the process, the TLDs are transported to a pre-heating station D). The heating plate raises the temperature of the TLD for 10 s with 155°C, which prevents thermal fading. This means that the peaks 1,2 and a part of 3 are deleted from the glow curve (see Figure 3.6 and subsection *LiF:Mg,Ti Glow Curve* for more information about fading).

The short-lived traps are empty and only the stable long-lived peaks are left. To ensure that only the desired traps are erased, direct cooling on the plates at room temperature is necessary. For this purpose, the TLD is pushed next to the second plate (above the letter D). The actual measurement is performed in the next step, when the gripping robot moves the TLD into the main readout unit E). Due to the temperature of the heating plate of 300°C, the TLD heats up exponentially and the photons emitted by the thermoluminescence effect are recorded within 15 s readout process. A photo multiplier tube is responsible for recording the thermoluminescence light. The TL-DOS is connected to a computer with the corresponding TLView software. There, the glow curve is plotted and the area below the glow curve is acquired. The photo multiplier tube can operate in two modes: single photon mode and photon current mode. In this work, the photon current mode must be applied because single photon counts are no longer possible due to too high doses (>mSv). Reuse of the TLD is possible by completely erasing the traps in the material by annealing at 400 °C for 15 s in station F) [125, 124].
Several studies investigated skin dose measurements using photon beams with various types of TLDs [131], [132], [133].

| | |
|---|---|
| Measuring quantity: | Absorbed dose for radiotherapy & radiation protection for protons, neutrons, electrons & photons |
| Positioning: | In air or solid phantom |
| TLD type: | Lithium fluoride doped with magnesium and titanium (LiF:Mg,Ti) |
| TLD structure: | LiF:Mg,Ti pressed on aluminum sheet with ceramic coating |
| Amount of powder: | 2 mg |
| TLD dimension: | 7.0 mm in ⌀ & 0.5 mm in thickness for aluminum |
| Pre-heating temperature: | 155°C |
| Cooling temperature: | Room temperature |
| Heating temperature: | 300°C |
| Annealing temperature: | 400°C |
| Pre-heating time: | 10 s |
| Cooling time: | 3 s |
| Photo multiplier tube time: | 15 s |
| Annealing time: | 15 s |
| Reading station: | TL-DOS reader |

**Table 3.5:** Specification of the TLD and the TL-DOS readout system [125, 124, 130].

### LiF:Mg,Ti Glow Curve

In the TLView software, a glow curve is plotted as a function of time for each TLD read out. The y-axis describes the detected photon counts by the photo multiplier tube. An example of a glow curve with its characteristic shape and peak labeling is given in Figure 3.6.
This glow curve originates after a proton irradiation of the TLD. The peaks are labeled according to a nomenclature with the numbers 3 to 5 [134]. The three peaks correspond to the respective emptied traps. The electrons have returned back to the valence band as a result of the energy supply (heating). Accordingly, there are short-lived traps named peak 1-2, which, however, have a reduced lifetime at room temperature. With a time gap between measurement and evaluation time, these traps can bias the result. For this reason, an emptying of these traps (peak 1-2) occurs by preheating. This effect is also known as post-irradiation fading (for TL-DOS in [51, 135]). Higher occupied peaks (3-7) are so called high-LET traps created by particles with high ionization density e.g. neutrons [136].
The integral of the glow curve is proportional to the irradiated dose. By subtracting the background from the raw signal and using a calibration factor of a $^{137}$Cs (662 keV) irradiation, it is possible to determine a dose.

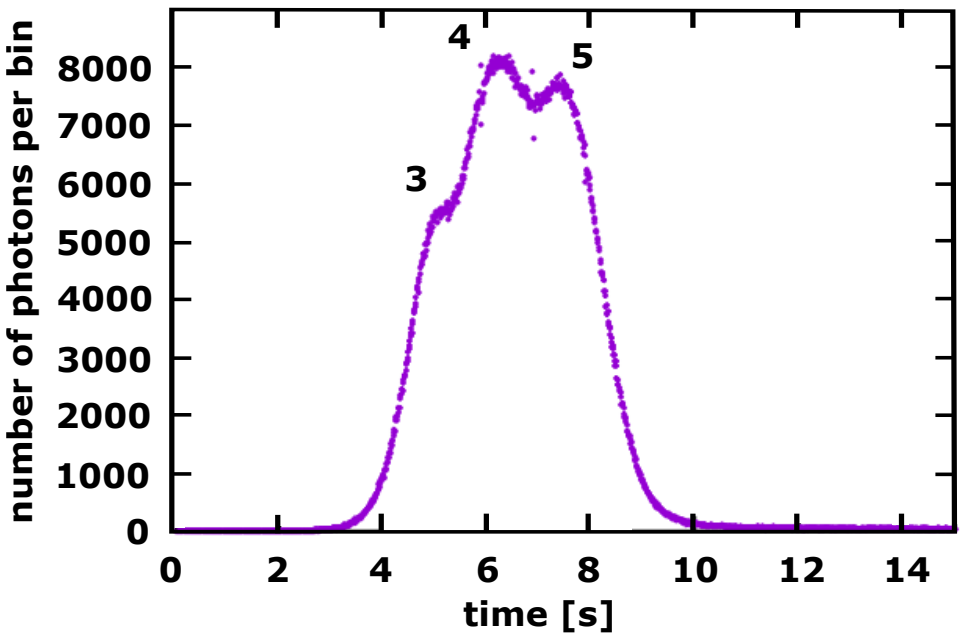


**Figure 3.6:** Readout by TL-DOS and TLView software: Glow curve obtained after proton irradiation of LiF:Mg,Ti. The pre-heating process eliminates peak 1-2 (fading effect), but the glow peaks 3-5 are visible (extracted from Ref. [124]).

### 3.1.3 Radiochromic Films

As introduced in the theory Chapter 2.2.3, chemical detectors in form of radiochromic films are used in this work. One of the manufacturer of the radiochromic films is Ashland ISP Advanced Materials (Convington, KY, USA) with their brand Gafchromic™. Various Gafchromic™ films were already used to investigate the skin dose in photon therapy [137], [138], [139]. The two following subsections present the two Gafchromic™ films used in this work.

#### EBT3 Film

The Gafchromic™ EBT3 film is the third product in the EBT (External Beam Therapy) series. The EBT3 film is suitable for measuring absorbed dose in radiotherapy and radiology for the three common types of radiation: photons, electrons and protons. The film can be used for various applications, i.e. in air, in a solid phantom or even for a short duration in water.
The structure of the EBT3 film is shown in Figure 3.7 a). The film has a symmetrical structure and consists of two dissimilar layers: an active layer sandwiched by two matte surface clear polyester layers. The thicknesses of the layers are 30 $\mu$m for the active layer and 125 $\mu$m for the matte polyester layer [140]. This information is taken from a written communication (e-mail) with the Ashland company. Depending on the literature, various information is given for the thickness of the layers because they vary slightly due to the production process [140, 141, 142]. The two matte surface clear polyester layers protect the inner active layer and allow an easier handling of the film as well as a short-term water protection [143]. Compared to its predecessor model EBT2, the EBT3 film has a Newton ring coating that eliminates artifacts caused by interference [143, 144]. The active layer of the film contains the active component, a colorless photo monomer molecule, which triggers a polymerization process by interacting with an energetic particle [52]. The result is a color change into a blue color without the need for chemical processing. Other components in the active layer are the marker dye, stabilizers and other undefined components [141].
A purchased Gafchromic™ EBT3 film box contains 25 films with dimensions of 20.3 cm [L] and 25.4 cm [W] with a resulting physical thickness of 280 $\mu$m. They are suitable for high temperatures (up to 60°C) and the built-in marker dye reduces the UV/visible light sensitivity, i.e. a use in daylight is possible. Further EBT3 film properties are a near skin equivalence, a dose range between 0.1 Gy to 20.0 Gy, a low energy dependence and due to the structure a very high spatial resolution (25 $\mu$m and less). A compact overview of the specifications is given in Table 3.6.

| | |
|---|---|
| Measuring quantity: | Absorbed dose for radiotherapy & radiology for protons, electrons & photons |
| Positioning: | In air, solid or water phantom |
| Radiochromic film type: | EBT3 Gafchromic™ |
| Film structure: | 30 $\mu$m thick active layer sandwiched by two 125 $\mu$m matte surface clear polyester substrates |
| Layer density: | 1.20 g/cm$^3$ (active) & 1.35 g/cm$^3$ (matte polyester) |
| Film thickness: | 280 $\mu$m |
| Spatial resolution: | High resolution down to 25 $\mu$m or lower |
| Dynamic dose range: | 0.1 Gy to 20.0 Gy |
| Sheet dimension: | 203.2 mm [L] x 254.0 mm [W] x 0.28 mm [H] |
| Film orientation | Landscape orientation |
| Flatbed document scanner: | EPSON Expression 10000XL |

**Table 3.6:** Specification of the EBT3 Gafchromic™ film developed by Ashland [140, 141].

A flatbed document scanner is required for further processing of the films. In the case of the WPE, this was a graphic scanner of the EPSON brand called Expression 10000XL (EPSON, Suwa, Japan). The scanner is a large device with a size of 45.8 cm [L] x 65.6 cm [W] x 15.8 cm [H], a weight of 14.5 kg and offers a scanning area of 43.7 cm [L] x 31.0 cm [W] [145]. The scanner's color images are taken in 48-bit, which means that the scanner measures the red, green and blue component of the transmitted light in 16-bit per color channel [141].

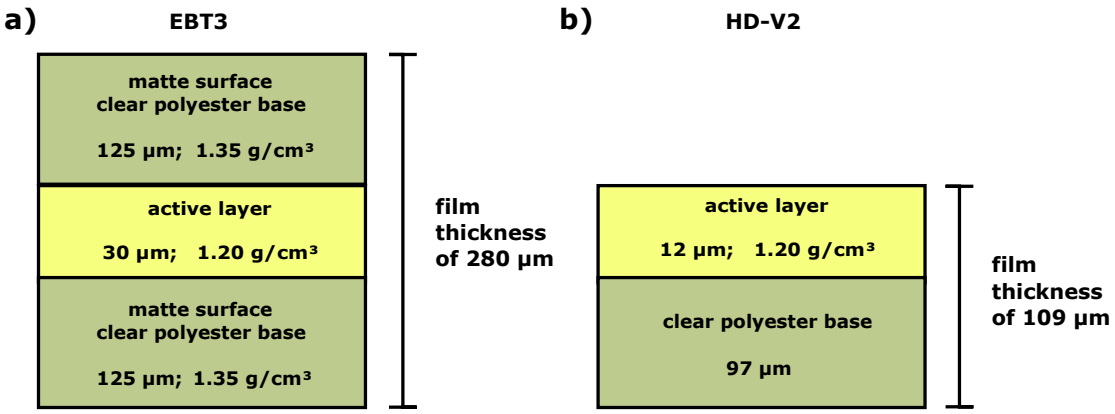


**Figure 3.7:** Structure of the two Gafchromic™ films. The layers are divided into an active and a polyester layer. a) A Gafchromic™ EBT3 film with a physical thickness of 280 $\mu$m. The active layer is sandwiched by two matte surface clear polyester substrates. b) A Gafchromic™ HD-V2 film consisting of two layers, an active layer and a clear polyester substrate, with a total physical thickness of 109 $\mu$m.

### HD-V2 Film

The abbreviation HD-V2 of the Gafchromic™ film stands for High Dose-Version 2 and is the successor of the Gafchromic™ HD-810 film. HD-V2 is applicable for high energy doses for photons, electrons and protons. In contrast to the EBT3 film, the asymmetric arrangement of the film layers allows application in air or on a phantom.
Figure 3.7 illustrates the asymmetric coating compared to the EBT3 film. The HD-V2 film in Figure 3.7 b) is divided into an active layer and a clear polyester substrate. The chemical composition of the active layer is similar to the EBT3 film and is marked for layer side detection. The thickness amounts to 12 $\mu$m. Since the active layer is not encapsulated, it is susceptible to all external influences and therefore not suitable for use in water. Instead of a matte polyester surface layer, the HD-V2 relies on a clear polyester layer with a thickness of 97 $\mu$m. The total physical thickness of the film is hence 109 $\mu$m [146].
The following table presents the main specifications of the HD-V2 film:

| | |
|---|---|
| Measuring quantity: | Absorbed dose for radiotherapy for protons, electrons & photons |
| Positioning: | In air or solid phantom |
| Radiochromic film type: | HD-V2 Gafchromic™ |
| Film structure: | 12 $\mu$m thick active layer on a 97 $\mu$m clear polyester substrate |
| Layer density: | 1.20 g/cm$^3$ (active) & no data for clear polyester |
| Film thickness: | 109 $\mu$m |
| Spatial resolution: | High resolution down to 5 $\mu$m or lower |
| Dynamic dose range: | 10.0 Gy to 100.0 Gy |
| Sheet dimension: | 203.2 mm [L] x 254.0 mm [W] x 0.109 mm [H] |
| Film orientation | Landscape orientation |
| Flatbed document scanner: | EPSON Expression 10000XL |

**Table 3.7:** Specification of the HD-V2 Gafchromic™ film developed by Ashland [146].

The HD-V2 film box contains only 5 films with the dimensions of 20.3 cm [L] and 25.4 cm [W]. The characteristics of the HD-V2 film are similar to those of the EBT3 film, with the following exceptions: The HD-V2 film has a shifted dynamic dose range towards higher doses starting from 10.0 Gy to 100.0 Gy. The spatial resolution is higher with 5 $\mu$m and less [146].
Similar to the Gafchromic™ EBT3 film, the use of the flatbed document scanner EPSON Expression 10000XL is also recommended for the HD-V2 film. A description of the scanner was given in the subchapter 3.1.3 of the EBT3 film.

## 3.2 TOPAS Monte Carlo Simulation

### 3.2.1 Introduction

As already introduced in the planning subchapter 2.4.1, which discussed the algorithms in the Raystation planning system, the Monte Carlo code is used to track various particles including the physical interaction processes in a medium and geometric structures. A Monte Carlo code can be used for various applications in radiotherapy and covers a wide range of particle transport and nuclear medicine. Some examples are radiotherapy, brachytherapy, radiation protection, imaging, etc.. The advantage of simulations are the possibilities to study the behavior of particles, to model complex experimental setups that are not easily reproducible experimentally, or to answer questions about physical parameters such as dose deposition, dose distributions or dose rates [147].
In general, the role of Monte Carlo can be illustrated in Figure 3.8. The theory serves as an inspiration for the design of the experiment and Monte Carlo can contribute to the verification and analysis of the experiment [148].

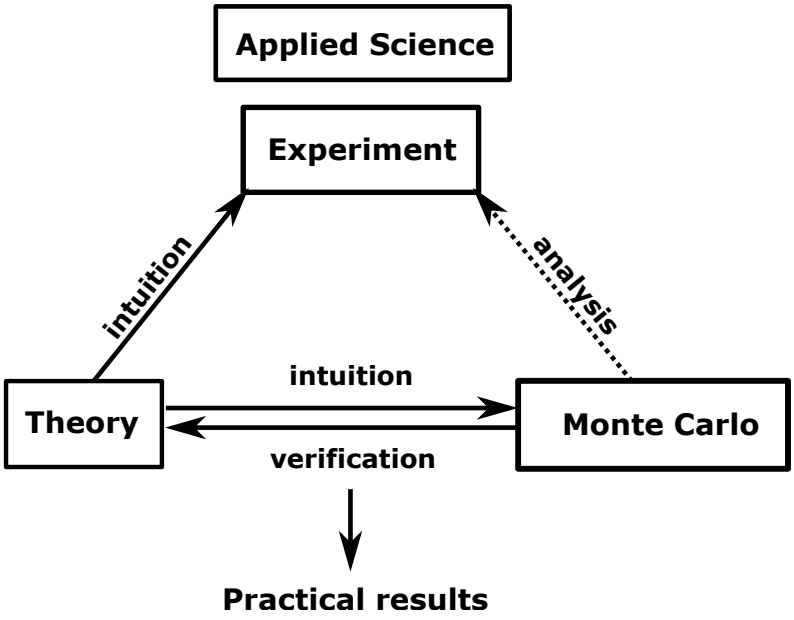


**Figure 3.8:** Monte Carlo as a third field in addition to theory and experiment in applied science (adopted from Ref. [148]).

TOPAS offers many potentials besides its use for proton therapy. For example, there are TOPAS publications in HDR brachytherapy [149], nanoparticle models [150] and DNA damage [151] , proton radiography [152], X-ray fluorescence spectroscopy [153] or

a study on carbon ion radiotherapy [154]. In this work, the Monte carlo code TOPAS is applied to study the surface dose, i.e. in the first 5 mm of the depth dose curve and in the micrometer range to determine the skin dose.

### 3.2.2 Structure Of TOPAS

TOPAS is the abbreviation for TOol for PArticle Simulation [15, 155]. TOPAS is based on the all-particle Monte Carlo toolkit Geant4, which is the framework for tracking, geometry, physics models and hits [156]. The energy spectrum of Geant4 covers the TeV (Tera electron Volt) range, whereas in TOPAS the energy range for proton therapy is relevant from keV (kilo electron Volt) to MeV (Mega electron Volt). The TOPAS interface simplifies the use of the tools in Geant4, providing access to Monte Carlo for the medical physics community. Additionally, TOPAS benefits from the enhancements and new features in Geant4. Version 3.1.p2 of TOPAS and the base of Geant4 10.03.p1 were used for the simulations.

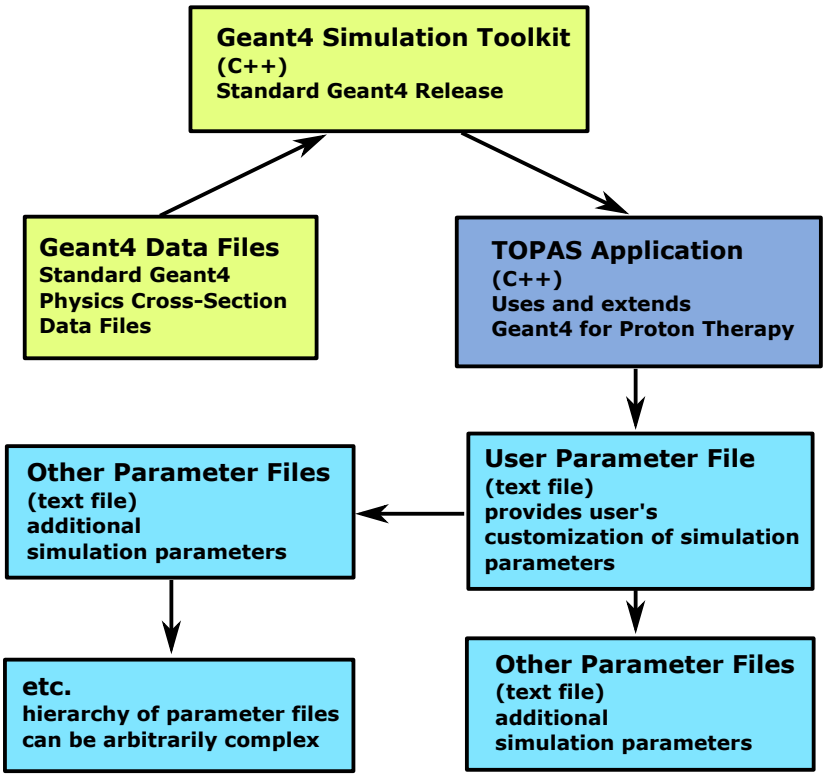


**Figure 3.9:** Hierarchy structure of TOPAS. The user defines the User Parameter Files, which may also form a hierarchy system (reconstructed from Ref. [15]).

While in Geant4 the user has to write C++ files, in TOPAS so-called TOPAS Parameter Control Files are used, so that no handling of C++ is necessary. The idea behind the TOPAS key classes in the TOPAS parameter control files is to specify what should happen at a run time. A representation of the structure in TOPAS is defined in Figure 3.9.
In the user defined text files the parameters are set line by line according to a mastered format (syntax):

Parameter_Type : Parameter_Name = Parameter_Value  #Optional comment

There are six different parameter types in TOPAS: *s*, *i*, *b*, *d*, *u* *xv*. Similar to the common programming languages *s* stands for *string* or *i* for *integer*. The further meanings of the abbreviations can be found in the upper part of Table 3.8. The parameter type is a control for the user's input. TOPAS expects the correct format depending on the parameter type and verifies this (strict type checking). An example for the type double would be a number plus a unit.

| Parameter type | Meaning |
|---|---|
| s | String |
| i | Integer |
| b | Boolean |
| d | Dimensioned Double |
| u | Unitless Double |
| xv | Vector, where x stands for one of the five parameter types |

| Major parameter name | Meaning |
|---|---|
| Ma/ | Materials |
| El/ | Elements |
| Is/ | Isotopes |
| Ge/ | Geometry Components |
| So/ | Particle Sources |
| Ph/ | Physics |
| Vr/ | Variance Reduction |
| Sc/ | Scoring |
| Gr/ | Graphics |
| Tf/ | Time Features |
| Ts/ | TOPAS overall control |

**Table 3.8:** TOPAS Parameter Type and Major Parameter Name. Five parameter types in the upper and eleven parameter names in the lower part of the table [157].

Another feature of the parameter files and structure in Figure 3.9 is that values or properties can be overwritten for a given simulation. This is done in the upper parameter

files keeping the original data untouched. This can be e.g. the material overwriting of a nozzle component.
The major parameter name follows in the mastered format after the parameter type. Parameter names can be used for all commands in TOPAS. Examples are *Ma* for *material* or *So* for *particle source*. Further names are located in the lower part of Table 3.8. The main parameter name is usually followed by an individual object name, e.g. the free naming of the scorer like *MyScorer* or similar [15, 155].
All commands for the respective major parameter names and further information can be taken from the TOPAS manual [157]. Examples of TOPAS commands are listed in Table 3.9 and give an overview of the entire TOPAS syntax.

| Parameter | Function |
|---|---|
| d:Ma/MyComponent/Density = 9.3 g/cm3 | Defines the density |
| s:Ge/MyComponent/Material = "Gold" | Assignment of a material |
| s:Ge/MyComponent/Type = "TsBox" | Component is a rectangular box |
| d:Ge/MyComponent/HLX = 20.0 cm | Sets half length in x-direction |
| i:Gr/MyGraphic/WindowSizeX = 1368 | Size of graphic window in x-direction |
| s:So/MySource/BeamParticle = "proton" | Particle type assignment |
| d:So/MySource/BeamEnergy = 150.0 MeV | Defining the beam energy |
| includeFile = Nozzle.txt | Embedding of a parameter file |

**Table 3.9:** Examples of TOPAS parameters and their function.

### 3.2.3 TOPAS WPE Model

For the present work, an IBA nozzle model for the WPE is required. Initial Monte Carlo work at the WPE had designed the basis of the WPE Gantry 4 nozzle (GTR4) and compared it to the original beam data in terms of beam parameters and dosimetry with the Faraday Cup [159, 160].
During the process of this work, the GTR4 model was further developed, in particular changes in the nozzle design. IC2/3 (see Figure 2.8 b)) developed by IBA and the Laboratory for Corpuscular Physics is part of the current nozzle design at WPE [66]. It was modeled for TOPAS. Both ICs are equipped with five Mylar electrodes, using a gold coating for dose and position measurement. The difference between IC2 and IC3 is the segmentation of the sensor. IC2 is segmented in the X-direction, IC3 in the Y-direction. The strips are 4.8 mm wide and in increments of 5 mm. The water equivalent thickness of the IC2/3 system is 187 $\mu$m [66]. A TOPAS graphic model of IC2/3 is shown below:

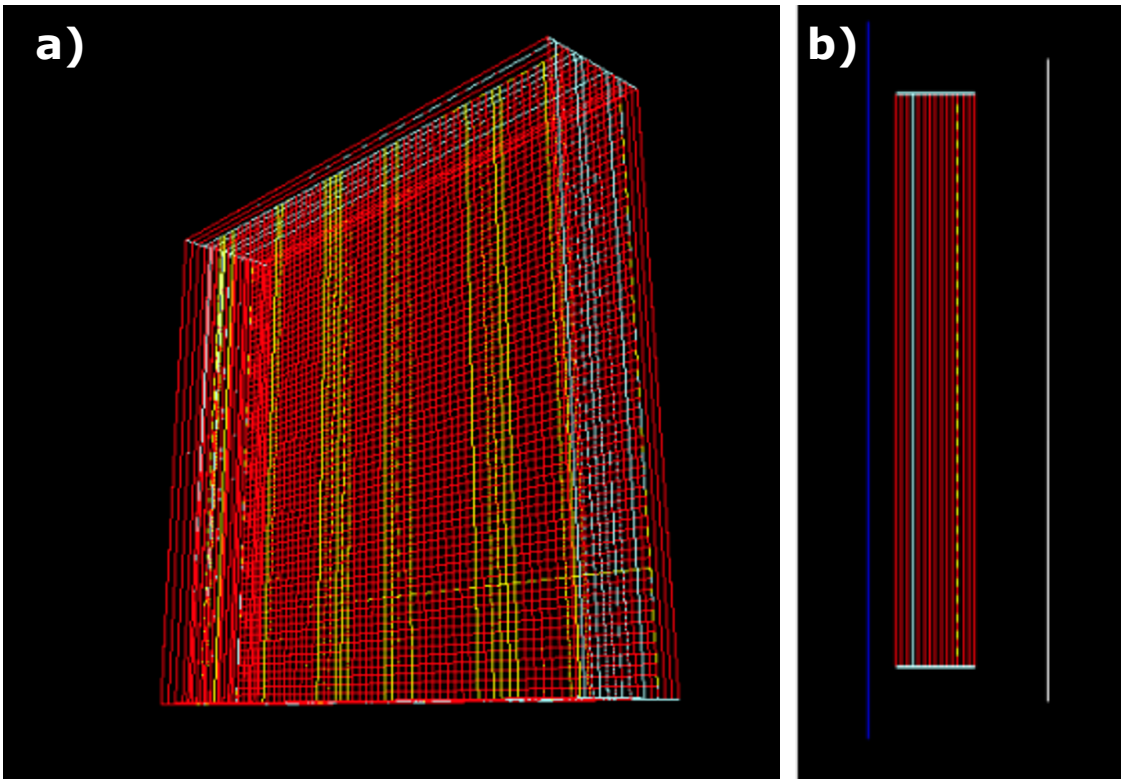


**Figure 3.10:** Changes in the TOPAS scanning nozzle model: a) New IBA IC2 and IC3 model according Courtois et al., which is installed at WPE [66]. The meaning of the colors are: red corresponds to Mylar electrodes, yellow corresponds to gold coatings and lightblue are the air areas between the electrodes. b) New position and material of the three last nozzle components. In the updated GTR4-model, the three components are located outside of the vacuum chamber. From left to right: Titanium foil (exit of vacuum chamber), IC2/3 and Kevlar® exit window.

The 3D model displays the Mylar electrodes in red, the gold coatings of the electrodes in yellow and the air gaps of the IC in light blue. Due to the zoom and orientation of the model, color overlay artifacts can occur as displayed in Figure 3.10 a) and b).
Another change in the GTR4 model is the exit window after the vacuum region in the nozzle, which is shown as a blue line in Figure 3.10 b). Titanium was assigned to the material. The last exit window of the entire nozzle is measured and defined as material Kevlar®(white line in Figure 3.10 b)).

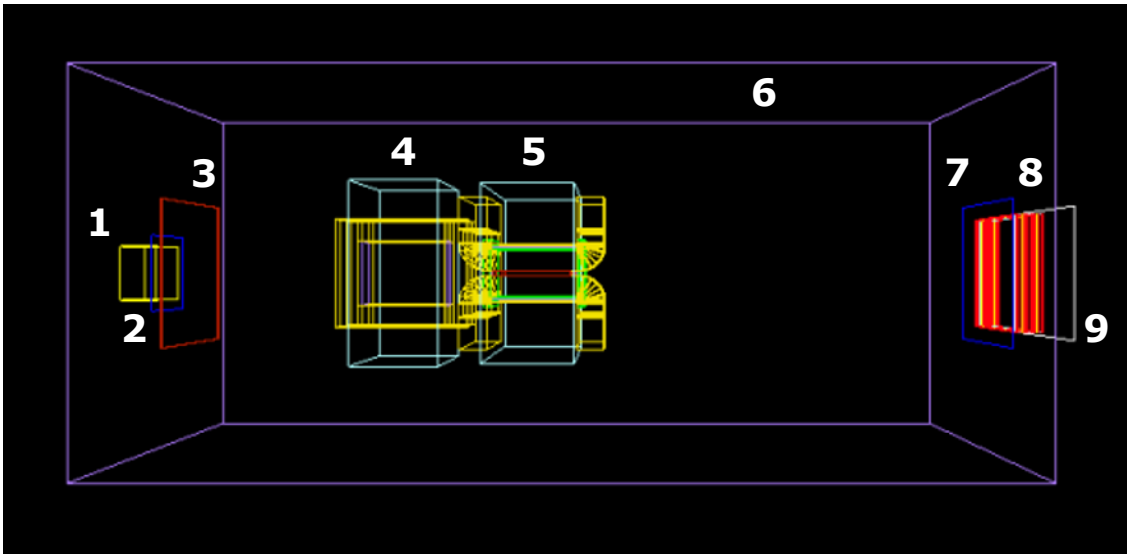


**Figure 3.11:** TOPAS scanning nozzle model. The proton beam is delivered and is going to several components numbered as 1-9. From left to right: (1) end of beam line called here vacuum chamber, (2) titanium foil or vacuum window, (3) the first ion chamber (IC1) followed by the scanning magnets in X-direction (4) and Y-direction (5), (6) forms the nozzle vacuum box, which is terminated by two titanium foils (2,7), (8) are the ion chamber 2 (IC2) and 3 (IC3). At the end, the Kevlar® exit window (9) is located.

Considering Figure 3.11, in a real system the proton beam is coming from the left side from the vacuum beam line (vacuum box 1) and enters the nozzle at the titanium foil (2), which separates the beam line vacuum (1) and the vacuum box (6). A first monitoring of the beam inside the nozzle is performed at the first ion chamber (IC1, (3)) followed by the scanning magnets in X-direction (4) and Y-direction (5). The three components (3), (4) and (5) are located inside of the vacuum box, which is terminated by two titanium foils (2 and 7). The second titanium foil (7) forms the end of the vacuum. Behind, the next beam monitoring takes place with IC2 and IC3, compare Fig. 3.10. The numbers (7), (8) and (9) form the snout and the Kevlar window is the last window of the system in front of the patient, the measuring instrument or the isocenter. Compared to the technical drawing in Figure 2.8, the X-ray tube and the quads are missing in the TOPAS model. Both components can be neglected, because they do not contribute to the nozzle water equivalent thickness ($WET$). The TOPAS model is a simplification, since not all components are identical to the IBA machine.
In TOPAS, the origin is defined in the isocenter. The distance between a point and the isocenter is defined by the Z-coordinate, so that all mapped components in Figure 3.11 lie along the negative Z-coordinate. Objects are controlled by their position specified as half-length (HL). Table 3.10 shows the Z-positions of all nozzle components. There are two values for the Kevlar® exit window, one for the standard fixed snout in GTR4 and

| Number | Component name | Z-distances to isocenter [cm] |
|---|---|---|
| 1 | Vacuum chamber | −295.000 625 |
| 2 | Titanium foil 1/vacuum window | −290.000 000 |
| 3 | Ion chamber 1 | −283.200 000 |
| 4 | Scanning magnet X | −221.500 000 |
| 5 | Scanning magnet Y | −184.600 000 |
| 6 | Vacuum box | −182.355 000 |
| 7 | Titanium foil 2 | −63.400 000 |
| 8 | Ion chamber 2 & 3 | −57.400 000 |
| 9 | Kevlar® window | -47.393000 & -51.100000 |

**Table 3.10:** Z-distances to the isocenter of the TOPAS scanning nozzle components. The Kevlar® exit window has two parameters that can be attributed to the different snout models for the two different pencil beam gantry rooms 4 (-47.393 cm) and 2 (51.100 cm). The Z-values are negative because they are located upstream of the TOPAS zero point and the isocenter, respectively.

one for the moving snout in GTR2.

As shown in Figure 3.9, TOPAS requires the user parameter files that contain the information for processing by TOPAS. The structure of the user parameter files in this work is outlined in Figure 3.12. The main file for the scanning nozzle executed by the TOPAS application is named here Main.txt. This file includes further data from the .phsp and .header file, which together provide the content of the proton source. For this reason, Figure 3.12 does not use a fixed name with the .txt suffix, since the PHSP files for the proton source have a different name for each energy. This is also the case for the other names in Figure 3.12 without the .txt suffix. Furthermore, the data from the spot patterns are required, which define the protons per spot and the position of the spots via the magnetic field strength. The file Nozzle.txt contains similar to the name the single components of Figure 3.11 and Table 3.10 as well as imports subcomponents of the other text files (see Figure 3.12). The last file defines the target volume and allows the choice of a scorer type. More information about the scorer types can be found in the TOPAS manual [157].

In this work, the standard physics packages were applied: G4DecayPhysics, G4EMStandardPhysics_option4, G4IonBinaryCascadePhysics, G4HadronElasticPhysicsHP, G4StoppingPhysics, and the binary cascade for hadronic interaction QGSP_BIC [157].

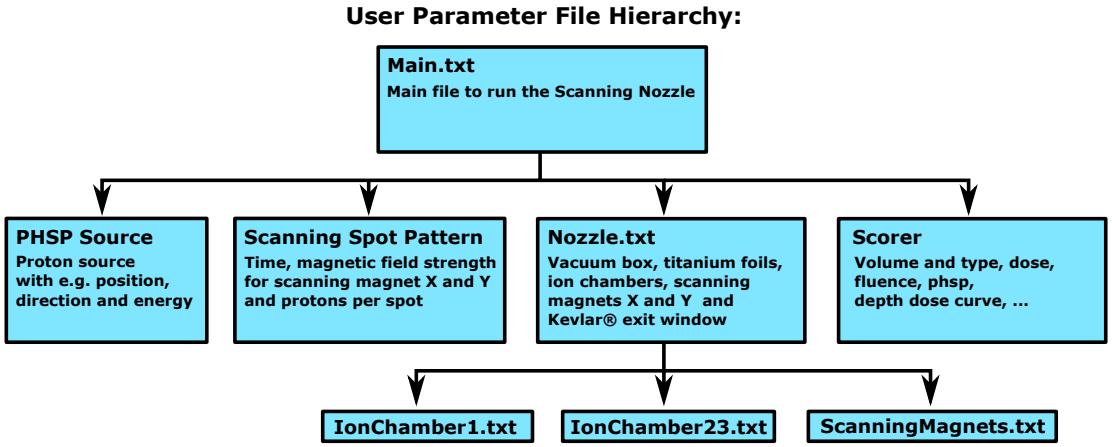


**Figure 3.12:** TOPAS scanning nozzle hierarchy: The top level user parameter file is the Main.txt file which includes the next four files in the hierarchy called PHSP Source, Scanning Spot Pattern, Nozzle.txt and Scorer. The Nozzle.txt uses further parameter files. The names without .txt extension are not fixed names for the files and therefore can have various names.

# Chapter 4

# Preliminary Work For The Surface And Skin Dose Determination

## 4.1 Determination Of Water Equivalent Thickness Factors

Each detector introduced in Chapter 3.1 has its own entrance material, e.g. entrance window for IC, before a charge is measured inside of the volume. The relation between the physical thickness and the resulting water equivalent depth ($WED$) of a material is necessary to define a precise classification in the depth dose curve. In this work, the following materials were considered in more detail:

| Material | Physical thickness | Density [g/cm$^3$] | Note |
|---|---|---|---|
| Polyester & active layer | 280 $\mu$m & 109 $\mu$m | 1.350 & 1.200 | EBT3 & HD-V2 |
| Kapton® | 25 $\mu$m, 50 $\mu$m, 75 $\mu$m | 1.420 | PTW extrapolation IC |
| Mylar | various sizes $\mu$m | 1.400 | Foils |
| PMMA | various sizes $\mu$m, mm | 1.180 | Wedge |
| RW3 | 1 mm, 2 mm, 5 mm, 1 cm | 1.045 | Slab phantom |
| Shonka C552 | 1 mm | 1.760 | IBA PPC05 |

**Table 4.1:** Materials to be examined for the $WET$ factor. The data was taken from the manuals [102], [106] , [141], [146], [161] and from NIST Standard Reference Database 124 [162].

PMMA is a standard material at WPE, which is well known from the experience with the IBA range shifters and from the production of apertures for patient specific treatment. The production of the introduced wedge in Subsection 4.2.5 from the WPE in-house workshop were produced from the same PMMA material as for the patient specific

compensator. Taking this into account the $WET$ factor of 1.15 can be adopted from the experience of the clinic. The same in-house knowledge exists for the material RW3, which is used at WPE for dosimetry and QA in form of a slab phantom (Ion Beam Applications Dosimetry, Schwarzenbrück, Germany). The applied $WET$ factor is therefore 1.03.
For all other materials from Table 4.1 further research in terms of the determination of a $WET$ factor was necessary. This happened with the following approaches:

- calculation with a theoretical approach
- simulating with a Monte Carlo approach
- experimentally with a MLIC.

The most practical approaches were the determination of the $WET$ factor by calculation the $WET$ with the stopping power relation and by simulations with TOPAS Monte Carlo. Both approaches were used for every material except for EBT3 and HD-V2 films. Due to the complex composition of the films, the experimental approach for a $WET$ determination was therefore chosen. However, this approach is only possible if a certain thickness and thus an observable separation of the proton ranges with and without the use of the material is available. As a result, this was feasible with a large number of 75 EBT3 films.
In the following subsections the respective approach will be further introduced. The investigated energies are 100.0 MeV, 150.0 MeV, 200.0 MeV and 226.7 MeV and are covering the IBA Proteus Plus range.

### 4.1.1 Water Equivalent Thickness Factor Determination With Stopping Power Calculations

The general equation for conversion or calculation for the unitless $WET$ factor can be done according the next formula from Ref. [163]:

$$t_{water} = t_{material} \cdot WET_{SP} \qquad \text{with} \tag{4.1}$$

$$WET_{SP} = (\rho_{material}/\rho_{water}) \cdot (S_{material}/S_{water}) \tag{4.2}$$

The variables are thickness $t$ [unit of length], the density $\rho$ [g/cm$^3$] and the stopping power $S$ [MeV cm$^2$/g]. Stopping Power data can be obtained for various materials and required energies from the NIST-Pstar data base. Combined, the following $WET$ factors are obtained for the investigated energy range:

| Energy [MeV] | $WET_{SP,Kapton}$ | $WET_{SP,Mylar}$ | $WET_{SP,ShonkaC552}$ |
|---|---|---|---|
| 100.0 | 1.30 | 1.30 | 1.55 |
| 150.0 | 1.30 | 1.30 | 1.56 |
| 200.0 | 1.30 | 1.30 | 1.56 |
| 226.7 | 1.31 | 1.31 | 1.56 |
| Mean | 1.30 | 1.31 | 1.56 |
| SD [%] | 0.14 | 0.13 | 0.16 |

**Table 4.2:** $WET$ factors determined by the stopping power approach.

### 4.1.2 Water Equivalent Thickness Factor Determination With TOPAS Monte Carlo Simulations

Implemented in TOPAS (Subsection 3.2), the idea behind the simulation approach was to simulate Bragg Peak curves with the investigated material as build-up in front of the phantom and none build-up. The comparison between the two the Bragg Peak curves shows a proton range shift. With the knowledge of the thickness of the build-up material it is possible to calculate the $WET$ factor.
The material build-up was modeled as a rectangular block with a thickness of 1 cm. To simplify the whole simulation, standard settings for TOPAS simulation were used. The proton beam had a field size of 10 x 10 cm². Only the energy was adapted and the material was changed according the materials calculated in Table 4.2. Depth doses were scored in a water phantom with the insert of the material build-up in front of the water tank and without. An example for a shifted 200.0 MeV Bragg Peak curve with the build-up insert of 1 cm Kapton® compared to a reference (only water) is displayed in Figure 4.1. As visualized in the plot of Figure 4.1, it is required to fit the scored data points to obtain a value at R80. This was executed in gnuplot using a *cspline* and an export of the values to a table. Then the range shift results to (named here as $WET_{R80}$):

$$WET_{R80} = R80_{water} - R80_{material} \quad . \tag{4.3}$$

To obtain a $WET$ factor, one need to divide the R80 shift $WET_{R80}$ by the physical thickness $t$ of the investigating material:

$$WET_{MC} = \frac{WET_{R80}}{t_{material}} \tag{4.4}$$

Simulating the various materials as build-up and scoring the depth dose curves, the results in Table 4.3 were obtained with Equations 4.3 and 4.4 for the $WET$ factor by the MC approach.

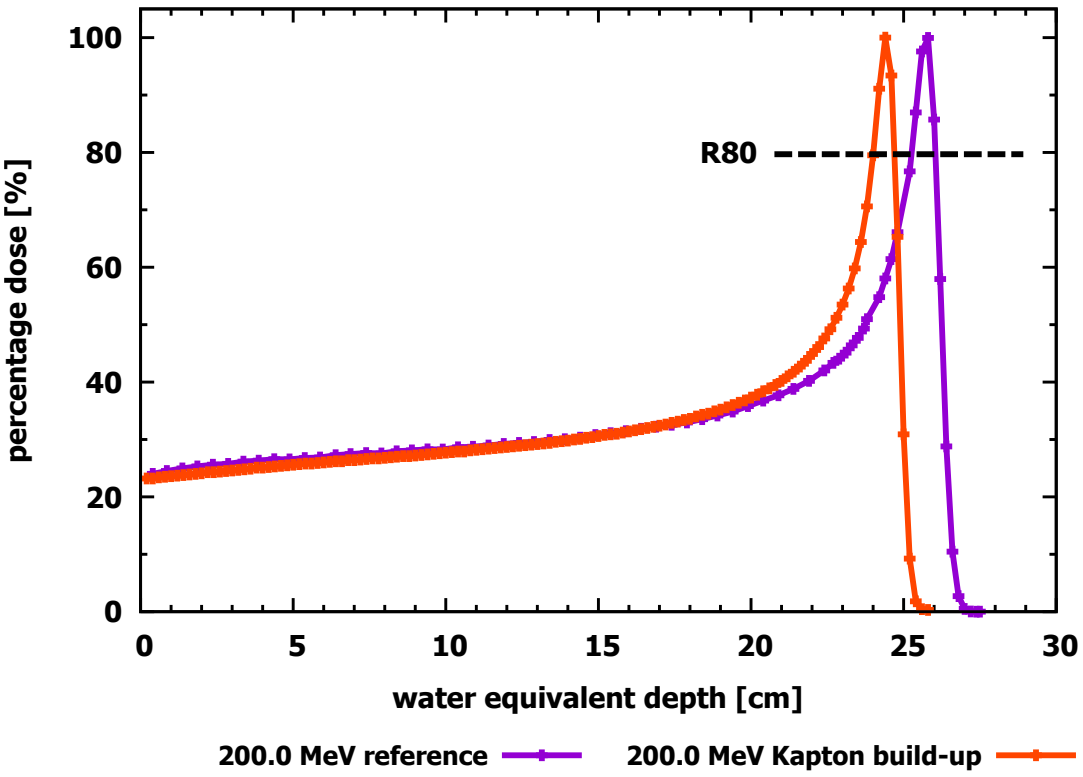


**Figure 4.1:** Two scored 200.0 MeV depth dose distributions in water. The reference curve is colored in purple. The change in range due to a 1 cm Kapton® build-up is colored in red. The difference of the distal $R80$ is required for $WET$ determination. For a better visualization, the points were connected.

| Energy [MeV] | $WET_{MC,Kapton}$ | $WET_{MC,Mylar}$ | $WET_{MC,ShonkaC552}$ |
|---|---|---|---|
| 100.0 | 1.27 | 1.28 | 1.56 |
| 150.0 | 1.30 | 1.30 | 1.56 |
| 200.0 | 1.31 | 1.32 | 1.56 |
| 226.7 | 1.32 | 1.32 | 1.56 |
| Mean | 1.30 | 1.31 | 1.56 |
| SD [%] | 1.62 | 1.41 | 0.19 |

**Table 4.3:** $WET$ factors determined by the MC approach.

### 4.1.3 Water Equivalent Thickness Factor Determination With The Experimental Approach

The experimental approach is similar to the MC approach, but with proton measurements instead of simulations. The proton range and thus the determination of R80 was measured with an MLIC (Subsection 3.1.1) including the IBA software OmniPro-Incline. The setup consisted of an aligned Zebra (on its marks) and the room lasers in gantry room 4 (GTR4). The 75 EBT3 films in full dimension were placed and fixed in front of the Zebras entrance window. Like described in the subsections before, the investigated energies were 100.0 MeV, 150.0 MeV, 200.0 MeV and 226.7 MeV irradiated in a 10 cm x 10 cm pattern. The following table shows a more detailed step by step view on the experimental results:

| Energy [MeV] | Reference $R80$ [cm] | $R80_{75films}$ [cm] | $WET_{R80}$ [$\mu$m] |
|---|---|---|---|
| 100.0 | 7.78 | 5.12 | 354.7 |
| 150.0 | 15.81 | 13.13 | 357.3 |
| 200.0 | 26.06 | 23.39 | 356.0 |
| 226.7 | 32.31 | 29.60 | 361.3 |

**Table 4.4:** Results for the experimental $WET$ approach. The table shows reference R80 ranges (without build-up material), the R80 ranges obtained by irradiation 75 stacked films and the $WET_{R80}$, which is calculated from the difference of the ranges and the conversation to one film (in $\mu$m).

To summarize Table 4.4, the various R80 with and without build-up material were measured, subtracted and converted to one film in micrometer length. With the physical depth of 280 $\mu$m and according to Equation 4.4 the following $WET_{exp}$ factors were determined for the film:

| Energy [MeV] | $WET_{exp}$ |
|---|---|
| 100.0 | 1.27 |
| 150.0 | 1.28 |
| 200.0 | 1.27 |
| 226.7 | 1.29 |
| Mean | 1.28 |
| SD [%] | 0.81 |

**Table 4.5:** Film $WET_{exp}$ factors determined by the experimental approach.

### 4.1.4 Summary Of The Water Equivalent Thickness Calculations

The remaining $WET$ factors for the various materials were investigated by three different approaches. The results are available in the Tables 4.2, 4.3 and 4.5. Taking the percentage standard deviation (SD) into account, the approach with stopping power calcualtions results in a low uncertainty of $< 0.2\%$. The MC approach shows a variety between 0.2% and 1.6% and a constant $WET_{MC}$ factor for the material with the highest density: Shonka C552. The classification for the experimental approach is with an SD of 0.8% within the other two approaches. Further, the mean $WET$ factor over all energies is equal for the three materials Kapton®, Mylar and Shonka C552 in Table 4.2 and 4.3. Table 4.6 shows the $WET$ factors applied for this work.

| Material | $WET$ |
|---|---|
| Kapton® | 1.30 |
| Mylar | 1.31 |
| PMMA | 1.15 |
| RW3 | 1.03 |
| EBT3 & HD-V2 | 1.28 |
| Shonka C552 | 1.56 |
| max. uncertainty | 1.6% |

**Table 4.6:** Applied $WET$ factors in this study.

For all materials in Table 4.6, the maximum SD is generously defined as the uncertainty for $WET$ factors. This considers the comparison of all three methods, the low energy dependence of the $WET$ factors and the already known $WET$ factors from the WPE.
For a classification of a measurement into the depth dose curve, the $WET$ factor multiplied with a thickness $t$ of a material is used to determine the water equivalent depth ($WED$):

$$WED = WET * t_{material} \quad . \tag{4.5}$$

## 4.2 Gafchromic™ Film Calibration

### 4.2.1 Film Dose Calibration with Proton Fields

A film calibration is required for the readout of the films. A certain number of films are irradiated to obtain a relationship between dose and color channel/grey value. This allows an interpolation of intermediate values, so that a range of dose is usable. In this work, the calibration was performed for two types of films: EBT3 and HD-V2 films. It is important that the calibration is applied accordingly for a lot of films that were produced in the same period of time. Accurate dose was acquired using a EXRADIN miniature Shonka T1 (SN: T1#XG101022) ionization chamber. The irradiation of the fields and the adjustment of the MU was done via so-called .pld files, which is the input format for the IBA machine. There, all necessary data for the machine are provided: Layer, spot, energy, MU per Layer and the total MU. The field parameters are:

| Parameter name | Parameter value |
|---|---|
| energy | 150.0 MeV |
| range | 157 mm |
| field size | 3 x 3 $cm^2$ |
| modulation | 0 |
| spot spacing | 1 mm |
| number of spots | 961 |

**Table 4.7:** Field parameters of the .pld file for the calibration irradiation.

The dose steps should cover the range from 0.5 to 5.0 Gy. The chamber was positioned at a $WED$ of 3 cm and the isocenter was at the same depth. The photo in Figure 4.2 a) shows the chamber inside the PMMA T1 adapter. The red laser crosshair is representing the isocenter position. An X-ray image followed by movement of the table was used to fine-tune the setup. A follow-up X-ray image verifies the shifted correction and the proper position of the chamber. The T1 chamber was connected to an IBA Dose 1 dosimeter to read the measurements. The operating voltage of the chamber is +300 V.

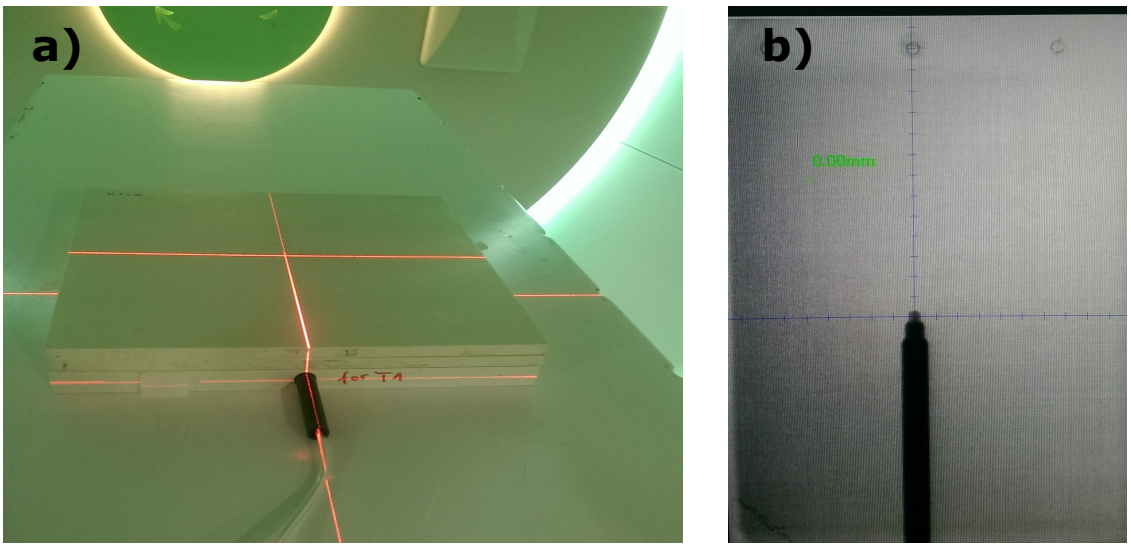


**Figure 4.2:** EXRADIN T1 dose measurement setup: a) The EXRADIN T1 is positioned in the isocenter and the measurement depth is 3 cm PMMA. b) In addition to laser alignment, fine correction and adjustment were performed and verified in an X-ray image.

The 150.0 MeV .pld file with the properties from Table 4.7 was modified according to the MUs in Table 4.8 and the field was irradiated. The measured value $M$ can be read at the Dose 1 electrometer. The conversion of the measured value $M$ in nC to a physical dose $D_M$ in Gy is done according to the Formula 2.13 and is extended to:

$$D_M = M \cdot N_{D,w,Q0} \cdot k_{Q,Q0} \cdot k_{pol} \cdot k_s \cdot k_{elec} \cdot k_{T,p} \quad ; \quad [\mathrm{Gy}]\,. \tag{4.6}$$

The individual variables are defined below:

- $M$: Display of the dosimeter, here the subtraction of zero is included.
- $N_{D,w,Q0}$: Calibration factor for the absorbed dose to water.
- $k_{Q,Q0}$: Correction factor of the beam quality.
- $k_{pol}$: Correction factor of polarity.
- $k_s$: Correction factor of saturation.
- $k_{elec}$: Correction factor of the electrometer.
- $k_{T,p}$: Correction factor of air density, where the factor is calculated from the reference conditions for temperature $T_0$= 293.15 K and pressure $p_0$= 1013.25 hPa: $k_{T,p} = \frac{p_0}{p} \cdot \frac{T}{T_0}$.

| MU | $M$ [nC] | Dose $D_M$ [Gy] |
|---|---|---|
| 44.2 | 0.882 | 0.51 |
| 88.3 | 1.767 | 1.02 |
| 132.5 | 2.656 | 1.53 |
| 176.6 | 3.528 | 2.03 |
| 220.9 | 4.411 | 2.53 |
| 261.1 | 5.222 | 3.00 |
| 304.6 | 6.117 | 3.51 |
| 348.1 | 6.972 | 4.01 |
| 391.6 | 7.849 | 4.51 |
| 435.1 | 8.713 | 5.01 |

**Table 4.8:** The table describes the used MUs of the irradiated proton fields, the charges of the EXRADIN T1 chamber and the conversion to a physical dose in Gy.

Using the correction factors of the EXRADIN T1 calibration certificate and the measurement conditions, the following formula is obtained:

$$D_M = M\ [nC] \cdot 10^{-9} \cdot 5.706 \cdot 10^{8}\ [\text{Gy/C}] \cdot 1.006 \cdot 1.000 \cdot 1.002 \cdot 1.000 \cdot 0.999\ [\text{Gy}]\,. \quad (4.7)$$

The Formula 4.7 yields to the dose results presented at Table 4.8.

### 4.2.2 Gafchromic™ Film Irradiation

Both Gafchromic™ film types are 8 inch x 10 inch, which is the equivalent to 20.3 cm x 25.4 cm. The EBT3 batch had the number 12121702. The EBT3 films were placed in landscape modus on a clean surface to subsequently sketch 5 cm x 5 cm film cutouts. To ensure the same orientation, the films were marked with a dot in the lower right corner (see EBT3 films in Fig. 4.3). To distinguish the irradiation order, the EBT3 films were labeled with the respective Gy number in the upper left corner.
There were only two films of the HD-V2 film delivered. All experiments had to be performed with these films, so the film dimensions were shortened to 2 cm x 2 cm. The active layer of a HD-V2 film is indicated by the manufacturer with a mark in the upper right corner. The markings for the order in this work were labeled on the polyester layer. In the last step before actual irradiation, the films were cut apart along the outlined mark. The following actions were taken to reduce film uncertainties: The markings were made without touching the films during writing. This means that no grease spots or similar are transferred during subsequent film scanning. Similarly, the intermediate storage and work steps must be performed from above on a suitable work surface that does not damage the films.
Films were irradiated at 3 cm $WET$ similar to the T1 chamber at isocenter, i.e., 2.9 cm

PMMA plates were placed on each film. Irradiation was performed using the 150.0 MeV .pld file with the properties from Table 4.7. The results of irradiation are shown in Fig. 4.3. There, the dose range is shown from 0.0 Gy to 5.0 Gy for the EBT3 films and 0.0 Gy to 10.0 Gy for the HD-V2 films. The 0 Gy film is representing an non-irradiated reference film. The figure shows the different discoloration of the two film types. The EBT3 films are sensitive to lower doses, i.e. they dye more with increasing doses. The HD V2 films are less sensitive to lower doses. To the eye, the differences in discoloration are much smaller.
After irradiation, there is an after-effect of irradiation due to the chemical reaction in the active layer. It is recommended to let the films rest after irradiation and to scan the film series to be compared at the equal time. In this work, a period of 24 $\pm$1 h was followed [164].

### 4.2.3 Scanning Of The Gafchromic™ Films

As mentioned in subsection 3.1.3 WPE has a EPSON Expression 10000XL scanner, which is required for film processing. A sketch is given in Figure 4.4 a). The scanner has a transparent reading area that is closed during scanning, similar to conventional scanners. The EPSON scanner has one scan direction. To ensure the reproducibility of the scanning process, a schaplone (Figure 4.4 b)) was used for each scan. This will always center the film on the scanner. Uniform positioning, especially in the center of the scanner, reduces scanner artifacts, such as uneven illumination at the edge of the scanner or light scattering [164, 165]. In addition to the reproducibility of the measuring position, the orientation of the film must also be consistent throughout the work. The orientation of the film can be distinguished by the original film's rectangular shape. With the help of the coating direction of the film the portrait or landscape format can be chosen. Depending on the orientation, there is a different film behavior during scanning [144, 166]. A visual example of the coating and alignment of the film is shown in Figure 4.4 c) and d). In order to stabilize the light source in the scanner, warm-up scans, so-called dummy scans, are performed.

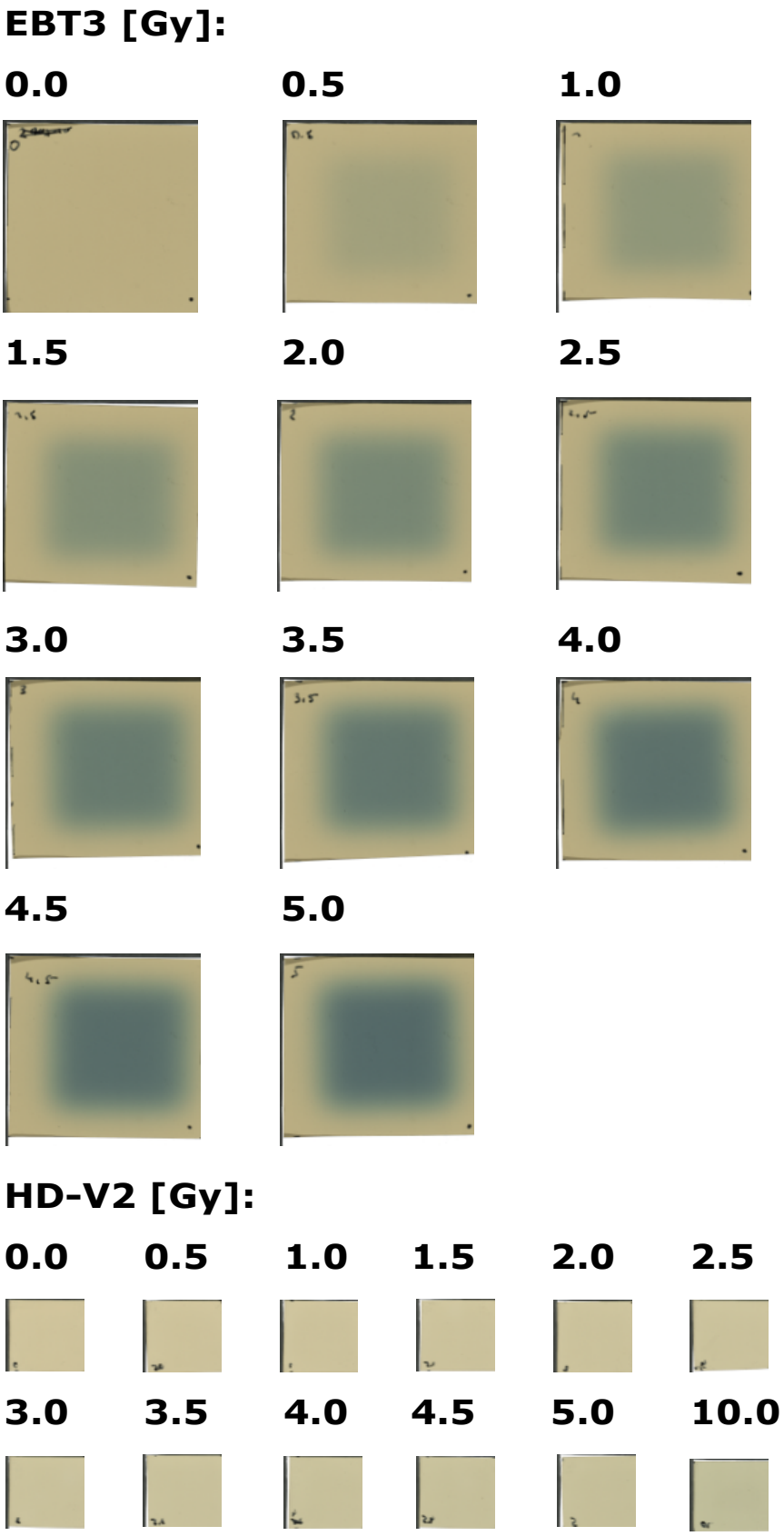


**Figure 4.3:** EBT3 and HD-V2 irradiated films for dose calibration. The dose ranges are 0-5 Gy for the EBT3 films and 0-10 Gy for the HD-V2 films.

In this work, ten scans are done before the actual irradiated films are scanned and stored. This procedure is also applied in other film protocols [167, 168].
The supplied Epson scan software is provided to scan the films. There, all image correction options that can falsify the original image are switched off. Other settings are the 48-bit color mode (16-bit per color channel red, green and blue), 150 dpi, transmission mode and storage in .tiff format.

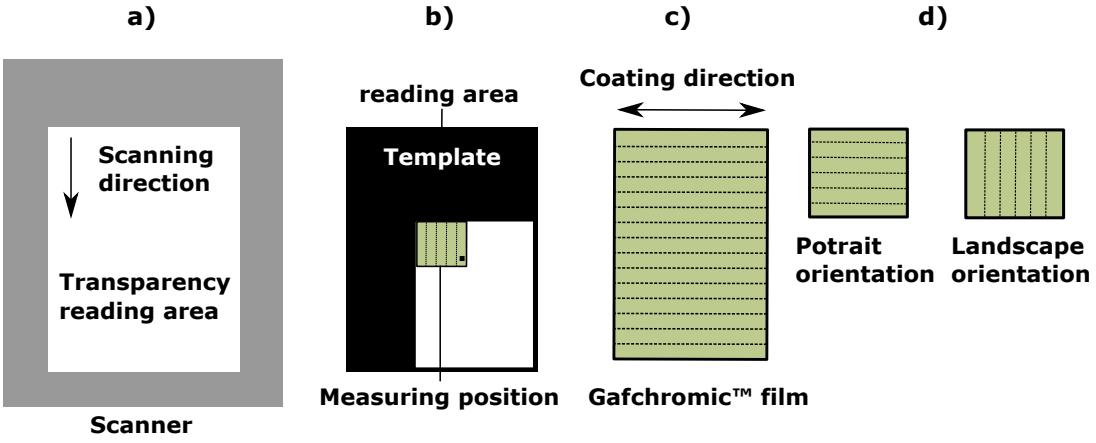


**Figure 4.4:** Scanner and Gafchromic™ film orientation. a) Scanner with reading area and scanning direction. WPE is using an EPSON Expression 10000XL scanner. b) Sketch of the reading area. A template was applied to ensure a reproducible measuring position. Here it is the center of the reading area. c) A Gafchromic™ film with its coating direction [169]. d) Depending on the orientation of the film during scanning, the response of the film varies. Here the landscape orientation was used, i.e. the coating direction of the film is parallel to the scan direction. As an alternative orientation, the portrait orientation is also available (reproduction according Ref. [169]).

### 4.2.4 Usage of FilmQA™

FilmQA Pro 2014 (Ashland, Convington, USA) software is used to create the calibration curve and to analyze the films. For the calibration curve, all individually scanned films must be available as one .tiff file, arranged similar as in Figure 4.3. This can be sorted and created within FilmQA Pro. During calibration, the small squared ROI is placed in the center of the irradiated area. This is followed by the assignment of the irradiated dose to the films and the recommended calibration model equation (reciprocal linear) of

$$X(D) = A + \frac{B}{D - C} \quad , \tag{4.8}$$

where X(D) represents the color channel, D is the dose in Gy, and A,B, and C are the fitting variables. The color channel X(D) is unitless and consists of the irradiated pixel value $PV_{irr}$ divided by $PV_0$=65536 (16-bit value range) [52]. The resulting calibration curve with the three color channels red, green and blue for the EBT3 films is shown in Figure 4.5.

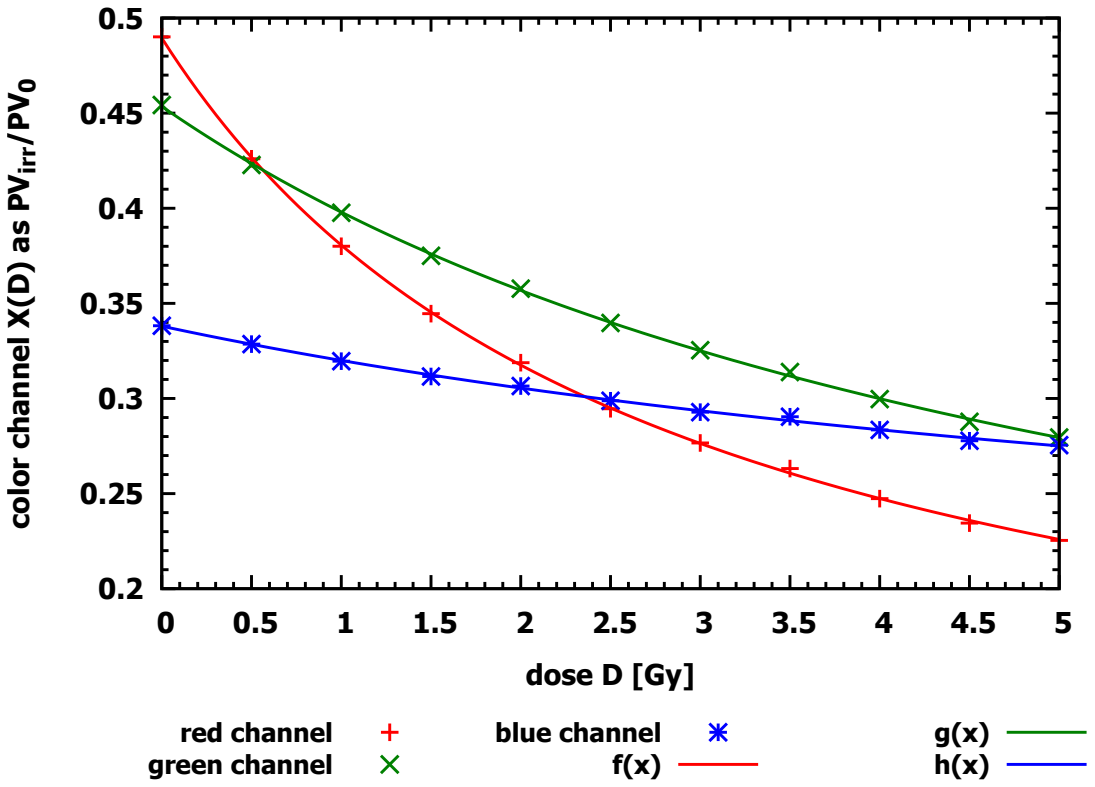


**Figure 4.5:** Calibration curve for the three color channels red, green and blue for the EBT3 film lot.

The values for the fit variables A, B and C are extracted from FilmQA Pro and are presented in Table 4.9 below.

| Channel | Fit variable | | |
|---|---|---|---|
| | A | B | C |
| red | 0.038 | 1.549 | -3.469 |
| green | -0.007 | 3.629 | -7.924 |
| blue | 0.122 | 2.275 | -10.408 |

**Table 4.9:** Resulting fit variables for the EBT3 calibration. With the formula $X(D) = A + \frac{B}{D-C}$ one obtains the calibration curve for the EBT3 film displayed in Figure 4.5.

The calibration curve for the HD-V2 film was extended by a calibration point up to 10 Gy. The near-linear curve shows the low-sensitivity region of the HD-V2 film which is typically selected for dose magnitudes of ≥10 Gy, see Ref [146] and Table 4.10.

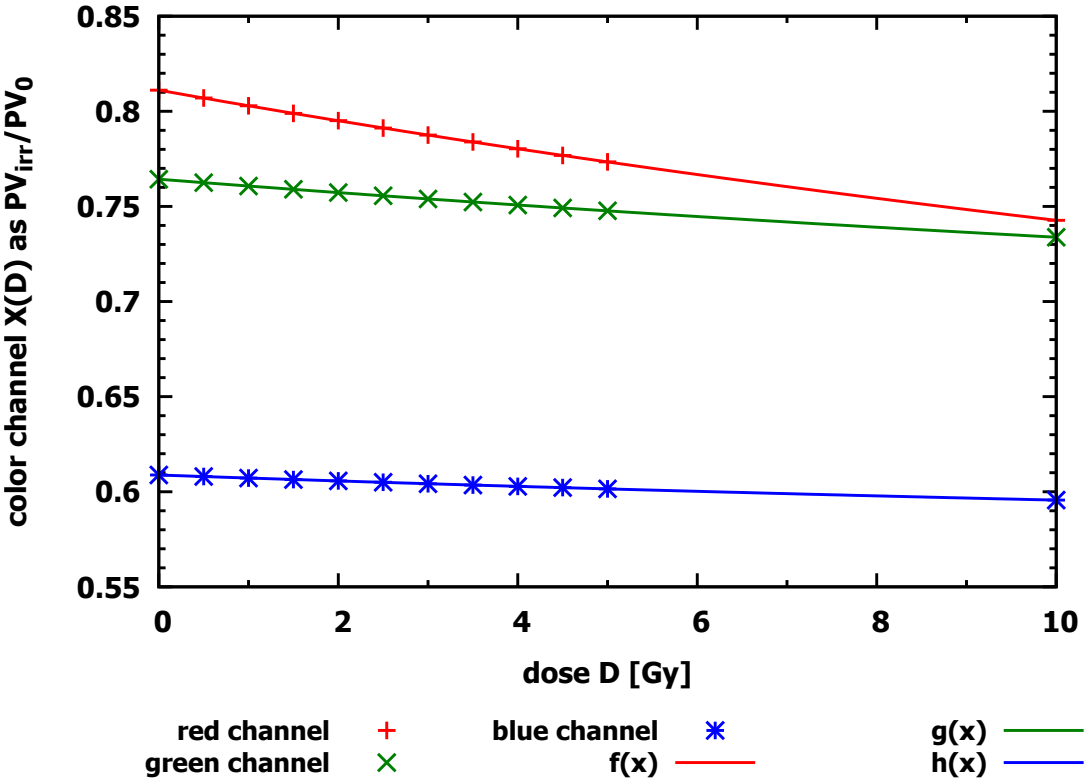


**Figure 4.6:** Calibration curve for the three color channels red, green and blue for the HD-V2 film lot.

The corresponding fit variables for A, B, and C for the HD-V2 calibration are listed in Table 4.10.

| Channel | Fit variable | | |
|---|---|---|---|
| | A | B | C |
| red | 0.443 | 16.107 | -43.752 |
| green | 0.579 | 9.395 | -50.705 |
| blue | 0.539 | 3.003 | -43.033 |

**Table 4.10:** Resulting fit variables for the HD-V2 calibration. With the formula $X(D) = A + \frac{B}{D-C}$ one obtains the calibration curve for the HD-V2 film displayed in Figure 4.6.

### 4.2.5 Survey Of The PMMA Wedge

The PMMA wedge was produced by precision mechanics at WPE's in-house workshop. First, prototypes were made with a larger angle to see how the PMMA milling machines can render the tip of the wedge geometry. The successful tests subsequently allowed the production of a PMMA wedge with an angle of 10°. The following Figure 4.7 depicts the sketch and a photo of the wedge:

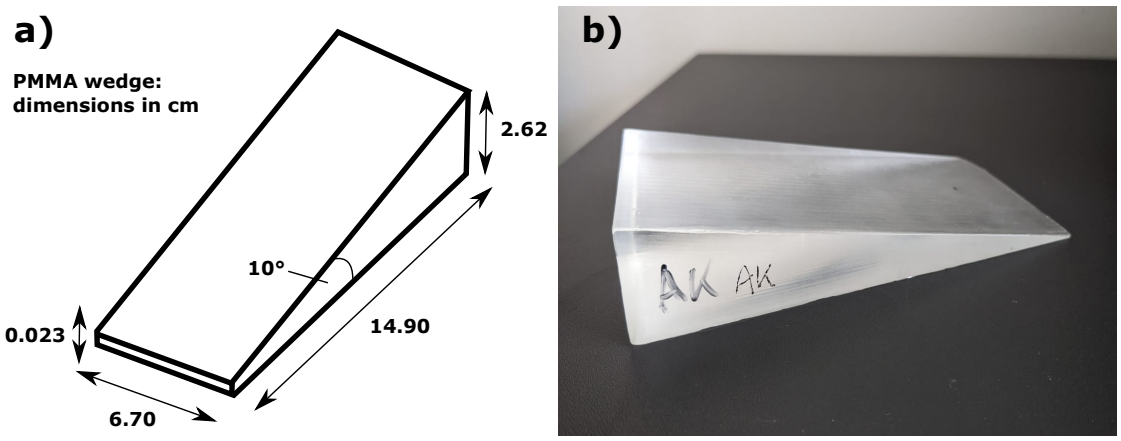


**Figure 4.7:** Concept, dimensions and photo of the PMMA wedge.

The geometry could be measured and the dimensions are given in Figure 4.7 a). For the dose measurement and the positioning in the depth dose curve, it is necessary to know how much PMMA is present in the first millimeters of the wedge. For this purpose, first the tip and then the thickness of the wedge was measured in 1 mm increments with a Tesa Hite 400 (height gauge). The thin scanning head has an accuracy of 0.005 mm. The measurement was taken for the first 10 mm. The following Table 4.11 describes the mean and standard deviation of 26 scans along the 6.7 cm wide wedge per measurement depth for the first 9 mm.

| Step | Tip | 1 mm | 2 mm | 3 mm | 4 mm |
|---|---|---|---|---|---|
| Thickness [mm] | 0.23±0.03 | 0.43±0.02 | 0.59±0.01 | 0.77±0.02 | 0.94±0.02 |
| Step | 5 mm | 6 mm | 7 mm | 8 mm | 9 mm |
| Thickness [mm] | 1.11±0.02 | 1.29±0.02 | 1.45±0.06 | 1.64±0.03 | 1.81±0.03 |

**Table 4.11:** Measured values for the thickness of the wedge at different positions. For reasons of clarity, only the first 9 mm are presented in the table.

From the measured data, the linear fit is

$$y = 0.1746 \cdot x + 0.2409 \tag{4.9}$$

applied to define the relation between the depth along the wedge (step, x) and the corresponding height (y) in the wedge. For a direct correlation into the water equivalent depth, the $WET$ factors for the film and PMMA were included. Thus, the entire thickness $y_{e,t}$ of wedge and film results to

$$y_{e,t} = 0.2009 \cdot x + 0.4579 \qquad . \tag{4.10}$$

## 4.3 Characterization Of The PTW Extrapolation Ionization Chamber

Similar types of extrapolation ICs have only rarely occurred in photon therapy ([109, 170, 171, 172]), where only Gerber et al. made use of a different PTW model and Camargo et al. even used the PTW model 23391 from this work. However, the paper by Camargo et al. was not published in a journal. The other two extrapolation ICs, on the other hand, were unspecified (Hanson et al. in Ref. [170]) or an in-house construction (Zankowski et al. in Ref. [109]) adapted from the work by Klevenhagen et al. [108]. The extrapolation IC has not yet been used in proton therapy. This means that it has to be reviewed whether this chamber is suitable for proton therapy and for this work. For this purpose, the chamber needs to be studied and characterized in more detail.
With three Kapton® entrance windows delivered with thicknesses of 25, 50, and 75 $\mu$m, the PTW extrapolation IC type 23391 is ideally qualified for the operation as classical ionization chamber for shallow depth measurements.

### 4.3.1 Electrode Gap

To determine an electrode gap, the parameters of some other ICs were first tabulated. In the context of voltage $U$ and the electrode gap $g$, the electric field strength can be calculated according to the formula

$$E = U/g \qquad [\mathrm{V}/mm]. \tag{4.11}$$

In the comparison of the data in Table 4.12 below, most of the ICs are applied with a bias voltage of 300 V and an electrode gap between 0.6 and 2 mm. In the case of the inner collecting electrode the extrapolation IC comes with a 30 mm diameter. That is comparable to Exradin T11 and to PTW Bragg Peak chamber. Comparing the electrode gap, a value of 2 mm can be applied. The electrode gap is adjusted on the micrometer screw. It is important to note that a display of 0 mm results in an actual electrode gap of 0.5 mm [106].

| Chamber name | $U$ [V] | $g$ [mm] | $E$ [V/mm] | Inner electrode diameter [mm] |
|---|---|---|---|---|
| IBA PPC05 | 300 | 0.6 | 500 | 9.9 |
| EXRADIN T11 | 300 | 2.0 | 150 | 20.0 |
| PTW Bragg Peak chamber | 300-500 | 2.0 | 150-250 | 40.8 |
| IBA Stingray | 150 | 1.0 | 150 | 120.0 |
| PTW Extrapolation IC | not defined | | - | 30.0 |

**Table 4.12:** Comparison of ionization chambers data. With regard to the diameter of the inner collecting electrode, the sizes of the Exradin T11 and the PTW Bragg peak chamber are comparable to those of the PTW extrapolation IC. The final values for $U$ and $g$ are not defined here for the PTW extrapolation IC in this table, as they will be introduced step-by-step in the next subsections. Chamber data were obtained from Ref. [102, 113, 173, 174].

### 4.3.2 Operating Range

The operating range of the ionization chamber is in the ion saturation range, i.e. approx. on a plateau of the current/voltage relationship (compare Fig. 2.4). To define the operating point, the chamber was irradiated three times at various voltages with a fixed electrode gap of 2 mm (1.5 mm on the micrometer display).

The setup consisted of the extrapolation IC placed on the table at a gantry angle of 270°. The chamber was connected to the PTW Tandem electrometer. The remote control of the PTW TANDEM was realized with an extension into the treatment control room and the PTW software MEPHYSTO. The voltage range of the electrometer was between 0 and 400 V, allowing measurements to be performed in 50 V increments. A 10 cm x 10 cm 150.0 MeV reference field was irradiated. Compared to other chamber readings, the measured charge of the extrapolation IC was high. To avoid irradiation

damage to the sensitive chamber, the MU were reduced from 1681 (WPE reference field) to 168.1. The plot below shows the normalized charge to 300 V plotted against the applied voltage.

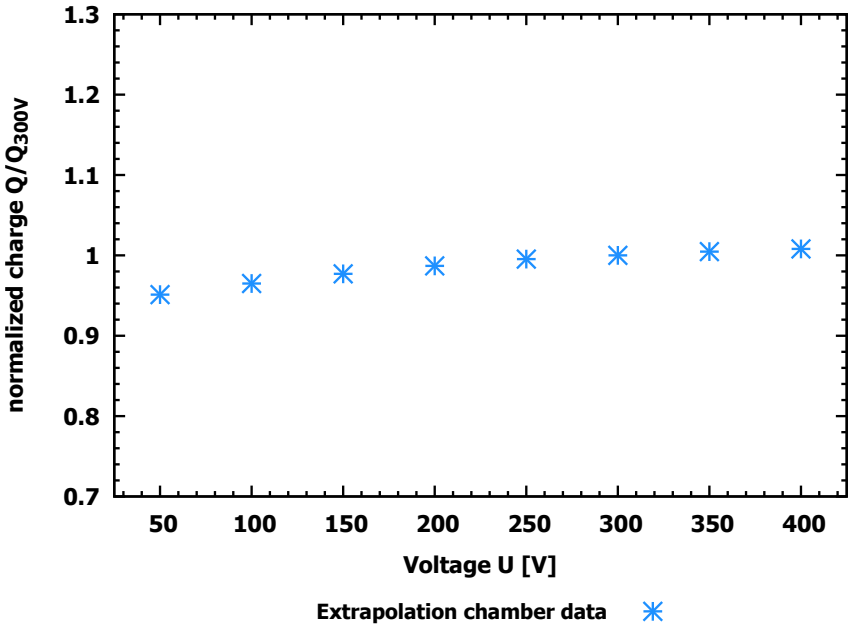


**Figure 4.8:** Operational range measurement of the PTW Extrapolation IC. The data was normalized to 300 V.

Accordingly, the line of the extrapolation IC is filled with the following values:

| Chamber name | $U$ [V] | $g$ [mm] | $E$ [V/mm] | Inner electrode diameter [mm] |
|---|---|---|---|---|
| PTW Extrapolation IC | 300 | 2 | 150 | 30 |

**Table 4.13:** Extrapolation IC operating values.

### 4.3.3 Charge To MU Linearity

Another test for ionization chambers applied in radiotherapy is a linear response at different MU. This dose to MU linearity or here charge to MU linearity is identified in this work by six different measurements:

- 33.62 MU, 67.24 MU, 117.67 MU, 168.1 MU, 336.2 MU and 504.3 MU

Figure 4.9 depicts the measured charge $Q$ in nC against the irradiated MU. The linearity of the data reflects the coefficient of determination with $R^2$=1.

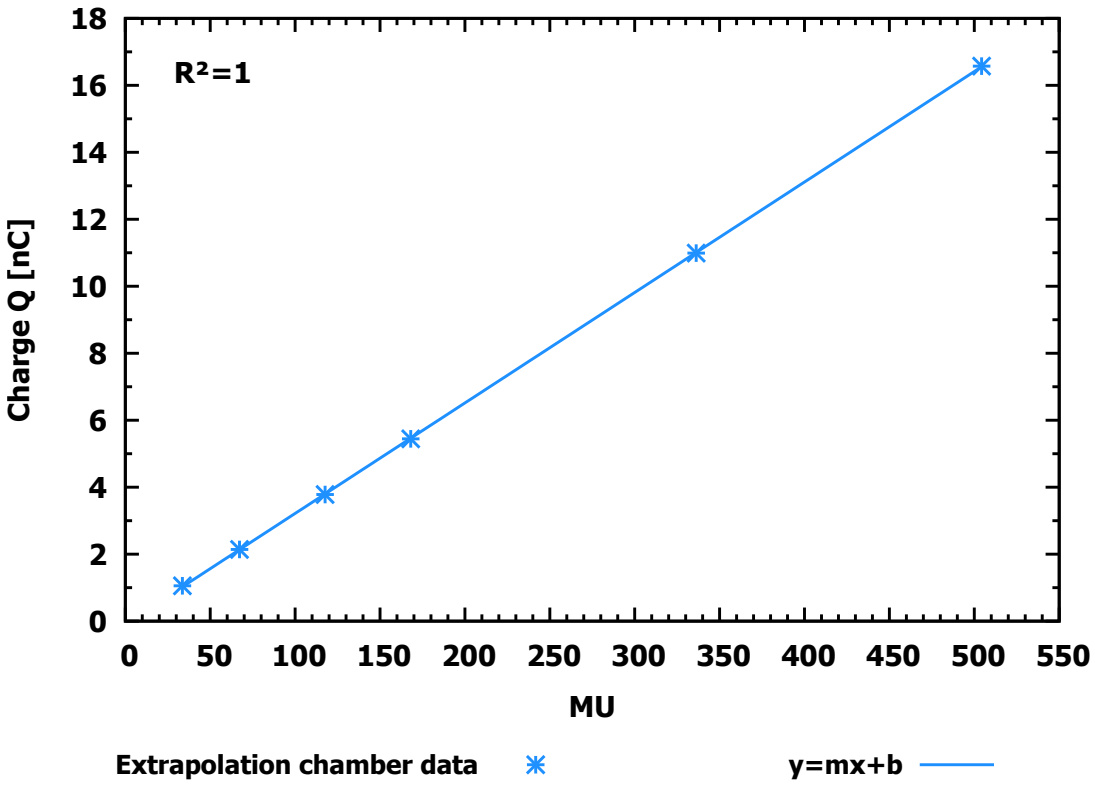


**Figure 4.9:** Charge to MU linearity of the PTW Extrapolation IC. The linearity of the data reflects the coefficient of determination with $R^2$=1.

## 4.4 Classification Of The Thermoluminescence Detector Into The Depth Dose Curve

As introduced in Subsection 3.1.2 *Thermoluminescence detector*, 2 mg TLDs were produced and used in this study. For a deeper understanding of the structure and thus to allow some classification of the TLD into a depth dose curve, a more detailed examination was performed. At TU Dortmund, there was the opportunity to perform a laser cut on a TLD using a TRUMPF Lasercell. It was cut in the geometric center. A further analysis of the thickness of the pressed-in powder layer on the aluminum substrate was carried

out with an electron microscope and its software at the physics chair E4 (TU Dortmund). Figure 4.10 a) depicts a laser cut of an investigated 2 mg TLD. Figure 4.10 b) shows an enlargement of the deepest part of LiF and some depth measurements marked with a red cross.

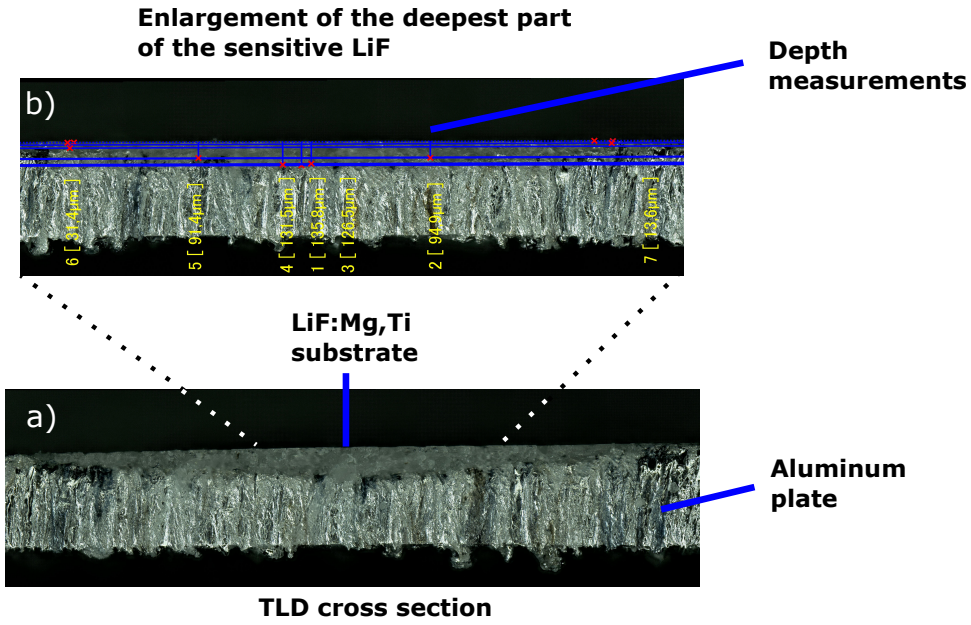


**Figure 4.10:** a) Cross section of a 2 mg TLD laser cut under the electron microscope. b) Example of depth measurements at the deepest expansion of the pressed-in LiF.

The geometric center of gravity of the volume of a paraboloid $V_S$ was chosen to determine the measurement depth. It describes the pressed-in thickness $h$ of the powder. The corresponding equation and calculation is:

$$V_S = h/3 \quad . \tag{4.12}$$

With the measured values recorded at the deepest point, the following result is obtained

$$V_S = (43 \pm 3)\ \mu m \quad . \tag{4.13}$$

## 4.5 TOPAS Particle Parameter Study

With TOPAS it is possible to determine the surface dose and to characterize the resulting particles, which were created from the interaction with proton and the other materials. Therefore, there are built in tools to track the particle fluence or the dose deposition of various particles. Due to the same physics library from Geant4, there are also different physics settings for TOPAS possible. The origin of the standard settings are the parameters which resulted best for the Massachusetts General Hospital [157]. For this work, the settings may need an adaption for the investigated problem.
The first TOPAS runs were done to identify the particle composition with a so called phase space scorer. The phase space scorer is tracking all particles, which are passing a cross section of a defined 2D plane. The setting was simplified without the nozzle and the scanning. Only a water tank was placed in the isocenter and the source was set to the position from the nozzle design. As a result the most scored particles are therefore:

- proton (primary + secondary)
- electron
- gamma
- neutron
- alpha
- deuteron

Based on these particle occurrences, the particle fluence and dose deposition in the first 10 mm of the water tank were analyzed for each individual particle.
The ranking presented in Table 4.14 is a result of both Figures 4.11 & 4.12. It shows that the ranking is not equal e.g. for the first three order of magnitudes. For this work, the dose deposition is more important, when determining the surface/skin dose at the beginning of the depth dose curve (investigated in Chapter 5). As a result there is a higher focus for the primary, secondary protons and the electrons in TOPAS (compare Table 4.14 dose results).

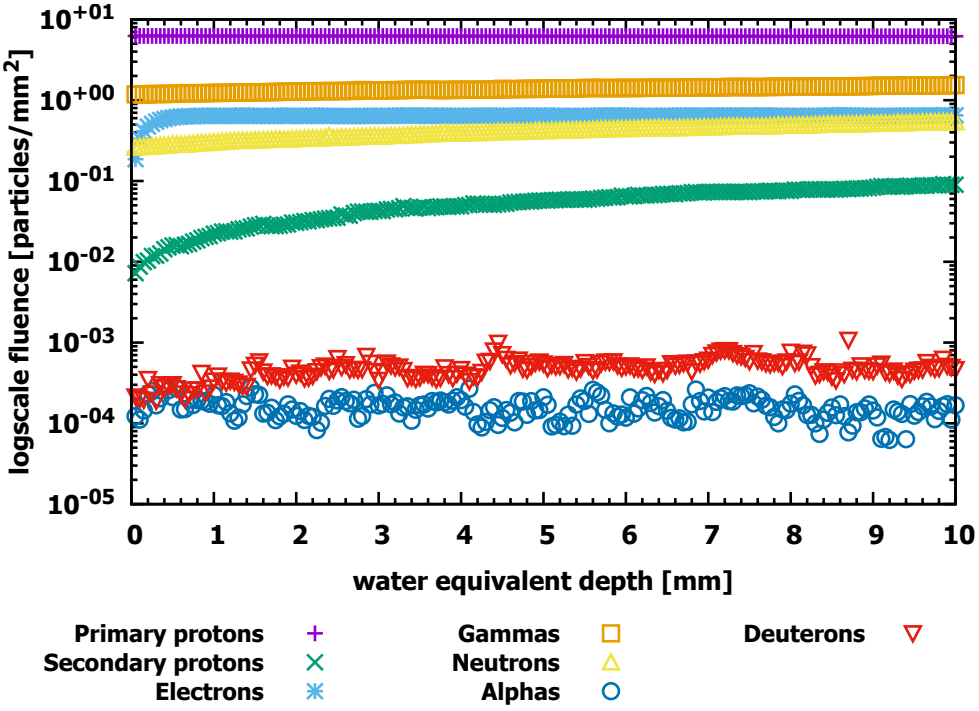


**Figure 4.11:** Particle fluence of the most common particles in the first 10 mm in a water tank scored in TOPAS.

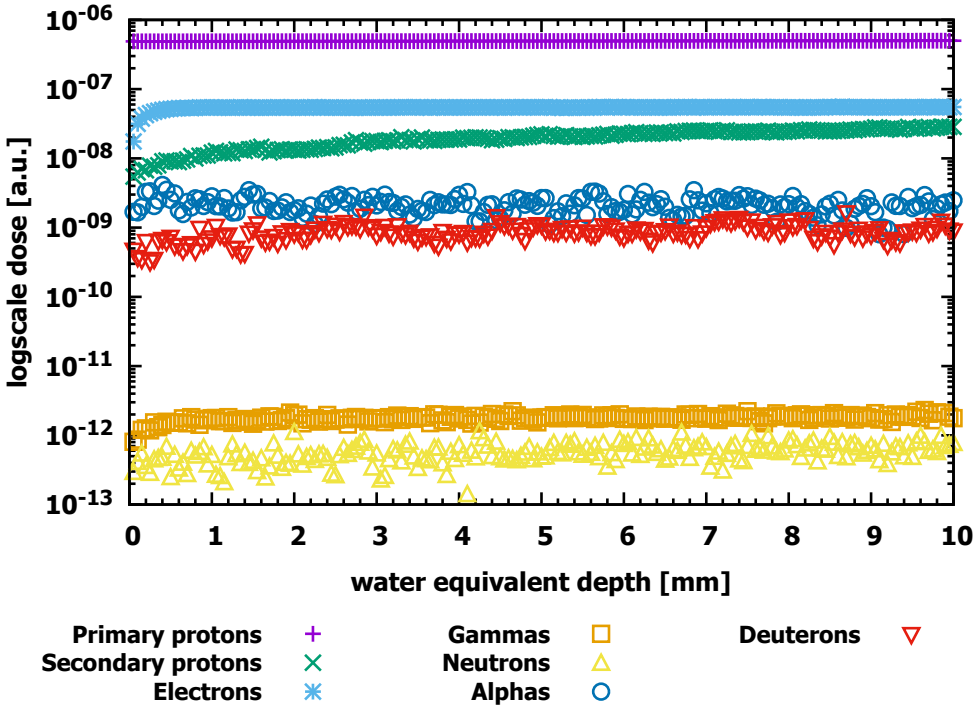


**Figure 4.12:** Dose to water deposition of the most common particles in the first 10 mm in a water tank scored in TOPAS.

| Ranking | Particle-fluence | Particle-dose |
|---|---|---|
| 1. | primary proton | primary proton |
| 2. | gamma | electron |
| 3. | electron | secondary proton |
| 4. | neutron | alpha |
| 5. | secondary proton | deuteron |
| 6. | deuteron | gamma |
| 7. | alpha | neutron |

**Table 4.14:** Rankings of particle fluence and dose deposition extracted from Figures 4.11 & 4.12.

Of the investigated changeable parameters, the TOPAS commmand *CutFor'particle typ'* had the greatest impact to the dose and fluence contribution at the surface region. The default setting is

$$\text{d:Ph/Default/CutForAllParticles} = 0.05 \text{ mm}.$$

That means, that every resulting particle with an energy translated to a range of >50 $\mu$m will be tracked and further proceeded in TOPAS. *CutFor* can also be named as range cut. As part of the analysis, the default value of 50 $\mu$m was compared to some adjusted values of 10 $\mu$m, 30 $\mu$m and 70 $\mu$m. For the focused particles (primary, secondary protons and electrons) there was only a visible effect on fluence and dose distribution for electrons. The graphical results are displayed in Figures 4.13 & 4.14. The lower the range cut, the more electrons are generated and more dose deposition by electrons is visible. The results from this investigation together with a further work of Wulff et al., who used TOPAS for IC calculations, are showing a need to adapt the range cut for various simulation scenarios [175, 176].
As a lower production cut reveals an impact to the shallow depth dose curve and therefore for the skin dose, the parameter for electrons was set to

$$\text{d:Ph/Default/CutForElectron} = 0.001 \text{ mm}.$$

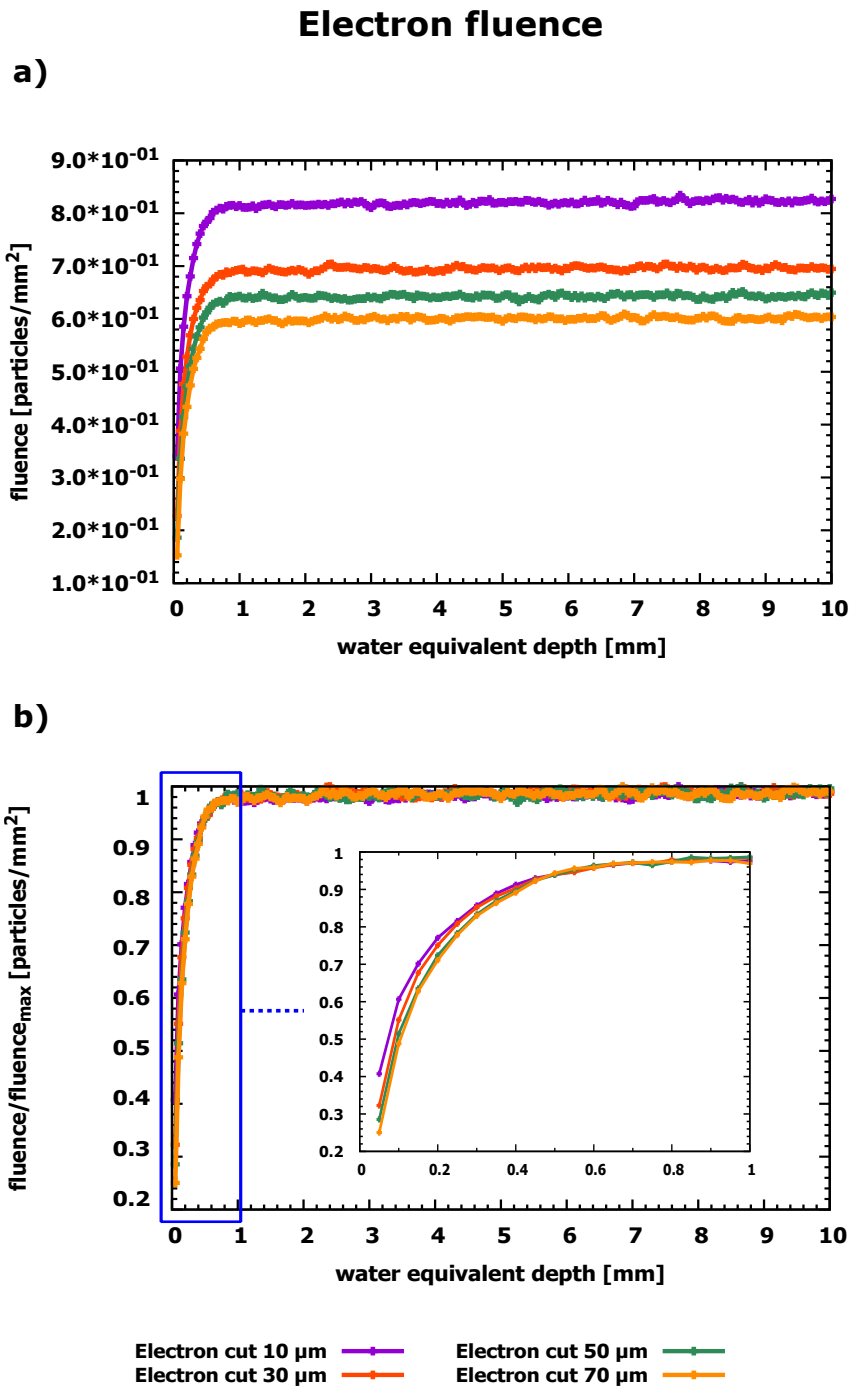


**Figure 4.13:** Various TOPAS range cut settings resulting on electron fluence in the first ten millimeters. a) Range cut of 10 $\mu$m, 30 $\mu$m, 50 $\mu$m (default) and 70 $\mu$m. The lower the range cut, the more electrons are generated in total. b) The fluence values were normalized to its maximum. The plateau region looks very similar, but a closer look into the first millimeter reveals again a gradation of fluence distribution due to range cut changes.

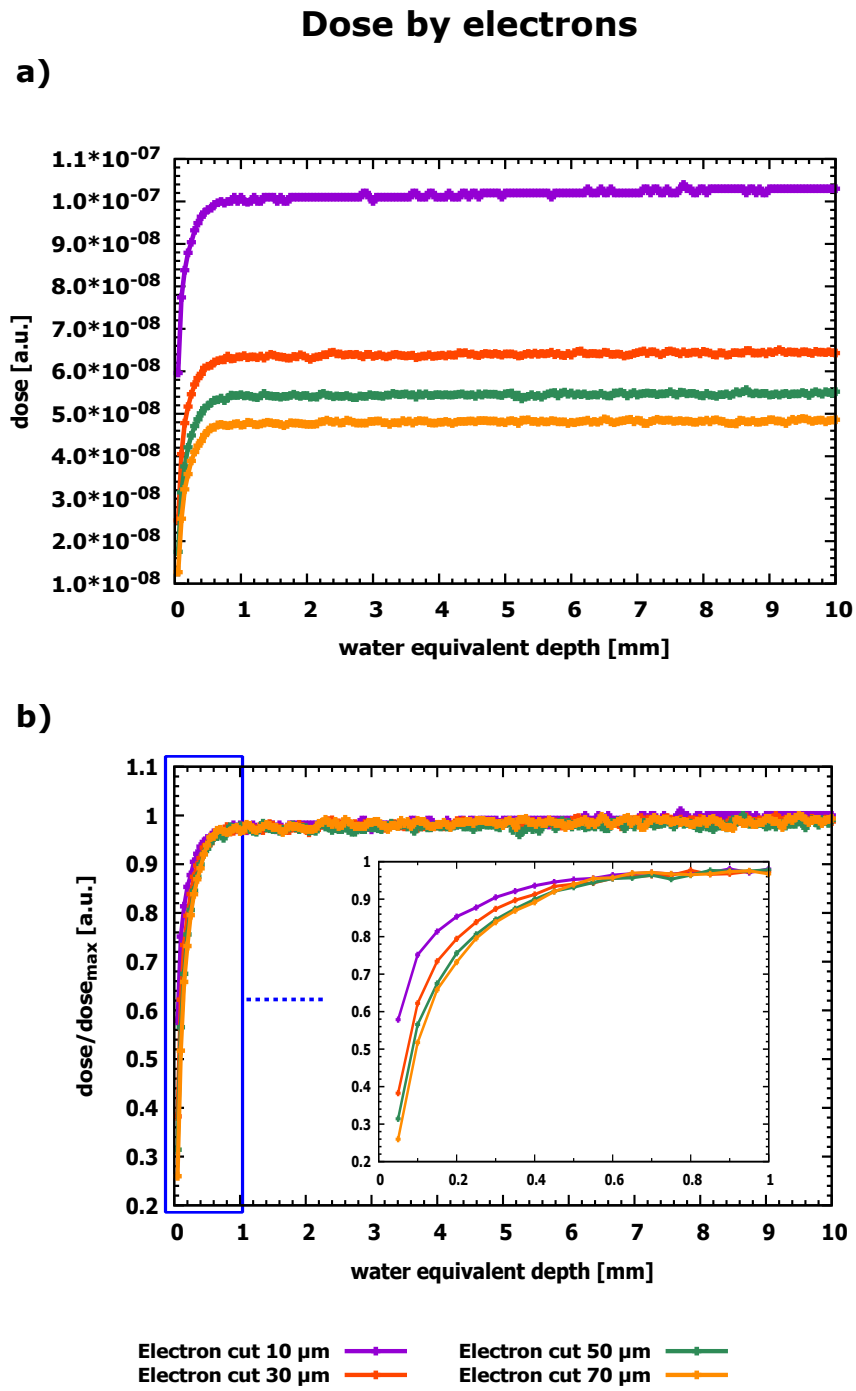


**Figure 4.14:** Various TOPAS range cut settings resulting on electron dose deposition in the first ten millimeters. a) Range cut of 10 $\mu$m, 30 $\mu$m, 50 $\mu$m (default) and 70 $\mu$m. The lower the range cut, the more dose is deposited by electrons. b) The dose values were normalized to its maximum. The plateau region looks very similar, but a closer look into the first millimeter reveals again a gradation of dose deposition due to range cut changes.

## 4.6 Determination Of The Backscatter Effect For The Extrapolation Ionization Chamber

Measurements for quality assurance are performed in water or solid water (e.g. RW3), in which the measuring chamber is embedded in the medium. Since the extrapolation IC cannot be enclosed in RW3 plates like for example the IBA PPC05, TOPAS was used to determine the effect of backscatter. For this purpose, the extrapolation IC had to be modeled in TOPAS. The dimensions of the chamber were measured and obtained from Ref [106]. The materials could not be determined clearly. In this work, an estimate was made for the housing, the hard plastic and the tissue equivalent plastic to aluminum, PVC and Shonka A150 [172]. The assignment of the materials and a cross-section of the modeled extrapolation IC can be seen below.

| Number | Material | Color |
|---|---|---|
| 1 | Air | White |
| 2 | Air gap | Red |
| 3 | Aluminum | Grey |
| 4 | Kapton® | Brown |
| 5 | Shonka A150 | Orange |
| 6 | PVC | Blue |

**Table 4.15:** Assigned materials for the TOPAS extrapolation IC.

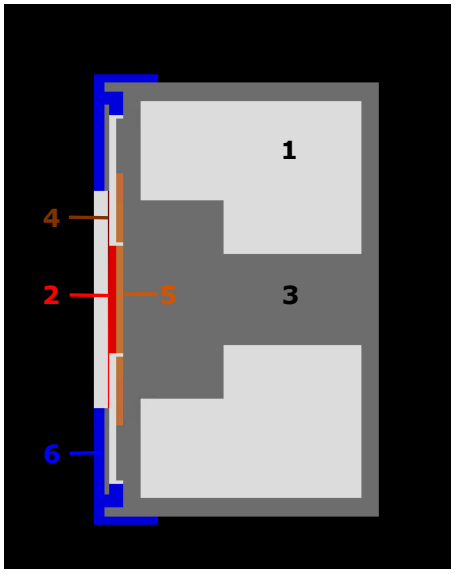


**Figure 4.15:** Cross section of a modeled extrapolation IC in TOPAS. The colors coding is listed in the table next to this figure.

The TOPAS extrapolation IC was designed without the rear part of the micrometer fine adjustment. The chamber with its measuring area (air gap between the electrodes, entrance window of 50 $\mu$m) was positioned in the isocenter in the simulation. The setup consisted of a scanned 10 cm x 10 cm 150.0 MeV proton field and the extrapolation IC was surrounded by air and then by water (in a 20 cm x 20 cm x 20 cm water tank). The scoring area was the measurement area of the chamber, which is 2 mm in width according

to Section 4.3. Further, various RW3 build-ups (1 mm, 1 cm and 3 cm) were placed in front of the chamber to get some more data for the backscatter comparison. As a result, the uncertainty for the effect of the backscatter for the extrapolation IC can be calculated with TOPAS to

$$U_{b,Dose} = 0.1\,\% \qquad . \tag{4.14}$$

# Chapter 5

# Determination Of Surface And Skin Dose Of Pristine Bragg Peaks

In this section, the surface and skin dose in proton therapy is investigated in more detail. The study of the depth dose curve is performed with various detectors, which have already been introduced in Chapter 3.1. A comparison with TOPAS Monte Carlo (Chapter 3.2) is also provided. This chapter contains the content of the first publication on this topic called *Determination of surface dose in pencil beam scanning proton therapy* [16].

## 5.1 Experimental Setup

Depending on the detector type, the setup was executed on the table at a gantry angle of 0° or 90°. At 0°, IBA PPC05, the TLDs, the EBT3 and HD-V2 films as well as the combination of EBT3 film with PMMA wedge were irradiated. Using the PPC05 RW3 adapter plate and the possibility of milling a RW3 plate with four holes for the TLDs, both detectors could be embedded. Whereas the two films were pressed onto the surface of the RW3 plate and fixed at each edge with adhesive tape.
Alignment at isocenter was performed with the laser system and for the ionization chambers additionally with the X-ray system. For each setup with the RW3 phantom, a total of 5 cm (5x1 cm plate) was used as backscatter. Figure 5.1 a)-d) show examples of the various measurement setups at the gantry angle of 0°.
Due to the design, the extrapolation IC was positioned at a gantry angle of 90° (Figure 5.1 e)). The chamber was fixed in place with adhesive tape on five RW3 plates which were aligned flush with the chamber. This allows the build-up material to be fixed flush to the existing plates without changing the position of the chamber. No backscatter was used behind the chamber (see backscatter investigation in Subsection 4.6).

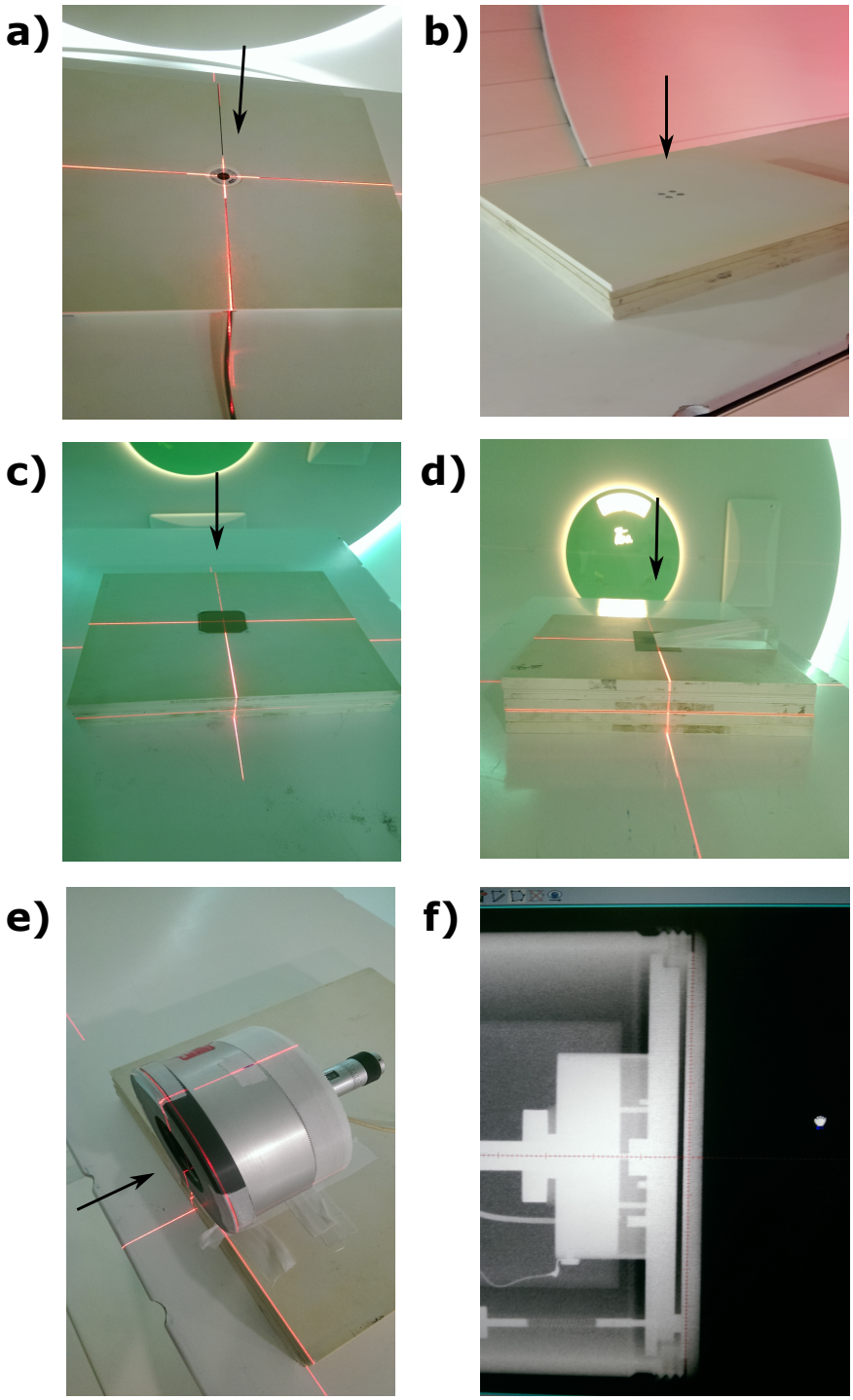


**Figure 5.1:** Setup of various used detectors for the determination of surface and skin dose. The direction of irradiation is marked with an arrow. a) Embedded IBA PPC05 in RW3. b) Four drilled holes for TLDs embedded in RW3 (taken from [124]). c) Alignment of Gafchromic™ EBT3 film array. d) Placement of PMMA wedge on Gafchromic™ EBT3 film. e) Setup of the PTW extrapolation IC type 23391 f) X-ray image of the PTW extrapolation IC type 23391 alignment.

The principle for the measurement series was to place different thicknesses and materials as build-up in front of the aligned detectors. This allowed the recording of different sampling points in the depth dose curve. Table 5.1 lists the materials and thicknesses of the build-up for the individual detectors.

| Detector | Build-up material | Build-up material - physical thickness [mm] | Build-up material - WED [mm] |
|---|---|---|---|
| PPC05 | RW3 | 0.5, 1, 2 | 0.52, 1.03, 2.06 |
| Extrapolation IC | RW3 | 0.5, 1, 2 | 0.52, 1.03, 2.06 |
| EBT3 film | EBT3 | 0.28 | 0.36 |
| HD-V2 film | - | - | - |
| Film & Wedge | PMMA | 0.28-4.17 | 0.32-4.80 |
| TLD | Mylar, RW3 | 0.005, 1, 2 | 0.006, 1.03, 2.06 |

**Table 5.1:** This table shows the build-up material and the corresponding physical thickness of that material for measurements in the surface region. The right column presents the converted WED.

Parts of the RW3 slab phantom are used for the two ICs. It consists of 1 cm (29x pieces), 5 mm (1x piece), 2 mm (2x pieces) and 1 mm (1x piece) plates. Further, there was an additional thin RW3 plate with a physical thickness of 0.5 mm available at WPE. Then, the individual and also the different plate combinations from Table 5.1 were placed on the embedded PPC05 chamber. For the extrapolation IC, the RW3 plates were positioned in front of the entrance window and fixed to the plates on the couch. Regarding the Gafchromic™ films, the approach of stacking radiochromic films according to Butson et al. [177] was followed. For the EBT3 films, 10 films were stacked on top of each other and fixed at the corners with adhesive tape. This resulted in sampling in water equivalent depth between 0.18 mm (center of the active layer) and 3.40 mm in steps of 0.36 mm. Due to the film structure and the limitation of the HD-V2 films, no stacking or further build-up material was used. The films were also fixed at the corners with adhesive tape. The PMMA wedge is a continuous build-up due to its design. The thickness of the wedge is taken from the preliminary investigation from Subsection 4.2.5 and is between 0.28 mm and 4.17 mm for this series of measurements (Table 5.1). Similar to the film stacks, two different Mylar stacks were used as build-up for the TLDs. On the one hand 5 Mylar films with a total physical thickness of 23 $\mu$m and on the other hand 10 films with a total thickness of 46 $\mu$m (the value for the physical thickness of the Mylar film is rounded to 0.005 in Table 5.1). Some more data sampling were measured for 150.0 MeV during the Master Thesis [124].
For all detectors, a measurement point is recorded at the reference depth in 3 cm WED. This depth is also used in quality assurance to determine the reference dose at WPE

[178]. The measurements were carried out depending on the entrance window of the various detectors and resulted to 2.8 cm or 2.9 cm RW3 build-up material.
Table 5.2 shows the entrance window or the measuring depth of the various detectors converted into a WED. The data were calculated according Equation 4.5 and the $WET$ factors were taken from Chapter 4.1. This listed $WED$ value represents the detectors output without a physical build-up and therefore the first measurement depth of the each detector in the depth dose curve.

| Detector | Entrance window/measuring depth [$\mu$m] | $WED$ [$\mu$m] |
|---|---|---|
| PPC05 | 1000 | 1560 |
| Extrapolation IC | 25, 50, 75 | 32.5, 65.0, 97.5 |
| EBT3 | 140 | 179.2 |
| HD-V2 | 6 | 7.7 |

**Table 5.2:** Entrance window or measuring depth of the various detectors converted into a $WED$.

Due to the relatively thick entrance window, the PPC05 chamber is not sensitive in the depths of smaller than 1.5 mm (1.56 $WED$). The three entrance windows of the extrapolation IC provide three scans <100 $\mu$m. The two radiochromic films are classified according to the center of their active layer (see Figure 3.7). The TLD is not listed here, as the measuring point was defined in Subsection 4.4. Due to its design and function, the measuring depth of 43 $\mu$m serves here as $WED$.
The spot pattern was a field with the dimension of 10.25 x 10.25 cm$^2$ and a spot spacing of 2.5 mm, which is similar to the QA field at WPE. The detectors were irradiated ten times without a physical build-up, with the previously introduced build-up material steps of this section and at the reference depth of 3 cm for each of the three energies [179]: 100.0 MeV ($\sigma_E$=0.65 MeV), 150.0 MeV ($\sigma_E$=0.82 MeV) and 226.7 MeV ($\sigma_E$=0.78 MeV). $\sigma_E$ is the energy width, which defines the width of the Bragg peak. Due to the small number of HD-V2 films and the preliminary work consisting of testing and calibration, only two instead of ten measurements were possible.

## 5.2 Monte Carlo Setup

The Monte Carlo setup was designed to mimic the experimental setup and to score dose to water in a water phantom for shallow depths. The WPE nozzle model from Subsection 3.11 is the basis. Then, the pencil beam scanning technique was translated to TOPAS. There, it is implemented as time based simulation, where each individual spot

is characterized with time, magnetic field strength and the number of protons to obtain a spot pattern of 10.25 cm x 10.25 cm and $1 \cdot 10^9$ starting total proton particles (results to a dose uncertainty $\leq 0.7\%$). Similar to the experimental approach, the same three energies were selected: 100.0 MeV ($\sigma_E$=0.64 MeV), 150.0 MeV ($\sigma_E$=0.82 MeV) and 226.7 MeV ($\sigma_E$=0.78 MeV). Due to the nozzle $WET$, the starting energies of a proton from the beginning of the simulation at the vacuum chamber have slightly higher energies. Further, the *CurForElectron* value was set to 1 $\mu$m (compare Subsection 4.5).
They were two different setups for depth dose scoring in a 10 x 10 x 10 $cm^3$ water tank with the following properties:

- Depth dose curve scoring in the first 5 mm $WED$ realized with a 5 x 5 x 5 $mm^3$ scoring volume and a z-binning (in depth) of 50 $\mu$m.
- Depth dose curve scoring in the first 200 $\mu$m with twenty 5 x 5 x 0.001 $mm^3$ volumes placed in 10 $\mu$m steps.
- The water tank was placed depending on the two scoring lengths of 5 mm and 200 $\mu$m by this length in front of the isocenter, which is similar to the film measurements.
- For the normalization depth of 3 cm, the water tank was placed at -3 cm to obtain the isocenter at 3 cm. Here, the scoring volumes had the same sizes like the volumes from point one (5 mm) and two (1 $\mu$m).
- Due to a binning of 50 $\mu$m the dose results will be presented at the center of the scoring volume (25 $\mu$m). Therefore an uncertainty in depth can be defined as $\pm$25 $\mu$m. For the second length of 1 $\mu$m, the depth uncertainty was not considered because of the short length, which is not visible in the later presented plots.

## 5.3 Uncertainty Analysis

The general uncertainty analysis is based on type A and type B uncertainties after Gum (Guide to the Expression of Uncertainty in Measurement [180]). Therefore, the labels are called $U_a$ and $U_b$, respectively. $U_a$ is the statistical uncertainty representing the standard error of the mean (SEM, 1-sigma statistical uncertainty). The systematic uncertainty $U_b$ is dependent on the detector type, but can be further distinguished between dose related $U_{b,Dose}$ or depth related $U_{b,Depth}$ uncertainty. If possible, $U_a$ and $U_b$ were calculated to $U_c$, the uncertainty in quadrature. Further, since every measurement and simulation was normalized to the reference depth (3 cm), most uncertainties are excepted to cancel out. This results in only individual detector uncertainties. As an example, the Gafchromic™ films are showing slightly variations due to the manufacturing process.
For this section, Table 5.3 is describing the obtained uncertainties of all used detectors

and TOPAS. The values are the maximum occurring uncertainties for each described uncertainty type of all measurements and energies. As a result $U_{c,Dose}$ may not be consistent to $U_a$ and $U_b$. Most of the listed systematic uncertainties were described in a former section like in Chapter 4, except of the gradient uncertainty for the extrapolation IC at 100.0 MeV, compare Table 5.3. The $U_{b,Dose}$ uncertainty of 0.4% was calculated using a 100.0 MeV depth dose curve and taking into account, that the depth of 3 cm is not perfectly reached by using RW3 plates. This has an impact due to the fact, that the reference point of 3 cm lies at the gradient in the direction to the Bragg peak for 100.0 MeV. Due to the larger air gap of 2 mm between the electrodes of the PTW extrapolation IC, the uncertainty $U_{b,Dose}$ of 0.4% was only applied for this chamber. For all experimental methods, a common depth uncertainty $U_{b,Depth}$ of 1.6% was set for all used detectors resulting from the $WET$ calculation study from Subsection 4.1. Both IC's have a minor $U_a$ or $U_{c,Dose}$ uncertainty, whereas the dose uncertainties for the Gafchromic™ films and TLDs are the highest ones (up to 2.9%).

| Measuring detector | $U_a$ | $U_{b,Dose}$ | $U_{b,Depth}$ | Note to $U_b$ | $U_{c,Dose}$ |
|---|---|---|---|---|---|
| PPC05 | 0.2% | - | - | - | - |
| Extrapolation IC | 0.2% | 0.1% (0.4%) | - | Effect of backscatter; (Gradient uncertainty only for 100.0 MeV) | 0.2% (0.4%) |
| EBT3 film | 0.3% | 1.0% | 15 $\mu$m | Dose uncertainty; Active layer | 1.1% |
| EBT3 film & wedge | 0.3% | 1.4% | 45 $\mu$m | Dose uncertainty; Active layer and wedge | 1.4% |
| HD-V2 film | 1.1% | 2.8% | 6 $\mu$m | Dose uncertainty; Active layer | 2.8% |
| TLD | 2.9% | - | 3 $\mu$m | Effective point of measurement | - |
| TOPAS | 0.7% | - | 25 $\mu$m | Binning size | - |
| All experimental methods | - | - | 1.6% | $WED$ factor uncertainty | - |

**Table 5.3:** Uncertainty budget for the depth dose curve measurements. The uncertainties are divided into the statistical uncertainty $U_a$ (SEM, 1-sigma statistical uncertainty) and into $U_b$ as systematic uncertainty. Moreover, a further categorization was applied for $U_b$: dose uncertainty $U_{b;Dose}$ and depth uncertainty $U_{b;Depth}$. $U_{c;Dose}$ is the dose uncertainty in quadrature. Each value presented here is the maximum uncertainty of all measurements and simulations for all energies (100.0 MeV, 150.0 MeV, 226.7 MeV).

## 5.4 Results

### 5.4.1 Determination Of The Measured And Simulated Surface And Skin Dose

The results for the measured and simulated surface and skin doses were plotted separately for each energy (see Figures 5.2, 5.3, 5.4). The Figures are presenting two different scales, first surfaces dose measurements of proton depth dose curves from zero to five millimeter $WED$ and second, a zoomed in graphical presentation of the first 200 $\mu$m $WED$, which includes the skin dose depth $D_{0.07}$ at 70 $\mu$m. Further, the three plots visualize the various detectors measurement ranges for surface depth dose curve sampling.
The first Figure 5.2 depicts the 100.0 MeV depth dose curve. In comparison to the higher energies 150.0 MeV (Figure 5.3) and 226.7 MeV (Figure 5.4) the normalized percentage dose range is approx. 10% lower. As already shown in Figure 2.3 of the theory chapter, the normalization depth of 3 cm is steeper for lower energies than for higher energies resulting in a higher normalization dose due to the rise towards the Bragg Peak.
The continuous sampling from TOPAS and the PMMA wedge in combination with the EBT3 film as well as the extrapolation IC exhibit a similar depth dose profile. The results obtained from the EBT3 film, the HD-V2 film as well as the TLDs and the IBA PPC05 chamber are above and below the depth dose curves of the experimental reference and the MC [16]. Considering an average contribution of all detector curves, the rise of surface dose in the first 5 mm amounts to approx. 3%.
In the zoomed in graph in the range up to 200 $\mu$m, measurements are included only from HD-V2 film, EBT3 film, TLD, the extrapolation IC and TOPAS simulation. In general, all measurement and simulation results are within the uncertainties. Comparing the experimental reference values of the extrapolation IC, which are representing the three entrance windows (32.5 $\mu$m, 65 $\mu$m, 97.5 $\mu$m $WET$) with nearby MC simulations (30 $\mu$m, 70 $\mu$m and 100 $\mu$m $WET$) the percentage difference are 0.4%, 0.6 % and 0.7%. As TOPAS has a full sample over the full range of 200 $\mu$m, the increase of dose over this range was determined by MC. For 100.0 MeV, there was an increase of 1.4% between 10 $\mu$m an 200 $\mu$m.
The measured and simulated depth dose curves for 150.0 MeV are displayed at Figure 5.3. In the $WED$ range between 0-5 mm, there are two small shifted trends of depth dose curves: TOPAS MC, the EBT3 film stack and the HD-V2 film on the hand, and the PPC05 IC, the extrapolation IC, the TLDs and the EBT3 film with the PMMA wedge on the other hand. Again, a consideration over all detector types yields to a percentage dose increase of approx. 3.8%.

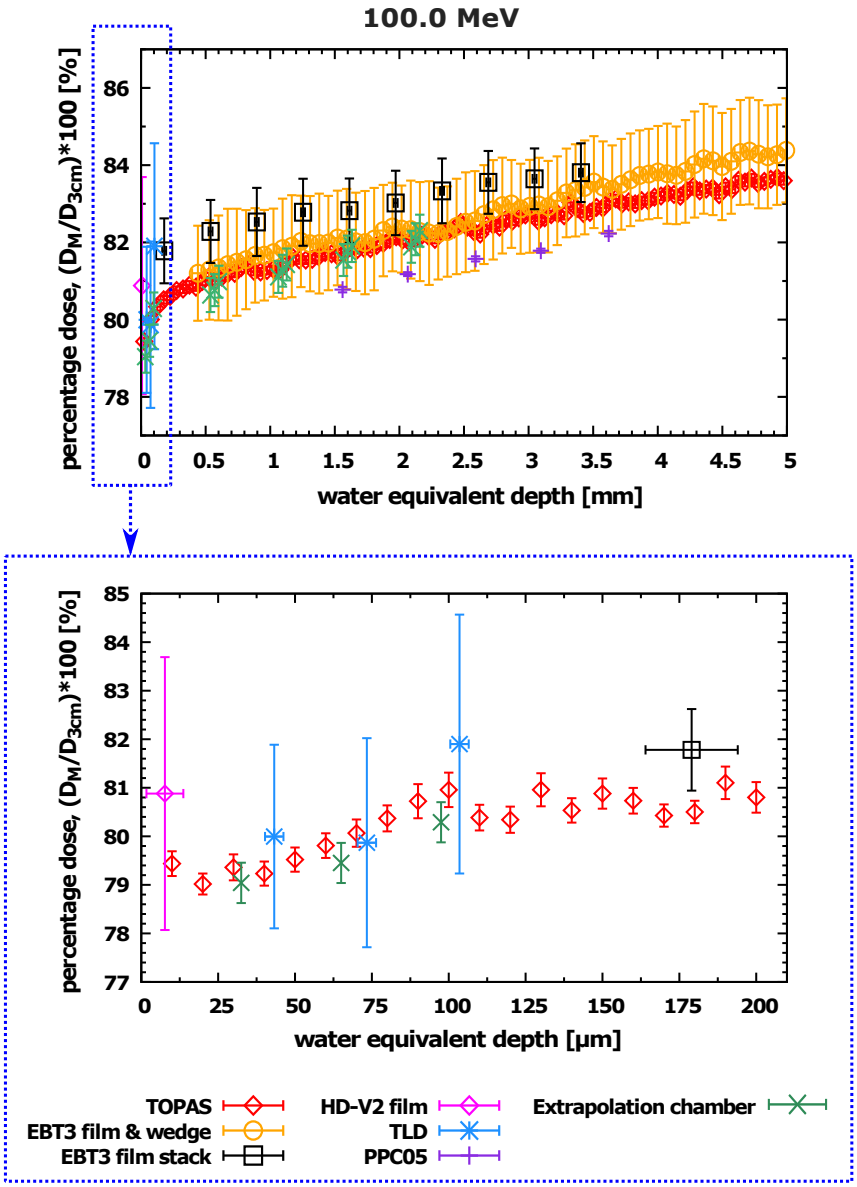


**Figure 5.2:** Measurement and simulation results for a scanned 100.0 MeV proton beam. The plot depicts the first five millimeter $WED$ of the proton depth dose curve. The lower plot shows the zoomed region in the $WED$ range between 0-200 $\mu$m. Each result of the IBA PPC05, PTW extrapolation IC, the EBT3 & HD-V2 Gafchromic™ films, TLDs and TOPAS was normalized to the reference depth of 3 cm. Reproduction according Ref. [16].

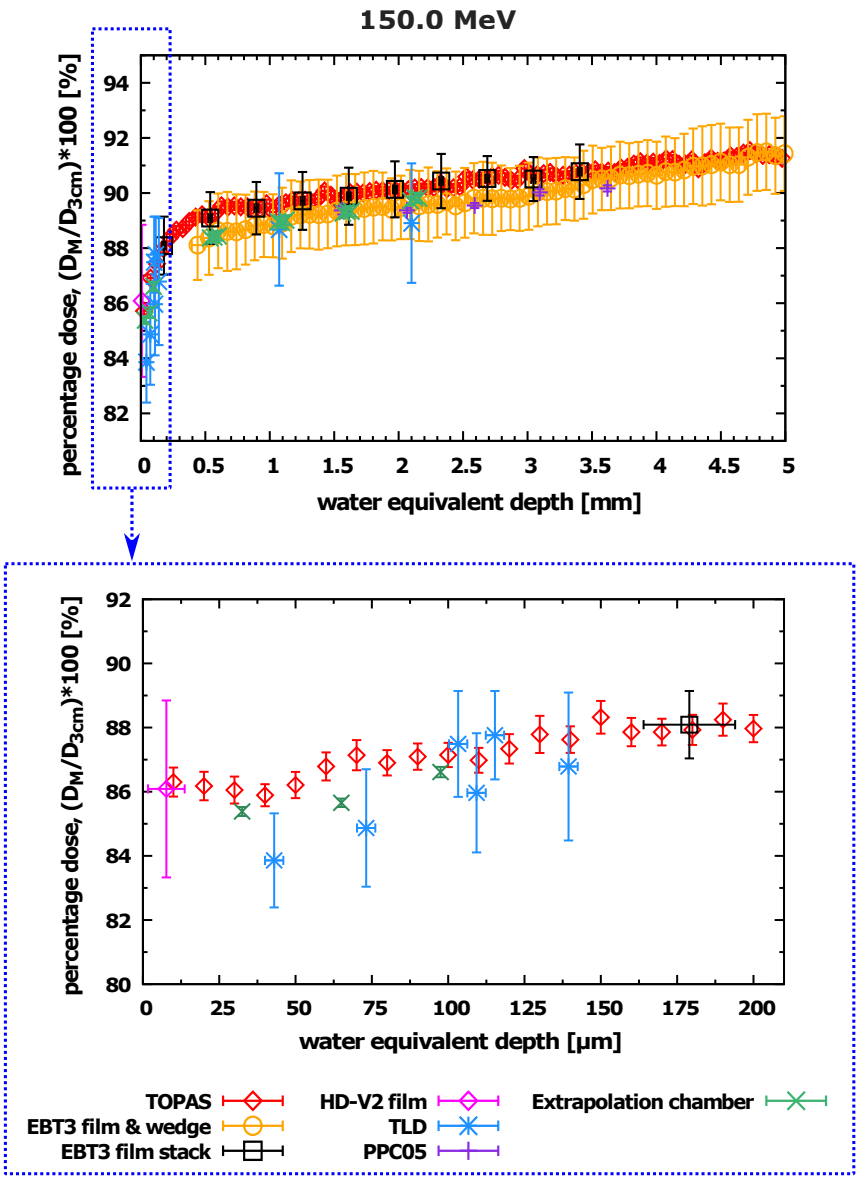


**Figure 5.3:** Measurement and simulation results for a scanned 150.0 MeV proton beam. The plot depicts the first five millimeter $WED$ of the proton depth dose curve. The lower plot shows the zoomed region in the $WED$ range between 0-200 $\mu$m. Each result of the IBA PPC05, PTW extrapolation IC, the EBT3 & HD-V2 Gafchromic™ films, TLDs and TOPAS was normalized to the reference depth of 3 cm. Reproduction according Ref. [16].

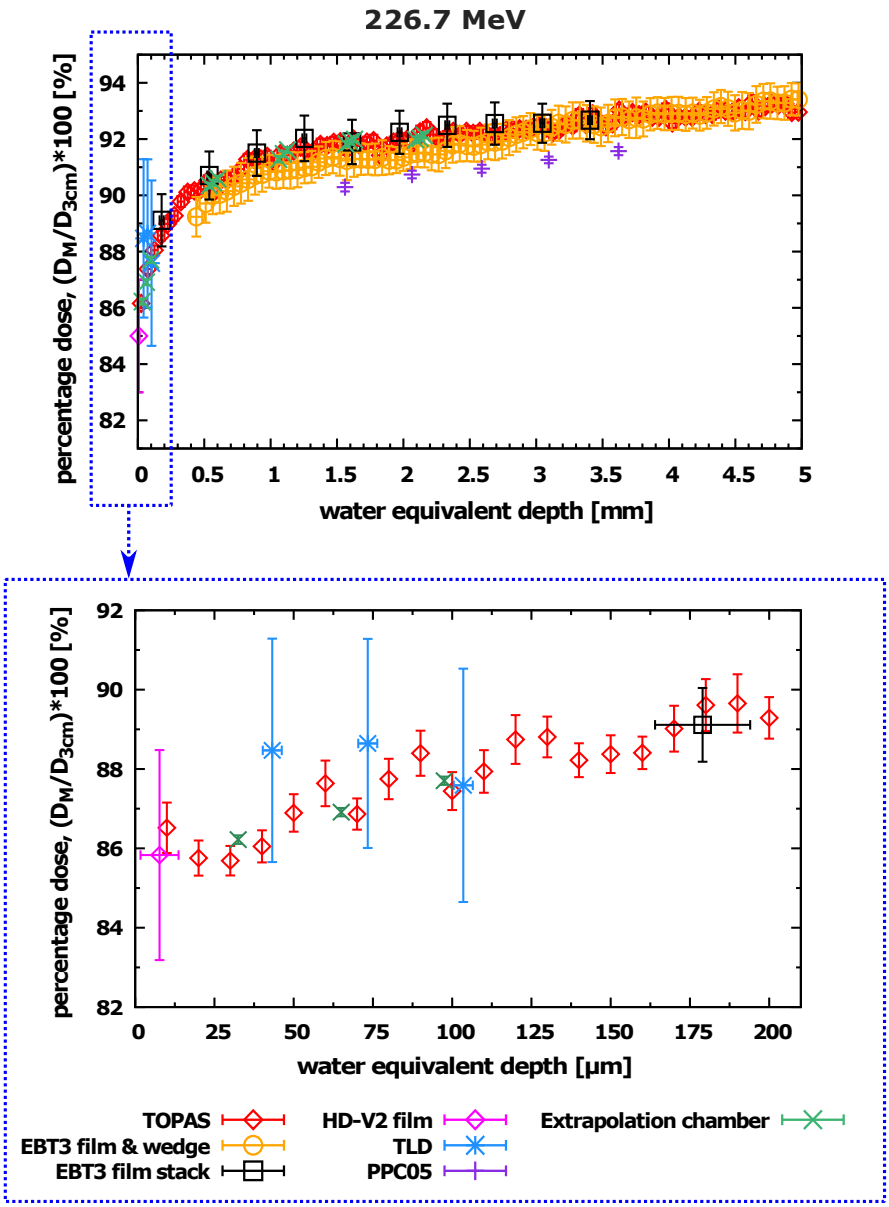


**Figure 5.4:** Measurement and simulation results for a scanned 226.7 MeV proton beam. The plot depicts the first five millimeter $WED$ of the proton depth dose curve. The lower plot shows the zoomed region in the $WED$ range between 0-200 $\mu$m. Each result of the IBA PPC05, PTW extrapolation IC, the EBT3 & HD-V2 Gafchromic™ films, TLDs and TOPAS was normalized to the reference depth of 3 cm. Reproduction according Ref. [16].

Regarding the surface dose until 200 $\mu$m $WED$, all detectors are in agreement within the uncertainties. Especially the EBT3 and HD-V2 film closely match the TOPAS depth dose curve. Further, the TLD and the extrapolation IC measurements agree within their uncertainties, but are showing an approx. dose difference of 2.0% (TLD 43 $\mu$m $WED$) and 1.4% (extrapolation IC 65 $\mu$m $WED$) to the TOPAS depth dose curve (40 $\mu$m and 70 $\mu$m). The overall percentage dose increase in the range between 0-200 $\mu$m was derived from TOPAS and amounted to 1.7% (see Figure 5.3).
A strong agreement of depth dose curves is presented in Figure 5.4. In detail, these are the depth dose curves of TOPAS, the EBT3 film stack, HD-V2 film and the extrapolation IC. Regarding the EBT3 film with the PMMA wedge depth dose curve, there is first a percentage dose difference of approx. 1% at the beginning of the sampling to TOPAS, but it reaches the same dose level as TOPAS at around 3 mm $WED$. The depth dose curve of the PPC05 IC is lower with a maximum of 1.5% deviation from TOPAS. The averaged percentage increase of all detector in the first 5 mm is approx. 4.8%.
The close match of the measurements and the simulations of the 5 mm scale is also well reflected in the zoomed graphic of Figure 5.4. A small percentage difference of <0.1% was observed if the 65 $\mu$m entrance window of the extrapolation IC was compared against the TOPAS scoring at 70$\mu$m. The biggest offset of 2.5% was noted for TLD (43 $\mu$m) against TOPAS (40 $\mu$m). For the TOPAS results obtained with 226.7 MeV protons, the curve rose 2.8% from the first to the last scoring volume.
A statement about the skin dose at 70 $\mu$m ($D_{0.07}$) was derived based on the collected data presented in the Figures 5.2, 5.3 and 5.4. Table 5.4 summarizes $D_{0.07}$ reported from the TOPAS scoring volume at 70 $\mu$m $WED$ and from the extrapolation IC by interpolating the dose points of the three entrance windows (32.5 $\mu$m, 65 $\mu$m and 97.5 $\mu$m). The TOPAS results for $D_{0.07}$ were 80.1 $\pm$ 0.2% for a 100.0 MeV field, 87.1 $\pm$ 0.5% for 150.0 MeV and 86.9 $\pm$ 0.4% for the remaining energy 226.7 MeV. Further, the calculated normalized skin doses at 3 cm depth for the extrapolation IC were 79.7 $\pm$ 0.3% for 100.0 MeV, 86.0 $\pm$ 0.6% for 150.0 MeV and 87.1 $\pm$ 0.1% for 226.7 MeV of the 100% dose measured at 3 cm depth. The $D_{0.07}$ results are matching within their uncertainties for all three energies. The uncertainties described in Table 5.4 are the statistical uncertainty $U_a$ for TOPAS and fitting uncertainties for the extrapolation IC.
In addition to the normalization depth to 3 cm, which is used in this work, data were also presented for proton centers which are using 2 cm as normalization depth.

| | Skin dose ($D_{0.07}$) normalized at 3 cm [%] | | Skin dose ($D_{0.07}$) normalized at 2 cm [%] | |
|---|---|---|---|---|
| Energy [MeV] | TOPAS | Extrapolation IC | TOPAS | Extrapolation IC |
| 100.0 | 80.1 ± 0.2 | 79.7 ± 0.3 | 86.4 ± 0.3 | 86.5 ± 0.3 |
| 150.0 | 87.1 ± 0.5 | 86.0 ± 0.6 | 89.0 ± 0.5 | 88.0 ± 0.6 |
| 226.7 | 86.9 ± 0.4 | 87.1 ± 0.1 | 87.7 ± 0.6 | 87.0 ± 0.1 |

**Table 5.4:** Skin dose $D_{0.07}$ for TOPAS and the extrapolation IC. The percentage results were normalized to the reference depth of 3 cm and 2 cm $WED$ for each energy under investigation.

### 5.4.2 Build-up Effect Dependent On Proton Kinetic Energy

The Figures 5.2, 5.3 and 5.4 show a build-up effect of the proton depth dose curve for all three energies. This effect was further investigated and is presented in this subsection by using TOPAS.

The shape of the build-up effect of the above mentioned Figures is similar to the contribution of the electron depth dose curve which was shown several times in Section 4.5. Therefore, TOPAS was used again to score electron doses in the first 1.3 mm $WED$ in the same setup as used in this Chapter 5. To obtain a higher resolution, the binning for the electron scoring was changed to 10 $\mu$m. The results of the electron depth dose curves for all three energies were overlaid with the already presented 5 mm depth dose curves Section 5.4.1. The corresponding graphs are displayed in Figure 5.5. With both depth dose curves, the end and thus the range of the build-up effect was defined qualitatively in the dose plateau region. For 100.0 MeV, the end of the build-up effect is at approx. 375 ± 25 $\mu$m, see Figure 5.5 a). For higher energies the build-up effect had a greater range, for 150.0 MeV it was approx. 725 ± 25 $\mu$m (Figure 5.5 b) and approx. 1075 ± 25 $\mu$m for 226.7 MeV (Figure 5.5 c). The trend of both depth dose curves after the solid line of each energy is linear. Similar to Pfuhl et al., both depth dose curves were normalized to the depth of the end of the build-up effect [31]. The magnitude of the build-up effect was calculated by the difference of the first TOPAS-all particle scoring point to the normalization point (end of build-up, solid line). With increasing proton energy, the magnitude of the build-up effect increased. In detail the percentage dose rose for 100.0 MeV, 150.0 MeV and 226.7 MeV in the following: 1.8%, 4.3%, 5.8%.

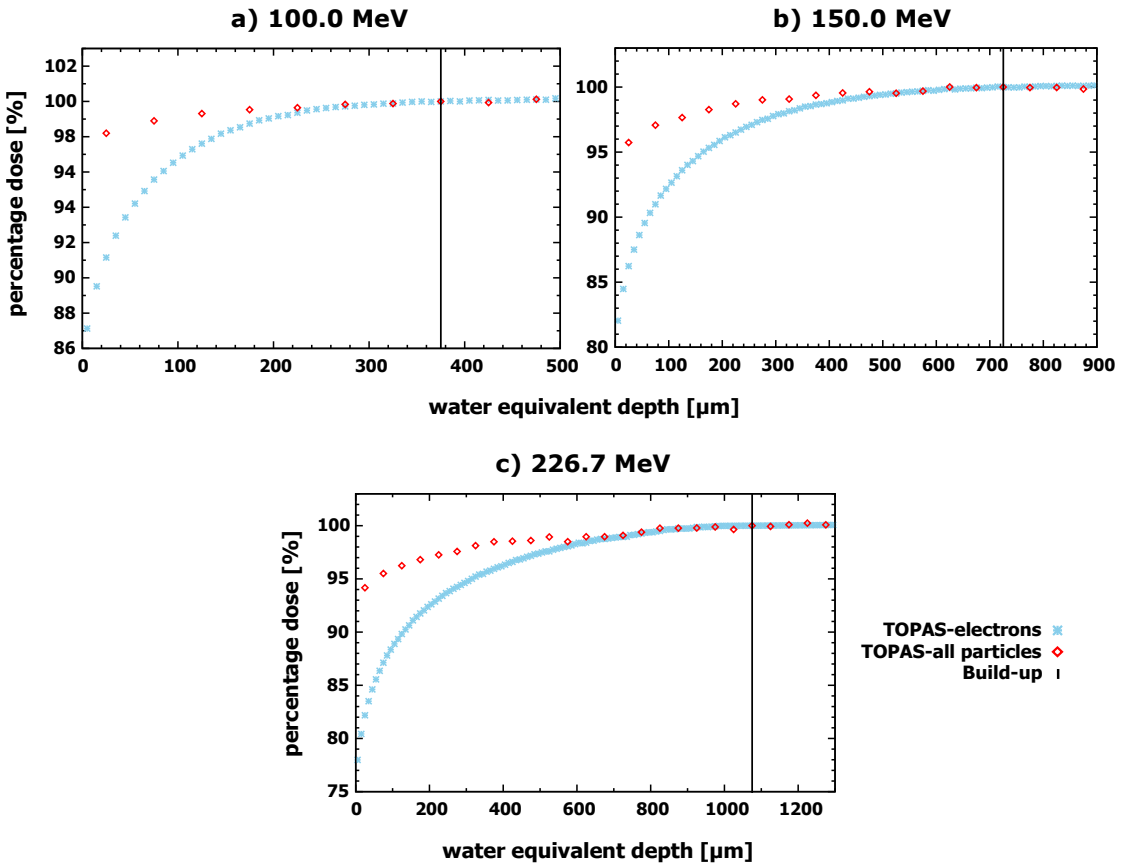


**Figure 5.5:** Overlay of proton depth dose curve contribution: Electrons and all particles. The line marker was approx. set to the depth, where both curves are on the flat plateau region. Taking the proton depth dose curves with all particles (TOPAS-all particles) for a statement, the build-up length results to approx. 375 ± 25 $\mu$m for a) 100.0 MeV, approx. 725 ± 25 $\mu$m for b) 150.0 MeV and approx. 1075 ± 25 $\mu$m for c) 226.7 MeV. Further, the magnitudes of these build-up effects were analyzed referring to the first scoring volume to the solid line and were approx. 1.8 %, 4.3 % and 5.8 %. Note: No uncertainties were added in this graph due to a qualitative graphical comparison of the depth dose curves.

Further, to get an overall classification in the context of all used detectors, the end of the build-up was marked with the solid line in the three depth dose curves of the 5 mm scale (Figure 5.6).

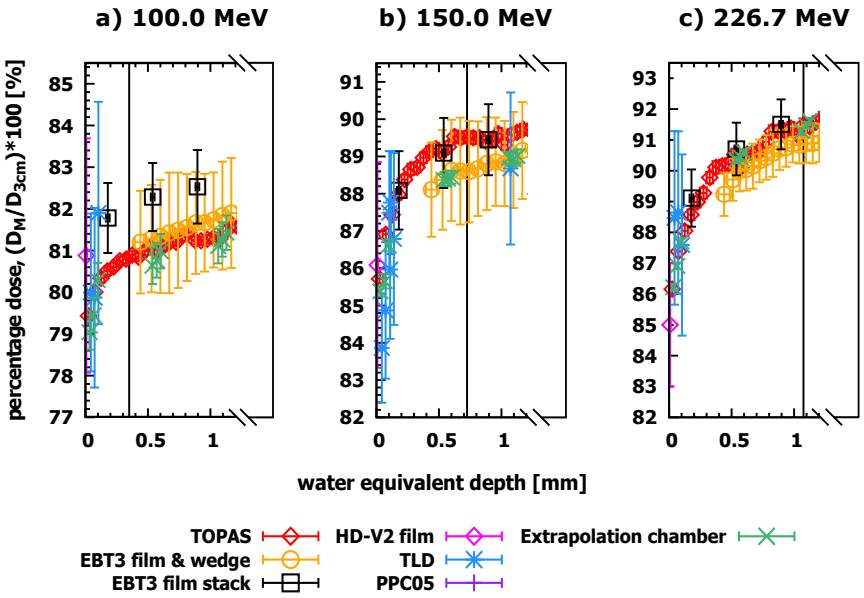


**Figure 5.6:** Visualization of the build-up range (line marker) on the measured depth dose curves. a) 100.0 MeV: The build-up was approx. 375 ± 25 $\mu$m. b) 150.0 MeV: The range for the build-up was approx. 725 ± 25 $\mu$m. c) 226.7 MeV: The build-up resulted to approx. 1075 ± 25 $\mu$m. Reproduction according Ref. [16].

# Chapter 6

# Impact Of Air Gap, Range Shifter, And Delivery Technique On Skin Dose In Proton Beam Therapy

Chapter 5 introduced the skin dose $D_{0.07}$ at 70 $\mu$m water equivalent depth. The aim of this chapter is to improve the empirical knowledge of the absorbed dose at skin depth in proton therapy. As the extrapolation IC and TOPAS MC were suitable for this purpose, both methods were used to investigate the effect of the air gap, the range shifter or proton delivery technique. The air gap is the distance between nozzle exit or RS to the measurement point. This chapter contains the content of the second publication to this topic called *Impact of air gap, range shifter, and delivery technique on skin dose in proton therapy* [17].

## 6.1 Experimental Setup

The WPE gantry room 2 uses a dedicated nozzle for PBS delivery. For these measurements, the PBS room was changed from GTR4 to GTR2, because a longer air gap distance was achieved between isocenter and Kevlar® exit window (47.4 cm to 51.1 cm) due to the movable snout construction. The second room (gantry room 3) is equipped with a universal nozzle, which can deliver all three techniques PBS, US and DS. In the period, when the measurements were performed, only US and DS could be delivered in room 3. Both nozzle designs and delivery techniques were described in Subsection 2.3.3 beam delivery techniques.
The basic idea behind the measurements when considering the air gap, the range shifter and the two nozzle designs with their delivery techniques is sketched in Figure 6.1. Figure 6.1 a) shows the IBA dedicated PBS nozzle. The total air gap between the exit window and isocenter was 51.1 cm. This full range was used for monoenergetic measurements

without the RS marked with '**x**'. Detailed air gap values are listed in Table 6.1. The measurement point in front of the exit window with an air gap of 6.2 cm was also the experimental lower air gap limit due to potential collision between setup and mechanical parts of the nozzle. Similar to Chapter 5, the same three quasi-monoenergetic energies of 100.0 MeV, 150.0 MeV and 226.7 MeV (field size 10.25 cm x 10.25 cm) with a spot spacing of 2.5 mm were used for PBS.

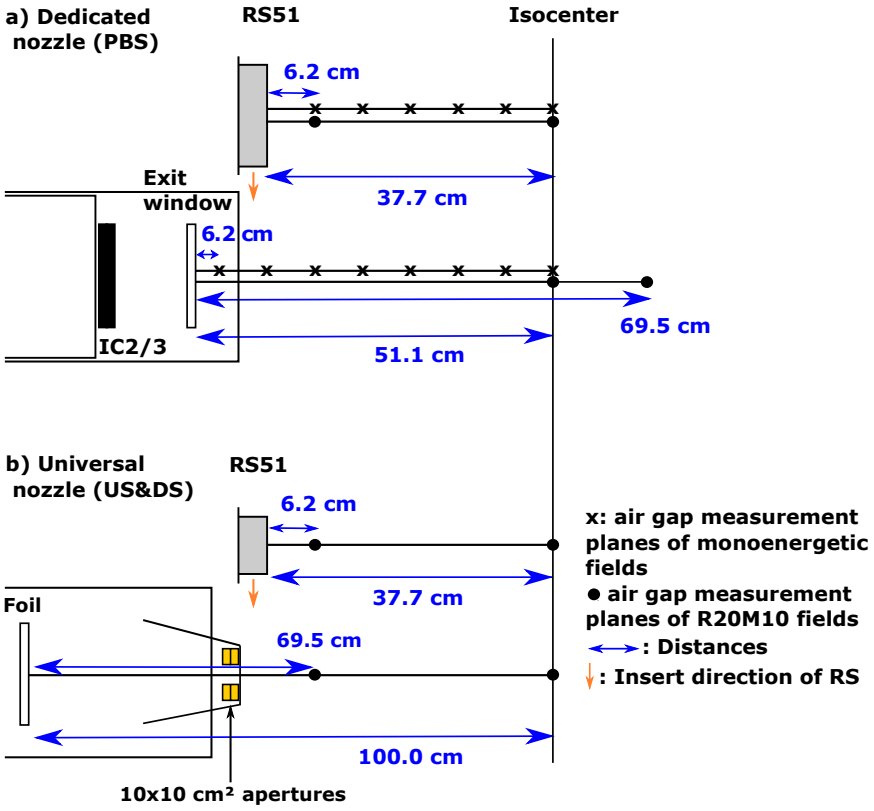


**Figure 6.1:** Overview of the experimental setups for the skin dose measurements with various air gaps for the pencil beam dedicated nozzle and the universal nozzle for US&DS. The blue arrows are showing the various relations of the distances in the two nozzle designs. The maximum air gap is defined as distance to the last foils of the nozzle designs. The symbols '**x**' and '●' are presenting the measurement positions of the extrapolation IC for monoenergetic and for R20M10 SOBP fields. In addition, measurements were done with and without the RS51. a) Pencil beam dedicated nozzle with eight monoenergetic and two SOBP air gap measurement planes. Taking the RS51 into account, six more monoenergetic and two more SOBP air gap measurements planes were performed for the pencil beam dedicated nozzle. b) Two air gap measurements were acquired without and with the RS51 for the universal nozzle with US & DS delivery technique. Reproduction according Ref. [17].

To compare the impact of the range shifter with a physical thickness of 4.4 cm (equivalent to 5.1 cm $WET$, further named as RS51) for a monoenergitic PBS field, six measurement planes were selected (compare air gap values in Table 6.1). The inserted RS51 reduced the total air gap between RS51 as last beam modifier and the isocenter to 37.7 cm. The corresponding fields were two more quasi-monoenergetic energies of 120.4 MeV ($\sigma_E$=0.67) and 150.3 MeV ($\sigma_E$=0.83). The application of the RS51 decreased the energy exactly from 150.3 MeV to 120.4 MeV to achieve a direct comparison and impact of the RS51. Furthermore, SOBPs were produced with all three proton delivery techniques. The two black lines marked with a '•' in each nozzle of Figure 6.1 a)+b) represents the measurement planes for the applied SOBP fields. The SOBP reference field had a range of 20.0 cm and a corresponding modulation width of 10.0 cm. In the following this combination of range R and modulation M is called R20M10. For the evaluation of the RS51 in combination with an SOBP, the fields have been adjusted accordingly to R25.1M10 [17]. A closer look between the PBS dedicated nozzle in 6.1 a) the and universal nozzle 6.1 b) reveals a different total air gap between last beam modifier and isocenter for the setup without RS. This air gap was 100 cm large (universal nozzle). In order to be able to compare both nozzle designs and thus the resulting total air gap to the isocenter, two distances were introduced: fixed ISO and fixed air gap. The first one refers to the measurement position at the ISO for both nozzles. The second one defines the fixed air gap of 69.5 cm with respect to the exit window of both nozzles (see Figure 6.1, [17]). Regarding the RS51, both nozzle air gaps were comparable (2x measurement planes each).
The snout position was 42.1 cm for every setup. In order to reach the predefined air gaps the patient positioning table was moved in the room x-axis with a gantry angle of 90°. An overview about the measurement conditions for the extrapolation IC were summarized in Table 6.1.

| | |
|---|---|
| Energy layering | Single quasi-monoenergetic layer |
| Kinetic energies $E$ of the fields [MeV] | 100.0, 120.4, 150.0, 150.3, 226.7 |
| Beam energy spreads $\sigma_E$ [MeV] | 0.65, 0.67, 0.82, 0.83, 0.78 |
| Spot pattern | 41 x 41 spots with 2.5 mm distance equal to 10.25 x 10.25 $cm^2$ |
| Spread-out Bragg peaks (SOBPs) | R20M10, R25.1M10 (R=Range, M=Modulation width) |
| Range shifter (RS) | Physical thickness D=4.4 cm, results to 5.1 cm water equivalent thickness |
| Apertures | centered square opening 10 x 10 $cm^2$ (2 x 3.3 cm thick, brass) |
| Air gaps without RS [cm] | Dedicated nozzle with PBS:<br>Monoenergetic layer (**x**): 51.1 (ISO), 44.5, 37.9, 31.3, 24.7, 18.6, 11.3, 6.2<br>Universal nozzle with US and DS:<br>SOBP(•): 100.0 (fixed ISO),<br>69.5 (fixed air gap) |
| Air gaps with RS [cm] | Dedicated nozzle with PBS:<br>Monoenergetic layer (**x**): 37.7 (ISO), 31.1, 24.5, 17.9, 11.3, 6.2<br>SOBP (•): 37.7 (ISO), 6.2<br>Universal nozzle with US and DS:<br>SOBP (•): 37.7 (Iso), 6.2 |
| Snout position [cm] | 42.1 |

**Table 6.1:** Measurement conditions and field parameters for the used extrapolation IC.

## 6.2 Monte Carlo Setup

Based on the working TOPAS model from Section 5.2, one change was done for the investigation of the effect of various air gaps on skin dose for quasi-monoenergetic energies. The second distance of the Kevlar® window (GTR2) was implemented in the simulations, mimicking the experimental setup (compare Section 3.10 and 6.1). Similar to the experimental setup, the air gap distances of 6.2 cm, 11.3 cm and 51.1 cm (RS: 37.7 cm) were scored in TOPAS. In addition, TOPAS was used to investigate air gaps, which were not accessible in the experimental setup of this work. This means, shallower air gap distances of 5 cm and 3.5 cm were set. Like in Section 5.2, similar scoring volume sizes of 5x5x0.001 $mm^3$ were placed in four different depths. The depths were at extrapolation IC $WED$ (32.5 $\mu$m, 65$\mu$m and 97.5 $\mu$m) and at the skin dose depth of 70 $\mu$m (reported as $D_{0.07}$) in a water phantom with a volume of 10x10x10 $cm^3$. The water phantom was adjusted to the air gap distances accordingly. For a comparison with the extrapolation IC, scoring was also done at 3 cm $WED$ (reference depth) for all air gap simulations.

The modeled RS had the same dimension like the original one from the experimental use and was therefore a 4.4 cm thick PMMA model.
Further, a simplified TOPAS study was acquired, scoring particle fluences in a phase space file. A phase space extracts all registered particles of a cross sectional area of a TOPAS volume. The distribution of particles from the nozzle after the exit window were compared to the percentages upstream of the RS. Phase space scorers were located for both setups in front of a water tank with the air gaps according to Fig. 6.1 a) of 3.5, 6.2 cm and at the isocenter plane. $10^8$ protons were used for each of these simulations [17].

## 6.3 Uncertainty Analysis

Similar to Section 5.3, the uncertainties are based on Gum and are divided into $U_a$, $U_{b;dose}$ and $U_{b;depth}$. Due to the three measurements of the extrapolation IC, which are presenting the various entrance windows, the skin doses were calculated using a linear fit. This introduced an additional uncertainty variable called $U_{fit}$ and it was part of the overall uncertainty called $U_{c,0.07}$. The following equation describes the relationship:

$$U_{c,0.07} = \sqrt{U_a^2 + U_{b,Dose}^2 + U_{fit}^2} \tag{6.1}$$

As the measurements are only performed with the extrapolation IC and simulations were done with TOPAS only the corresponding uncertainties of both acquisitions are presented in Table 6.2. There, only the maximum occurring uncertainties for $U_a$ ($U_{a,max}$), $U_{fit}$ ($U_{fit,max}$) and $U_{c,0.07}$ ($U_{c,0.07,max}$) are listed for this investigation. The values of $U_b$ are the same assumptions as in Section 5.3.

| Measuring detector | $U_{a,max}$ | $U_{b,Dose}$ | $U_{b,Depth}$ | $U_{fit,max}$ | $U_{c,0.07,max}$ |
|---|---|---|---|---|---|
| Extrapolation IC | 0.3% | 0.1% (0.4%) | 1.6% | 0.8% | 0.8% |
| TOPAS | 0.6% | - | 0.5 $\mu$m | - | - |

**Table 6.2:** Uncertainty budget for the impact of air gap, RS51 and delivery technique. The here presented uncertainties are divided into the maximum occurring statistical uncertainty $U_{a,max}$ (SEM, 1-sigma statistical uncertainty), $U_b$ as systematic uncertainty and $U_{fit}$ as fitting uncertainty. Moreover, a further categorization was applied for $U_b$: dose uncertainty $U_{b,Dose}$ which includes the backscatter effect of 0.1% and the gradient uncertainty of 0.4% for 100.0 MeV and further the depth uncertainty $U_{b,Depth}$ of 1.6% (see Section 5.3). $U_{c,0.07,max}$ is the maximum occurring dose uncertainty in quadrature after Equation 6.1.

## 6.4 Results

This section is divided into results from monoenergetic field delivery and results obtained from SOBP delivery. Further, the TOPAS MC secondary particle production study is presented in the last section.

### 6.4.1 Skin Doses For Monoenergetic Fields In PBS

In a first view, the experimental and simulated skin dose results of the three quasi monoenergetic energies are presented in Figure 6.2. The plot is showing the skin dose $D_{0.07}$ normalized to 3 cm against several air gap distances. The experimental data cover the air gap range between 6.2 cm and 51.1 cm. Shallower air gap depths were investigated with TOPAS MC, where no experimental measurements could be performed, see Figure 6.2. The percentage skin dose is for all three energies constant until an air gap of 11.3 cm. Normalized to 3 cm, it is for 100.0 MeV around 79%, for 150.0 MeV approx. 86% and for the highest energy of 226.7 MeV approx. 87%. Taking a look into shallower air gap distances in Figure 6.2, the skin doses rise for the monoenergetic energies without an RS. Comparing the TOPAS results between the isocenter air gap at 51.1 cm and the shortest air gap of 3.5 cm, there were changes in the order of 1%, 1.5 % and 2.4% for 100.0 MeV, 150.0 MeV and 226.7 MeV, respectively.
The next Figure 6.3 compares the skin doses for various air gaps for the same energy. The red data was obtained from the 120.4 MeV raw isocenter energy from the cyclotron, whereas the black data describes a 150.3 MeV beam, reduced by a RS51 to obtain the same energy of 120.4 MeV. In short term, the plot describes the effect of the RS on the skin dose for the investigated air gaps. The normalized skin doses $D_{0.07}$ to 3 cm for both fields are almost constant and identical between an air gap of 51.1 cm (isocenter) and 24.6 cm. Within the interval of measured air gaps 18.6 and 6.2 cm an increase in the skin dose by the RS was obtained. In detail, the skin doses determined with the extrapolation IC changed from 83.9±0.6% (83.7±0.5%) to 85.3±0.4% (84.4±0.3%) with the inserted RS51 for an air gap of 6.2 cm (11.3 cm) [17]. Therefore, the effect of the RS51 resulted in an increase in skin dose of +1.4% (+0.7%). For the same air gaps, an equivalent skin dose increase was observed with TOPAS: +1.3% (6.2 cm) and +0.7% (11.3 cm). The largest dose difference of 1.7% was obtained for the smallest investigated air gap of 3.5 cm using TOPAS. Again, the full air gap range (37.7 cm - 3.5 cm) results with TOPAS for the use of RS51 showed a dose difference of 3.6%. For the same full air gap range without RS a reduced increase of 1.6% was observed (TOPAS to TOPAS). All in all, the skin dose results obtained from both methods are within their uncertainties and the maximum offset was 0.6%.

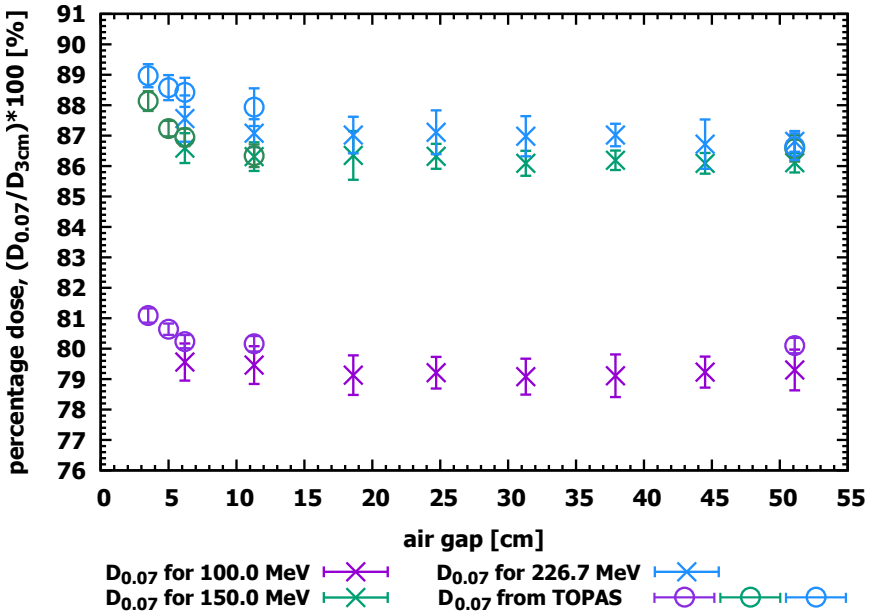


**Figure 6.2:** Results for skin doses $D_{0.07}$ at various air gap distances for monoenergetic energies. Experimental data were measured with extrapolation IC and simulated results were obtained from TOPAS MC.

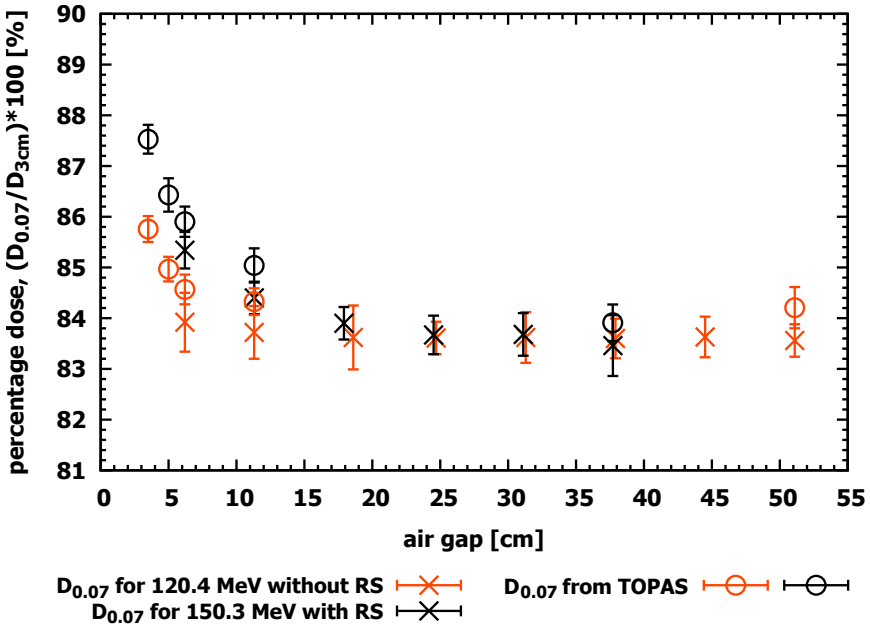


**Figure 6.3:** Comparison of skin doses $D_{0.07}$ at various air gap distances for the same energy: raw isocenter energy of 120.4 MeV from the cyclotron and 120.4 MeV obtained by reducing 150.3 MeV with a RS of 5.1 cm thickness. Experimental data were measured with extrapolation IC and simulated results were obtained from TOPAS MC.

A more detailed view of the effect of the RS51 is displayed for the smallest common air gap of 6.2 cm in Figure 6.4. There, measurement and simulation data $D_M$ are presented in the depth dose curves in shallow depth (up to 100 $\mu$m). Here, the dose influence by the RS (in black) is obvious and describes a constant offset of approx. 1.3%. Both data points are matching within their uncertainty, except of one measurement point at 120.4 MeV.

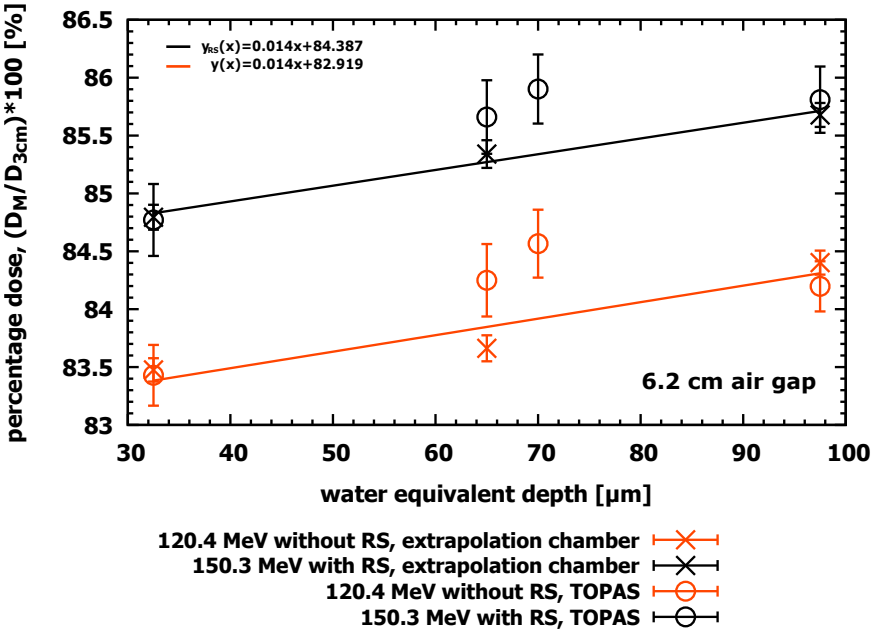


**Figure 6.4:** Detailed skin dose results of the extrapolation IC and TOPAS results for 120.4 MeV with and without RS51 at an air gap of 6.2 cm. The skin dose is plotted against the $WED$ in $\mu$m. Further, a linear fit is presented, which was used to interpolate for $D_{0.07}$. The picture was taken from Ref. [17].

### 6.4.2 Delivery Mode Dependence Of Skin Doses For SOBPs

The following Figure 6.5 summarizes the results obtained for the R20M10 SOBP field for the three delivery techniques with and without RS.
The PBS SOBP skin dose results show no difference between both measurement positions fixed isocenter (Iso at 51.1 cm) and fixed air gap (69.5 cm), see Figure 6.5 a). Skin doses $D_{0.07}$ were 86.2±0.4% and 86.3±0.4%, respectively. At fixed Iso, the air gap for US and DS was 100.0 cm. The obtained result for the US skin dose $D_{0.07}$ was 87.5±0.5% and therefore +1.3% higher than the PBS result. The largest skin dose was measured for the DS technique, which was 0.6% higher than US (fixed Iso).

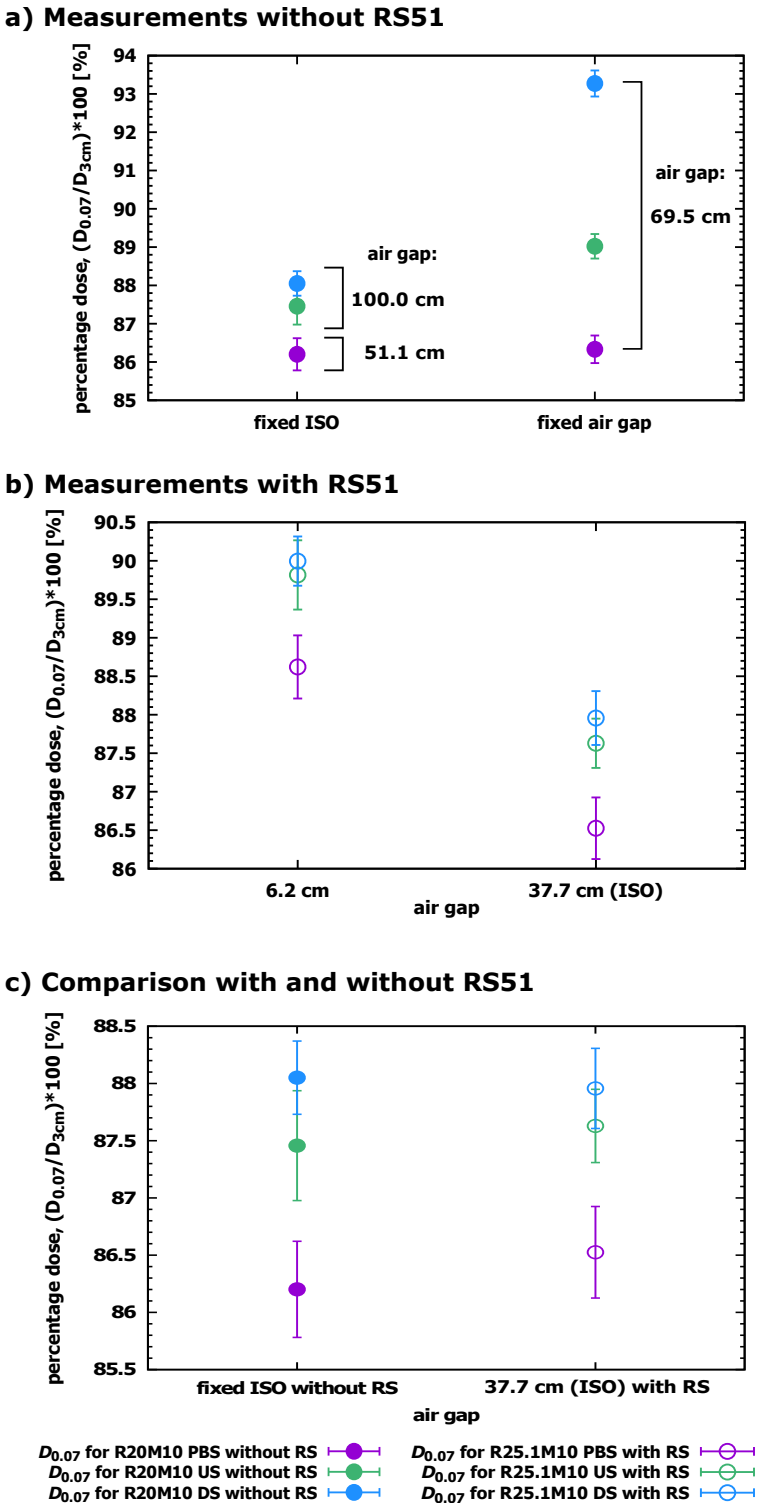


**Figure 6.5:** Skin doses $D_{0.07}$ measured with SOBPs for different delivery modalities and air gaps. The results were normalized to the dose at 3 cm reference depth. a) PBS, US and DS measurements without RS at fixed isocenter (51.1 cm air gap distance for PBS and 100.0 cm air gap distance for US and DS) and at fixed air gap (distance of 69.5 cm). b) Skin doses $D_{0.07}$ results for PBS, US and DS in combination with the RS51 for two air gaps: 6.2 cm and 37.7 cm (isocenter distance). c) Comparison between the results with RS and without at isocenter position. Reproduction according Ref. [17].

Further, Figure 6.5 a) shows the investigation of the fixed air gap distance (69.5 cm), which yielded in an increase of +1.5% for US and +5.2% for DS compared to fixed Iso (100.0 cm) results.
The next results are provided by Figure 6.5 b) for SOBP measurements with RS51. Again, the skin dose for the energy-degraded R20M10 field yielded higher doses for the US/DS techniques with the universal nozzle than for PBS with the dedicated nozzle. In addition, the skin doses are higher for a smaller air gap (6.2 cm) against the Iso distance (37.7. cm) for all three delivery techniques, which is similar to the trend of the monoenergetic energies in Figure 6.3. In detail, this means for PBS, a change by +2.1% from 86.5±0.4% to 88.6±0.4%. In a similar order of magnitude, the skin dose results increased for US from 87.6±0.3% to 89.8±0.5% (+2.2%) and for DS from 88.0±0.4% to 90.0±0.3% (+2.0%).
Figure 6.5 c) is a comparison between the use of the RS and none at isocenter position of the data mixed from 6.5 a)+b). The skin doses for PBS, US and DS agree within their uncertainties between both isocenter positions and again, it is similar to the results between the two air gaps 37.7 cm (with RS) and 51.1 cm (without RS) for monoenergetic energies from Figure 6.3.

### 6.4.3 Secondary Particle Production After Nozzle Exit Window And After RS

The phase space scoring after the PBS dedicated nozzle exit window and after RS was done for the highest and lowest energy of 100.0 MeV and 226.7 MeV. The results are presented in a graphical plot in Figure 6.6. On the left (Figure 6.6 a)) side are the scored particles (primary and secondary protons, electrons, neutrons and gammas) as percentage of the original histories of $10^8$ protons for 100.0 MeV. In Figure 6.6 b) for 226.7 MeV, respectively. The x-axis is representing the three air gap distances: 3.5 cm, 6.2 cm and at isocenter (51.1 cm). Due to a high percentage difference between the primary protons and the other particles, the plot itself was separated for a clearer view. In general, three main observations can be made. First, the amount of primary protons is higher after the nozzle exit window than for after RS for both energies. Second, it is the other way around for the the other particles, which occurred more often after RS than after the Kevlar® window. Further, with increasing air gap up to the isocenter plane, the particle fluences decreased continuously after RS, whereas a nearly constant amount of particles were found for neutrons, photons, primary and secondary protons after the nozzle exit window. This effect is visible in Figure 6.6.
To elaborate and present the difference of the use of the RS on the secondary particles production in more detail, the two Tables 6.3 list the difference between particles generated after RS minus after Kevlar®. More focus can be set to electrons and secondary protons according Table 4.14, which, in addition to the primary protons, contribute most

to the dose in the surfaces area. Secondary protons and electrons are scored with +1.1% and +0.4% more after RS than after nozzle exit window at 3.5 cm air gap for 100.0 MeV. In the same air gap measurement depth, secondary protons and electrons occurred +3.8% and +0.6% more often after RS for the highest energy. Other particles such as neutrons and photons were doubled or even more after using an RS. The highest difference between after RS and after Kevlar were +5.9% for neutrons and +4.8% for photons at 226.7 MeV and an air gap distance of 3.5 cm. Primary protons were the only type of particles, which were scored in a reduced amount after RS. In detail it is about -5.4% for 226.7 MeV and even more a loss of primary protons of -7.8% for 100.0 MeV, both for scoring at isocenter.

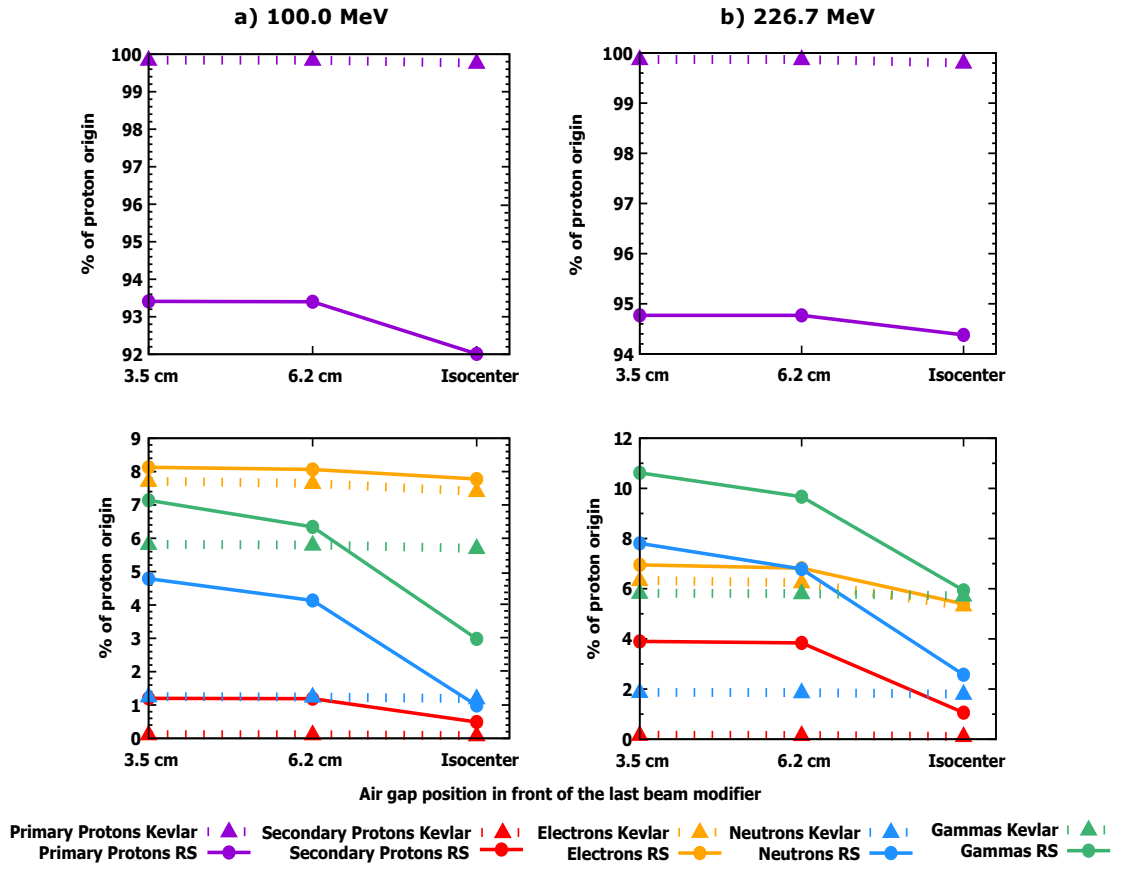


**Figure 6.6:** Graphical presentation of the scored particles after nozzle exit window and after the range shifter for two different energies and three air gaps for the PBS technique. The particles are primary and secondary protons, electrons, neutrons and gammas. The number of particles are shown as percentage of the original histories of $10^8$ protons.

| 100.0 MeV | | | |
|---|---|---|---|
| Particles | Difference of particles: after RS - after Kevlar [%]: air gap of 3.5 cm | air gap of 6.2 cm | at isocenter |
| Primary protons | -6.4 | -6.4 | -7.8 |
| Secondary protons | +1.1 | +1.1 | +0.4 |
| Electrons | +0.4 | +0.4 | +0.4 |
| Neutrons | +3.5 | +2.9 | -0.2 |
| Gammas | +1.3 | +0.6 | -2.7 |

| 226.7 MeV | | | |
|---|---|---|---|
| Particles | Difference of particles: after RS - after Kevlar [%]: air gap of 3.5 cm | air gap of 6.2 cm | at isocenter |
| Primary protons | -5.1 | -5.1 | -5.4 |
| Secondary protons | +3.8 | +3.7 | +1.0 |
| Electrons | +0.6 | +0.6 | +0.1 |
| Neutrons | +5.9 | +4.9 | +0.8 |
| Gammas | +4.8 | +3.9 | +0.2 |

**Table 6.3:** Difference of particles between after RS and after nozzle exit window Kevlar® for 100.0 MeV and 226.7 MeV. The scored particles in TOPAS were primary and secondary protons, electrons, neutrons and gammas at three different air gap positions.

# Chapter 7

# Surface Extrapolation Factor

A surface extrapolation factor (Sef) has been introduced for future simple skin dose estimation. This factor scales back the first depth measurement normalized to 3 cm of a detector $D_{M1}$ used in this work to obtain the skin dose in 70 $\mu$m determined by the extrapolation IC $D_{0.07}$. The Sef is defined as follows:

$$Sef = 1 - \frac{D_{M1} - D_{0.07}}{D_{0.07}} \tag{7.1}$$

At the beginning, the Sef is introduced for the EBT3 & HD-V2 films, the IBA PPC05 IC and for the thermoluminescent dosimeter (TLD). The data for the determination of the Sef (Eq. 7.1) are taken for $D_{0.07}$ from Table 5.4. $D_{M1}$ were introduced as part the measured depth dose curves in Figures 5.2, 5.3, 5.4. In detail, the effective point of measurement $D_{M1}$ was 8 $\mu$m for the HD-V2 film, 43 $\mu$m for the TLD, 179 $\mu$m for the EBT3 film and 1560 $\mu$m for the PPC05 IC. The results are displayed in Table 7.1.

| Energy [MeV] | Surface extrapolation factor Sef | | | |
|---|---|---|---|---|
| | HD-V2 film | TLD | EBT3 film | PPC05 |
| 100.0 | 0.985 ± 0.035 | 0.996 ± 0.024 | 0.974 ± 0.011 | 0.986 ± 0.004 |
| 150.0 | 0.999 ± 0.033 | 1.024 ± 0.019 | 0.976 ± 0.015 | 0.961 ± 0.008 |
| 226.7 | 1.015 ± 0.030 | 0.984 ± 0.032 | 0.977 ± 0.010 | 0.963 ± 0.003 |

**Table 7.1:** Surface extrapolation factor (Sef) for the measuring devices used in this work. The Sef was determined for the EBT3 film, the IBA PPC05 chamber, the HD-V2 film and the thermoluminescent dosimeter (TLD) and for three proton energies: 100.0 MeV, 150.0 MeV and 226.7 MeV. Further, the detectors are increasing in their $WED$ from left to right: 8 $\mu$m, 43 $\mu$m, 179 $\mu$m and 1560 $\mu$m.

The variation of the Sef ranges from the minimum 0.961 for the PPC05 to a maximum value of 1.024 for the HD-V2 film. whereas the EBT3 film stack has an almost constant surface extrapolation factor. One would expect that with increasing measuring depth the

Sef decreases from the absolute value 1 and vice versa for depths below 70 $\mu$m. This can be observed partly with the PPC05 chamber and with the EBT3 films (see Table 7.1). For HD-V2 film and TLD, both with a low measurement depth, there is a larger variation of Sef, which is dominated by the detectors higher uncertainty.
The PPC05 IC showed the lowest uncertainties and is a common detector in the proton therapy and therefore in the clinics. For this reason, the PPC05 IC was further used to perform additional measurements with the investigated fields from Chapter 6. In detail it were a quasi-monoenergetic PBS field with an energy of 120.4 MeV and the SOBP field R20M10 for all three delivery techniques (PBS, US and DS). The Sef results are presented in the table below:

| Field name | Sef for PPC05 at ISO |
|---|---|
| PBS 120.4 MeV | 0.977 ± 0.004 |
| PBS R20M10 | 0.964 ± 0.005 |
| US R20M10 | 0.966 ± 0.006 |
| DS R20M10 | 0.962 ± 0.004 |

**Table 7.2:** Additional Sef measurements with the PPC05 IC. The measurements included the fields from Chapter 6, taking the remaining quasi-monoenergetic energy of 120.4 MeV and the SOBP field R20M10 for all three delivery techniques into account. The first measurement depth of the PPC05 IC is at 1560 $\mu$m.

The resulting factors for the SOBP fields are matching taking their uncertainties into account. This means the Sef is in the same order of magnitude for all three delivery techniques. The Sef of 0.977± 0.004 lies between the Sef of 100.0 MeV and 150.0 MeV from Table 7.1.

# Chapter 8

# Discussion

## 8.1 Determination Of Surface And Skin Dose of Pristine Bragg Peaks

The determination of the skin dose ($D_{0.07}$) at 70 $\mu$m water equivalent depth was investigated by an experimental and a simulation approach. From the various detectors used in this work, the PTW extrapolation IC was suitable for this purpose. TOPAS was applied as MC, and both approaches matched within their uncertainties regarding the skin dose $D_{0.07}$. In addition, with increasing energy, the results of both methods converged. Comparing the skin dose results normalized at 3 cm of the first three investigated energies (100.0 MeV, 150.0 MeV and 226.7 Mev) in Table 5.4, a lower percentage result was observed for 100.0 MeV. This can be explained by an increased dose at the normalization depth of 3 cm. In this combination of energy and depth, there is not a flat plateau like at the other two higher energies. Instead, there is a rise towards the Bragg Peak for 100.0 MeV and is called a dose gradient. This normalization effect is not that strong for e.g. 2 cm, see Table 5.4, where a more consistent skin dose $D_{0.07}$ was reached for all three energies.

Table 8.1 reminds the energy dependent dose rise in the two presented $WED$ scales in Figures 5.2, 5.3, 5.4. There is a clear relation between the increase of the dose rise and the energy. With higher energy, a stronger rise of percentage dose was observed. In detail it was 1.8% higher in the 0-5 mm $WED$ range and 1.4% in the 0-200 $\mu$m range between 226.7 MeV and 100.0 MeV. This results from the additional produced secondary particles at higher energies.

The extrapolation IC had two strong arguments as choice as reference chamber in this work. First, the extrapolation IC showed a low dose uncertainty $U_{c,Dose}$, which were summarized for all devices in Table 5.3. Second, the property to be delivered with three entrance windows of different thicknesses in micrometer scale. Especially, the 50 $\mu$m (65 $\mu$m $WET$) entrance window can provide an immediate estimation of the skin dose. The

| $WED$ range | Dose rise per energy | | |
|---|---|---|---|
| | 100.0 MeV | 150.0 MeV | 226.7 MeV |
| 0-5 mm | 3.0% | 3.8% | 4.8% |
| 0-200 $\mu$m | 1.4% | 1.7% | 2.8% |

**Table 8.1:** Percentage dose rise of the two $WED$ scales up to 5 mm and up to 200 $\mu$m.

statistical uncertainty $U_a$ was low with a maximum of 0.2% over all measurements and energies. A further contribution of $U_{c,Dose}$ was $U_{b,Dose}$, which covered two systematic uncertainties. The effect of material backscatter, which was determined in the Subsection 4.6 and the gradient uncertainty. The latter systematic uncertainty was considered, due to the normalization effect at 3 cm depth and the higher air gap distance of the extrapolation ICs electrodes. Depending on the dose at this reference depth, the data points at shallower depths were scaled and were further sensitive due to the measurements in a RW3 plate phantom and the resulting $WED$ uncertainties on top. Therefore, the 0.4% gradient uncertainty was introduced for the lowest energy and was negligible for the higher energies. In order to avoid this uncertainty at lower energies, a normalization to a different depth (e.g. 2 cm) is possible.
TOPAS, as a second tool for the skin dose determination showed a good agreement to the extrapolation IC with small differences of typically <1% along the depth dose curve. A dose difference of 1.4% was observed as maximum.
In summary, the extrapolation IC is suitable for surface dose measurements. However, it should be noted, that the extrapolation IC is not part of standard proton dosimetry equipment. That is why, other detectors were considered in this work.
The Gafchromic™ films benefited from the usage of FilmQA Pro™. With the software it was possible to minimize the uncertainties using multichannel film dosimetry. Micke et al. (Ref. [181]) were presenting and explaining the nonuniformity correction and the compensation of e.g. anomalies, artifacts, disturbances, the thickness of the active layer, scanner nonlinearity and noise. Therefore, $U_{b,Dose}$ resulted to a maximum of 1.0% for EBT3 films, a little bit higher in combination with the PMMA wedge to 1.4% and to the highest uncertainty of 2.8% for HD-V2 film. The latter one is showing, that the HD-V2 films are more sensitive in handling than the EBT3 films. HD-V2 films are missing the second polyester foil and are sensitive to external influences. Both uncertainties were contributing into to a higher combined dose uncertainty $U_{c,dose}$. A further disadvantage of the HD-V2 is the higher suitable dose range starting at 10 Gy and the resulting lack of sensitivity with lower doses. Therefore, it is not comparable to the clinical setting.
With TOPAS and a continuous depth dose sampling for the surface dose, it was possible to make some further statements, like the determination of the build-up range and the corresponding build-up size. A very early publication from Carlsson and Carlsson showed

a 185.0 MeV proton build-up measured by LiF-teflon dosimeters in a polytetrafluorethylene ($C_2F_4$) phantom. There, the maximum range of electrons had a path length of 0.8 mm in $C_2F_4$, which is equivalent to 1.5 mm in soft tissue [25]. Other published ranges were e.g. approx. 400 $\mu$m in water at 100.0 MeV and 1100 $\mu$m in water at 220.0 MeV [30] or approx. 1000 $\mu$m in polyethylene at 220.0 MeV [31]. In comparison to the other published data, the chosen TOPAS settings in this work were comparable (results from this work were approx. 375 $\pm$ 25 $\mu$m for 100.0 MeV, 725 $\pm$ 25 $\mu$m for 150.0 MeV and 1075 $\pm$ 25 $\mu$m for 226.7 MeV). Further, it is hard to determine the exact end of the first build-up, the electron build-up, due to the overlap with the nuclear build-up. Therefore, most of the published data found the electron build-up empirically [30, 31].
The build-up size was determined by the start and range of the build-up. The starting point was the the first TOPAS scoring point. As expected, there was an increase in build-up with rising proton energy [16]. The size of the build-up for the three energies 100.0 MeV, 150.0 MeV and 226.7 MeV was as follows: 1.8%, 4.3% and 5.8%. A comparable result was reported from Pfuhl et al. with 6% for 220.0 MeV. This strongly corresponds to the value gained from TOPAS and accordingly to the experimental results of our measurements. The obtained data show results which are comparable with the other publication. It must be emphasized however, that there are differences in the geometrical setup [16].

## 8.2 Impact Of Air Gap, Range Shifter And Delivery Technique On Skin Dose In Proton Beam Therapy

The determination of the skin doses ($D_{0.07}$) at 70 $\mu$m water equivalent depth were investigated for the use of RS, for various air gaps and the three delivery modalities at WPE. Again, there was an experimental and a simulation approach. The limitations of the experimental setup was complemented by TOPAS for e.g. smaller air gaps. Both approaches matched within their uncertainties, TOPAS results to extrapolation IC results (compare Figures 6.2, 6.3, 6.4).
Extrapolation IC uncertainties for the skin dose results had an overall dose uncertainty of $U_{c,0.07,max}$ of 0.8%. The most dominant factor contributing to the overall uncertainty was the fitting uncertainty $U_{fit,max}$ with 0.8%, as the skin dose $D_{0.07}$ was determined by interpolating the measured data of the three extrapolation IC entrance windows. The maximum statistical uncertainty $U_a$ was 0.3% (see Table 6.2). Due to the normalization to a reference depth of 3 cm, most uncertainties were canceled out. In comparison to the first part of this work (see Chapter 5 and Section 8.1) the overall uncertainty was higher due to the following points: More setups of the extrapolation IC; different delivery

modalities; and the included fitting uncertainty. TOPAS MC had a comparable statistical uncertainty of max 0.6% (Chapter 5: 0.7%), which was only used for simulations of PBS delivery.
The Figures 6.2 and 6.3 are showing monoenergetic energies, which are not used clinically, but more in the context of QA. However, they are examined in the academic interest by covering the energy range of the IBA system at WPE. The experimental determined skin doses for various air gaps and without RS were almost constant in the range between isocenter (51.1 cm) and 6.2 cm air gap. This air gap range covers the used clinically range. The percentage doses were normalized to 3 cm, and the skin doses raised with higher energy, comparable to the first results in Chapter 5 for a different PBS room. The maximum offset to TOPAS was 0.8%, which showed a good agreement for both approaches. Partly seen with the air gap result of 6.2 cm, lower investigated air gaps (<6.2 cm) simulated with TOPAS revealed a smaller rise of skin dose by varying up to 2.4 % (226.7 MeV, Figure 6.2). The resulting dose increase when reducing the air gap may be the effect of a slightly increased primary proton and electron fluence (see Figure 6.6).
Similar to Chapter 5 and Section 8.1, the lower percentage skin doses for 100.0 MeV and 120.4 MeV in comparison to higher energies is related to the choice of normalization depth at 3 cm [16, 178]. Therefore, the normalization output may vary by choosing a different normalization depth like the 2 cm shown in Table 5.4. The depth depends on the decision of the physicists in the clinic and also of the energy range of the cyclotron.
From a clinical point of view, the investigation of the effect of an inserted RS in Figure 6.3 is more important. At WPE, there were two different RS thicknesses to pull back the proton beam when treating tumors close to the surface. Here, the RS51 was chosen, which is the thinner RS. The results are showing, that there is a higher skin dose observed for air gaps lower than 11.3 cm. In detail it was found a 1.7% (1.4%) increase in skin dose by inserting a RS51 at the air gap of 3.5 cm (6.2 cm). The higher skin dose due to the RS is visible in Figure 6.6 and Table 6.3. There is an general increase of secondaries after the RS, in special secondary protons [182]. The most contributing particles for the dose were the secondary protons and electrons (compare also Section 4.5). Both particles are increased in lower air gaps than at isocenter.
Figure 6.6 and Table 6.3 are summarizing the fluence distribution normalized to original histories and the delta difference of particles between after the nozzle exit window and after RS. The listed air gaps are the similar ones, which were simulated and measured. Therefore the increased particle influence has an impact on the skin dose. As mentioned before, secondary protons were produced after the RS. These secondary protons have a low energy, and thus a high linear energy transfer (LET), which lead to high energy deposition close to the origin and consequently to an increased dose [17]. As the electron fluences are contributing to the build-up, there is a varying dose effect due to a reduced air gap and by the RS [30]. Taking a closer look into Figure 6.6, it reveals a higher

primary proton loss, when inserting the RS in the beam path. Due to the wide angle scattering for lower energy protons, the possibility of forward scattering is decreased for 100.0 MeV compared to 226.7 MeV and downstream of the RS [17, 20, 86]. Further, the percentage of one of the main particles contributing to the dose, the secondary protons, were reduced at 3.5 cm air gap from 3.9% (1.2 %) to 1.1% (0.5 %) at isocenter for 226.7 MeV (100.0 MeV) after the RS. These observations and the decrease in the skin dose with larger air gaps suggest that low energy secondary protons are scattered away and have no impact on measurements at larger air gaps [17].

Comparing the results of PBS single layer (Figure 6.2 & 6.3) and PBS SOBP (Figure 6.5) show a similar behavior, when inserting the RS. In one hand Figure 6.5 a) displays a similar skin dose for both air gaps, this is similar to the monoenergetic energies, but in an extended air gap range of Figure 6.2. On the other hand Figure 6.5 b) presents a skin dose increase of +2.1% between the measured air gaps of 37.7 cm (isocenter) and 6.2 cm by inserting the RS. This is nearly similar to the value found for the rise at monoenergetic energies: +1.8%. As Ref. [17] is mentioning, the skin dose - air gap relation can be assumed as similar for PBS SOBPs as it was investigated for monoenergetic energies.

The results of Figure 6.5 are clearly showing, that the skin dose is dependent on the delivery technique. The lowest skin doses were observed for PBS, whereas the largest skin doses were measured for DS. In between, there were the results for US. The order of the results is due to the difference in the nozzle design. The PBS dedicated nozzle was designed in order to keep the scatter and therefore the production of secondaries low [17]. The universal nozzle needs the range modulation wheel to perform US and DS technique. Then depending on the delivery mode, the US requires the scanning magnets and the scatterer for DS. Therefore, the additional amount of material (nozzle components) in the pathway are the main contributor for a higher skin dose (see Figure 6.5). In Ref. [16] a normalization to 2 cm resulted to a more common percentage skin dose through the investigated monolayer energies (100.0 MeV, 150.0 MeV, 226.7 MeV). Here, a different normalization will not change the order of the skin dose ranking of the three delivery techniques PBS, US and DS. A study from Arjomandy et al. also compared the surface dose of the universal and PBS dedicated nozzle, which resulted in higher doses for the universal nozzle [183]. This is comparable to the results of this work. Figure 6.5 a) depicts the effect of generated secondary particles. This means e.g. a constant skin dose for PBS for the two different air gap positions fixed ISO (51.1 cm) and fixed air gap (69.5 cm) and a difference of +5.2% for DS and +1.5% for US delivery. This indicates a higher particle production for US/DS as introduced with Figure 6.6 after nozzle exit window. The resulting increase in dose and measuring close to the nozzles aperture point out two effects: First, Daartz et al. revealed that the brass aperture serves as secondary proton source [184]. Here in this work a centered square opening 10 $\times$ 10 $cm^2$ aperture (2 $\times$ 3.3 cm thick, brass) was used. The second effect on dose may be caused by the

secondary particles which was investigated by Schneider and Hälg [185, 186]. The results for the simulation of the generated secondary particles in this work were presented in Figure 6.6 and Table 6.3 for the PBS technique. There, it was shown, that the fluence of the secondary particles increased to lower air gaps. Regarding the universal nozzle and the two deliveries US and DS, the impact of the generation of new particles may be higher than for the dedicated PBS nozzle (see Figure 6.6). A further impact on dose due to secondary particles is displayed in Figure 6.5. Comparing the setup in Figure 6.1, the measurement position of fixed air gap (69.5 cm Figure 6.5 a)) without RS and the air gap 6.2 cm (Figure 6.5 b)) with RS are identical. The results of both measurements revealed, that a lower skin dose was obtained with RS than without for DS technique. In contrast, in PBS, it was the other way around and a higher skin dose was observed with RS. The US results were approx. in the same order of magnitude. The difference could again be related to the secondary particles from the nozzle and the interactions with the RS. This effect needs to be considered in future research. Figure 6.5 c) is describing the results obtained at isocenter for all three delivery techniques with and without RS. Here, it is a similar behavior like for the monoenergetic energies in Figure 6.3.
The combination used in this work of both delivery techniques US and DS with the RS is not available in the clinical patient routine. As introduced in the theory chapter and in Figure 2.12 patient specific apertures and compensators are milled for the passive techniques. A uniform straight RS may be regarded as the simplest version of range compensator. But, this combination can be applied for QA activities or non clinical academic questions or cell studies.

## 8.3 Surface Extrapolation Factor

As already mentioned, the extrapolation IC is not a common detector in clinics. Therefore, in this work a surface extrapolation factor (Sef) was introduced (Chapter 7). The idea was to give a simple skin dose estimation at 70 $\mu$m using the Sef with the detectors first measurement value (without any additional physical build-up). The Sef was introduced for three energies at isocenter plane and various detectors from this work (Table 7.1). After choosing the PPC05 as the most suitable detector for this purpose, some additional Sef were calculated in the scope of Chapter 6, see Table 7.2.
In detail, the Sef was calculated for some standard dosimetric devices such as Gafchromic™ films, the PPC05 IC and TLDs. Suitable was the PPC05 IC due to the fact, that the measurement uncertainties ($U_a$) were the smallest ones. This resulted in a Sef uncertainty between 0.3% and 0.8%. The EBT3 film showed a constant Sef between 0.974 and 0.977 for the three energies. This energy independent effect could be a result of the

uncertainty $U_{b,Depth}$ of ± 15 $\mu$m and therefore the averaging of the dose in the effective point of measurement (179 $\mu$m $WED$) and at normalization depth (3 cm $WED$). The EBT3 film is also suitable due to the user friendly energy independence, but needs more time for evaluation and comes with higher uncertainties (see Table 5.3). The surface extrapolation factors of the TLD and the HD-V2 film are not recommended due to their large uncertainties, which are a further propagation of $U_a$ and $U_{c,Dose}$, respectively. As a result, the Sef are fluctuating randomly between the energies from 0.984 to 1.024. Ideally, a lower Sef should be resulting for measurements at higher $WED$, and a higher factor for measurements with lower $WED$. Therefore, the output of each detector describes the Sef.
The Sef is limited in the scope of this work. There are several limits, like the Sef is covering a small amount of monoenergetic energies and one defined SOBP, which are not clinical relevant, but more for academic purpose or applied in QA. The best suitable detector, the IBA PPC05 IC may not be an inventory of every proton clinic and the presented Sefs here, were obtained with a dedicated IBA nozzle. However, the IBA nozzle is widely available and can show comparable results for the Sef. Further, in the frame of an alternative interpretation, the Sef can be regarded as uncertainty in the determination of the skin dose by a detector's shallowest measurement depth [16]. An extension of the use of the Sef results from the air gap investigations of the skin dose. Figures 6.2 & 6.3 allow the Sef to be applicable for monoenergetic fields and PBS SOBPs for combinations, where the skin dose was constant during the air gap range.

## 8.4 Skin Dose

In this work several quasi-monoenergetic and SOBP fields were applied for measuring and scoring the skin dose with various clinical parameters like the usage of the RS or the air gap. From a clinical point of view, the quantification of skin dose in proton therapy may lead to further correlations between absorbed dose and skin toxicity. As common side effect of radiation, several publication reviewed the skin toxicity for photon treatment in general like Refs. [187, 188] or to specific treatment areas like head and neck [189], breast cancer [190] or cranial region [191]. Further, skin toxicity paper were published focusing on the effect of proton therapy [192, 193, 194, 195] or in comparison of proton and photon therapy [196, 197]. Therefore the current study may provide a dosimetric link to skin studies with other beam qualities.
In this work several contributions were made. One is e.g. the depth dose curve measurements to shallow depths down to 8 $\mu$m $WED$. As treatment planning systems are limited due to imported depth dose curves in water for the beam model and in the granularity of the dose grid, such shallow depths are not covered by the TPS. Further, an

implementation of the depth dose curves of this work cannot be implemented directly in TPS. The surface extrapolation factor might be an option to avoid this limitation.
This work made use of the skin dose in an effective depth of 70 $\mu$m. This concept, which was established for radiation applications could be too simplistic for clinical use and for radiobiology research [2, 11, 16, 198]. Together with the published depth dose curves, both information may help for further evaluations regarding the skin dose [16].
A further contribution of this work were the findings of the skin dose in various measurement conditions like delivery modality, air gap dependency applied with open fields or RS. Regarding skin protection some suggestion can be made from this work. First, the choice of the delivery technique. Figure 6.5 is presenting a lower skin dose obtained with PBS. Therefore the US/DS technique should be replaced by the PBS technique. Second, the choice of the RS and its thickness. The skin dose increased mainly due to secondary proton generation of the RS51 (see Table 6.3) in comparison without an RS. A new study showed, that the effect on skin dose increase is proportional to the inserted RS and its thickness [199]. At WPE, there are two different RS sizes for different tumor localization for PBS: RS51 and RS74. Therefore a higher increase in skin dose can be excepted when inserting RS74 at shallow air gaps than with RS51. Further, the knowledge can be transferred in the planning process. One can choose a thin RS or none for skin sparing at small air gaps. If a thicker RS is required due to the limited cyclotron energy range and a tumor close to the surface, one can realize it according Figure 6.3 with e.g. an increased air gap starting at approx. 18-25 cm and larger to receive a constant skin dose [17].
Due to the results, a simple guideline could be developed to see the impact on the skin dose reflecting the impact of RS and the air gap. This is presented in Table 8.2. By sparing one effect, an other effect may be compromised in the planning. Here, both impacts, RS and air gap, have e.g. an influence on lateral penumbra. The latter, and the distal gradient may also be factors to be considered in TPS to spare organs at risk. In general, treatment planning may be a trade-off of various factors, like e.g. to cover the treatment volume by sparing the organs at risk or here by sparing the skin. According to Table 8.2 the skin dose is effected by a small air gap. By using a RS, this effect is enhanced ($\uparrow\uparrow$). For larger air gaps, the skin dose is not effected when using a RS or not (-). Further, the lateral penumbra becomes wider with larger air gaps ($\uparrow$) and with the RS ($\uparrow\uparrow$) and vice versa ($\downarrow\downarrow$ /RS: $\downarrow$).

However, treatment planning is not straight forward. Each proton patient case is individual and requires expertise from a medical physicist. A lot of the planning result depends on the used algorithm of the TPS and from the optimizer, which are chosen to treat the target volume optimally. More influence by the user is the choice of further parameters like the field gantry angle, the delivery technique, the use of the RS and the various air gaps. By planning several fields, the application of various RS and air gap distances are

| Case | Effect on skin dose | Effect on lateral penumbra |
|---|---|---|
| Range shifter & large air gap | - | ↑↑ |
| Range shifter & small air gap | ↑↑ | ↓ |
| No range shifter & large air gap | - | ↑ |
| No range shifter & small air gap | ↑ | ↓↓ |

**Table 8.2:** Impact of RS and air gap distances on the skin dose and on the lateral penumbra. One arrow up ("↑") means larger/wider, one arrow down "↓" smaller/narrower, "-" defines not varying and a double arrow (↑↑ or ↓↓ is a stronger effect).

possible. This will result in a non uniform skin dose per field and therefore not straight forward to determine the skin dose in patient specific QA. Table 8.2 might be an option to plan the fields accordingly. Currently there is no recommended avoidance strategy for the skin dose effects. Some publications are reporting about pharmacologic interventions in form of creams or lotions to support the healing of the site effects [200] or to reduce them by applying a film on skin [201]. The majority of publications is comparing the skin dose by calculating photon against proton plans (e.g. Ref. [196]).

# Chapter 9

# Summary and Outlook

This thesis introduced experimental data of the shallow proton depth dose curve and the quantification of the skin dose at 70 $\mu$m water equivalent depth in proton therapy.
In a first investigation, various approaches were evaluated with respect to measurements within the first few micro- and millimeters of water equivalent depth. The characterization of the surface dose of the proton depth dose distribution was sampled by using the PTW extrapolation IC, the IBA PPC05, the TLD and the radiochromic Gafchromic™ films (EBT3 film, EBT3 film + PMMA wedge, HD-V2 film). In addition, the experimental dose was compared with TOPAS Monte Carlo, which was in a good agreement. The extrapolation IC provided results close to the skin depth and featured the smallest uncertainties. The EBT3 film stack and the EBT3 film in combination with the PMMA wedge supplied with continuous dose measurements with one field application. The TLD and HD-V2 film allowed very close surface measurements, but revealed the largest uncertainties.
The skin doses were determined at a depth of 70 $\mu$m using the extrapolation IC and the TOPAS simulations. Normalized to 100% to the dose at 3 cm reference depth, the results for the skin dose obtained with the extrapolation IC were 79.7±0.3% for 100.0 MeV, 86.0±0.6% for 150.0 MeV and 87.1±0.1% for 226.7 MeV. For TOPAS the following results were obtained 80.1±0.2% (100.0 MeV), 87.1±0.5% (150.0 MeV) and 86.9±0.4% (226.7 MeV), respectively.
With the determination of the skin dose at the depth of 70 $\mu$m, further characteristics of the depth dose distribution could be developed. The beginning of the depth dose curve revealed a build-up effect which was energy dependent for length and height. In detail, the TOPAS results for the build-up length for 100.0, 150.0 and 226.7 MeV were approx. 375 ± 25 $\mu$m, 725 ± 25 $\mu$m and 1075 ± 25 $\mu$m. The dose magnitude between the first scoring point and the resulting build-up range were 1.8%, 4.3% and 5.8%. All in all, this thesis provided comprehensive data on surface depth dose curves and skin doses at 70 $\mu$m depth for proton energies of 100.0 MeV, 150.0 MeV, and 226.7 MeV [16].

In the second study the skin dose was further investigated by varying key parameters of a clinical proton treatment plan. These aspects were the range shifter, the air gap and the delivery modality. The following approaches were applied: An experimental approach with the extrapolation IC, and a simulation approach with TOPAS Monte Carlo.
The experimental air gap varied between 6.2-51.1 cm and a non-inserted RS revealed no skin dose dependence for monoenergetic and SOBPs applying the PBS technique. First dose increases were visible for air gap distances <6.2 cm. Quantifying the dose increase within the investigated air gap range between isocenter (51.1 cm) and the lowest air gap obtained by TOPAS of 3.5 cm, TOPAS results showed for monoenergetic energies (and no RS) energy dependent results between 1% (100.0 MeV) and 2.4% (226.7 MeV). The highest impact on skin dose was confirmed when inserting the RS. Here, the RS51 had an impact on the shortest simulation air gap depth of 3.5 cm of 1.7% dose difference against no RS and an increase of dose of 3.7% when comparing against the isocenter air gap distance of 37.7 cm.
The rise in skin dose could be attributed to two effects, the increased electron fluence at small air gaps and the additional hadronic particle production emitted from the RS modality due to design.
The three available proton delivery techniques at WPE were compared by applying an equivalent SOBP beam. As expected, the skin dose was lower for the PBS technique followed by the US and DS techniques and can be explained due to the nozzle design. Whereas the PBS dedicated nozzle was designed to keep the scatter low, the impact on the skin dose by the universal nozzle is given by the beam modulating passive hardware design and the additional generated secondary particles. Here, air gap measurements in front of the snout resulted in a stronger increase of the skin dose (US&DS, fixed air gap). The rise of the skin dose using the RS for all three SOBP application was in the same order of magnitude (approx. 2.1%) as the monoenergetic comparison in the range between 6.2 cm and isocenter [17].

In this thesis, a surface extrapolation factor was developed to estimate the skin dose for various detectors used in this work. It is based on the dose values at the skin depth of 70 $\mu$m. The surface extrapolation factor will be applied on the first detector reading without any physical build-up to obtain a skin dose value. Due to the various investigated detectors and their uncertainties, the Sef may carry significant uncertainties. A suitable detector was the PPC05 chamber for which the uncertainty regarding the factor was the lowest.

As skin side effects may occur during irradiation therapy, these dosimetric proton data can help for skin dose studies and for correlation between absorbed dose and skin toxicity. New data like the height and the range of the build-up effect and the determination of

the skin dose at 70 $\mu$m for various key parameters can support the treatment planning, which has some limitations by calculating the surface dose. As treatment planning is not straight forward, the applied key parameters delivery technique, RS and air gap distance may not only have an impact on skin dose, but also may impact other parameters like the lateral penumbra or in general the dose in the target and at organs at risk.

This work was based on an IBA proton therapy system and there are more vendors with different proton generation techniques available which have different nozzle designs and beam optic systems. Therefore the skin dose or the superficial depth dose distribution may vary.
As Monte Carlo codes can match the clinical beam model, quick skin dose checks can be done via simulation besides the dosimetrical solution with an appropriate detector or using the Sef.
Further, publications, studies and clinics compare the results between photon and proton therapy. The results of this work may support for a closer comparison regarding skin dose of both radiation therapy sources.
The findings of this research may help to improve TPS systems in the surface region of the depth dose. The planning and optimization technique for skin site effects can be improved by the knowledge of the dosimetric background for skin dose.

# List of Figures

# List of Tables

# Acronyms

| | |
|---|---|
| $^{137}CS$ | Radioactive isotop of caesium |
| C2F4 | Tetrafluoroethylene, preliminary stage of teflon |
| CT | Computed tomography |
| CTV | Clinical tumor volume |
| GTV | Gross tumor volume |
| $D_{0.07}$ | Skin dose depth at 70 $\mu$m |
| dpi | Dots per inch |
| DS | Double scattering |
| EBT | External Beam Therapy radiochromic film |
| HD-V2 | high dose-version 2 radiochromic film |
| HU | Hounsfield unit |
| IBA | Ion Beam Applications |
| IC | Ionization chamber |
| ICRP | International Commission on Radiological Protection |
| ICRU | International Commission on Radiation Units and Measurements |
| IMPT | Intensity-modulated proton therapy |
| ISO | Isocenter |
| LET | Linear energy transfer |
| LiF:Mg,Ti | Lithium Fluorine doped with Magnesium and Titanium |
| MC | Monte Carlo |
| MeV | Mega electron volt |
| MLIC | Multi-layer ionization chamber |
| MPA NRW | Materialprüfungsamt North Rhine-Westphalia |
| MRT | Magnetic resonance tomography |
| OAR | Organ at risk |
| PBS | Pencil beam scanning |
| PMMA | Polymethylmethacrylate |
| PPC05 | IBA Plan parallel chamber 05 |
| PTV | Planning target volume |
| PTW | Physikalisch-Technische Werkstätten |
| QA | Quality assurance |
| $R80$ | Range at 80% dose |
| RBE | Relative biological effectiveness |
| RF | Radio frequency |
| RS | Range shifter |
| RS51 | Range shifter of 51 mm water equivalent thickness |
| RW3 | Material of 98% polystyrene + 2% $TiO_2$ |

| | |
|---|---|
| SEF | Surface extrapolation factor |
| SEM | Standard error of the mean |
| SOBP | Spread-out Bragg peak |
| TL-DOS | Thermoluminescence dosemeter system |
| TLD | Thermoluminescent dosimeter |
| TOPAS | TOol for PArticle Simulation |
| TPS | Treatment planning system |
| $U_a$ | Statistical uncertainty |
| $U_{b,Dose}$ | Systematic uncertainty in dose |
| $U_{b,Depth}$ | Systematic uncertainty in depth |
| $U_{c,0.07}$ | Combined dose uncertainty of $U_a$, $U_{b,Dose}$ and $U_{fit}$ in quadrature |
| $U_{c,Dose}$ | Combined dose uncertainty of $U_a$ and $U_{b,Dose}$ in quadrature |
| $U_{fit}$ | Skin dose $D_{0.07}$ fitting uncertainty |
| US | Uniform scanning |
| WED | Water equivalent depth |
| WET | Water equivalent thickness |
| WPE | West German Proton Therapy Centre Essen |

# Bibliography


[1] Particle Therapy Co-Operative Group. Particle therapy facilities in operation. URL `https://www.ptcog.site/index.php/facilities-in-operation-public`, [Last accessed: 22. November 2023].

[2] ICRP Report No. 60. Recommendations of the international commission on radiological protection, 1990.

[3] T. R. Koenig, D. Wolff, F. A. Mettler et al. Skin injuries from fluoroscopically guided procedures. *American Journal of Roentgenology*, 177(1):3–11, 2001.

[4] J. Daniel. The x-rays. *Science*, 3(67):562–563, 1896.

[5] E. A. Codman. The cause of burns from x-rays. *Bos Med Surg*, 135:610–611, 1896.

[6] J. C. L. Chow and G. N. Grigorov. Surface dosimetry for oblique tangential photon beams: A monte carlo simulation study. *Medical Physics*, 35(1):70–76, 2008.

[7] N. Vicoroski, A. Espinoza, M. Duncan et al. Development of a silicon diode detector for skin dosimetry in radiotherapy. *Medical Physics*, 44(10):5402–5412, 2017.

[8] K. Y. Quach, J. Morales, M. J. Butson et al. Measurement of radiotherapy x-ray skin dose on a chest wall phantom. *Medical Physics*, 27(7):1676–1680, 2000.

[9] F. Zibold, F. Sterzing, G. Sroka-Perez et al. Surface dose in the treatment of breast cancer with helical tomotherapy. *Strahlentherapie und Onkologie : Organ der Deutschen Röntgengesellschaft ... [et al]*, 185:574–81, 09 2009.

[10] E. Ishmael Parsai, D. Shvydka, D. Pearson et al. Surface and build-up region dose analysis for clinical radiotherapy photon beams. *Applied Radiation and Isotopes*, 66(10):1438–1442, 2008.

[11] ICRU Report No. 39. Determination of dose equivalents resulting from external radiation sources, 1985.

[12] Y. S. Lee and K. Hwang. Skin thickness of korean adults. *Surgical and Radiologic Anatomy*, 24:183–189, 2002.

[13] J. Sandby-møller, T. Poulsen and H. C. Wulf. Epidermal thickness at different body sites: relationship to age, gender, pigmentation, blood content, skin type and smoking habits. *Acta dermato-venereologica*, 83 6:410–3, 2003.

[14] P. Krackowizer and E. Brenner. Thickness of the human skin 24 points of measurement. *Phlebologie*, 37:83–92, 04 2008.

[15] J. Perl, J. Shin, J. Schümann et al. Topas: An innovative proton monte carlo platform for research and clinical applications. *Medical Physics*, 39(11):6818–6837, 2012.

[16] A. Kern, C. Bäumer, K. Kröninger et al. Determination of surface dose in pencil beam scanning proton therapy. *Medical Physics*, 47(5):2277–2288, 2020.

[17] A. Kern, C. Bäumer, K. Kröninger et al. Impact of air gap, range shifter, and delivery technique on skin dose in proton therapy. *Medical Physics*, 48(2):831–840, 2021.

[18] H. Takei. Physical characteristics of proton beams. In K. Tsuboi, T. Sakae and A. Gerelchuluun, editors, *Proton Beam Radiotherapy*, pages 37–50. Springer, Singapore, 2020.

[19] W. D. Newhauser and R. Zhang. The physics of proton therapy. *Physics in Medicine and Biology*, 60(8):R155–R209, 2015.

[20] B. Gottschalk. Physics of proton interaction in matter. In H. Paganetti, editor, *Proton Therapy Physics*, pages 20–59. CRC Press, Taylor & Francis Group, Boca Raton London New York, 2012.

[21] H. Bethe. Zur Theorie des Durchgangs schneller Korpuskularstrahlen durch Materie. *Annalen der Physik*, 397(3):325–400, 1930.

[22] F. Bloch. Zur Bremsung rasch bewegter Teilchen beim Durchgang durch Materie. *Annalen der Physik*, 408(3):285–320, 1933.

[23] D. J. Thomas. ICRU report 85: fundamental quantities and units for ionizing radiation. *Radiation Protection Dosimetry*, 150(4):550–552, 2012.

[24] H. Krieger. *Strahlungsmessung und Dosimetrie*. Springer Spektrum, 2 edition, 2013.

[25] C. Carlsson and G. Carlsson. Proton dosimetry with 185 mev protons. dose buildup from secondary protons and recoil electrons. *Health physics*, 33:481–4, 1977.

[26] C. Brusasco, B. Voss, D. Schardt et al. A dosimetry system for fast measurement of 3d depth–dose profiles in charged-particle tumor therapy with scanning techniques. *Nuclear Instruments and Methods in Physics Research Section B: Beam Interactions with Materials and Atoms*, 168(4):578 – 592, 2000.

[27] A. Krießbach. *Untersuchung des Wandeffektes von Ionisationskammern bei der Bestrahlung mit relativistischen 12C-Ionen*. Ph.D. thesis, Ruprecht-Karls Universität Heidelberg, 2000.

[28] C. Grassberger and H. Paganetti. Elevated LET components in clinical proton beams. *Physics in Medicine and Biology*, 56(20):6677–6691, 2011.

[29] H. Paganetti, editor. *Proton Therapy Physics*. CRC Press, Taylor & Francis Group, Boca Raton London New York, 2012.

[30] L. Kelleter, B. Zhen-Hong Tham, R. Saakyan et al. Technical note: Simulation of dose buildup in proton pencil beams. *Medical Physics*, 46(8):3734–3738, 2019.

[31] T. Pfuhl, F. Horst, C. Schuy et al. Dose build-up effects induced by delta electrons and target fragments in proton bragg curves—measurements and simulations. *Physics in Medicine & Biology*, 63(17):175002, 2018.

[32] International Commission on Radiation Units and Measurements (ICRU). Nuclear data for neutron and proton radiotherapy and for radiation protection, 2000.

[33] H. Krieger. *Grundlagen der Strahlungsphysik und des Strahlenschutzes.* Springer Spektrum, 4 edition, 2012.

[34] V. Vyas, L. Palmer, R. Mudge et al. On bolus for megavoltage photon and electron radiation therapy. *Medical dosimetry : official journal of the American Association of Medical Dosimetrists*, 38 3:268–73, 2013.

[35] T. Pfeiler. *Dynamic evaluation of 4D robust optimisation for motion management in scanned proton therapy of hepatocellular carcinoma.* Ph.D. thesis, TU Dortmund, 2018.

[36] H. Paganetti. Range uncertainties in proton therapy and the role of monte carlo simulations. *Physics in medicine and biology*, 57:R99–117, 2012.

[37] T. Bortfeld. An analytical approximation of the bragg curve for therapeutic proton beams. *Medical Physics*, 24(12):2024–2033, 1997.

[38] J. F. Janni. Proton Range-Energy Tables, 1 keV-10 GeV, Energy Loss, Range, Path Length, Time-of-Flight, Straggling, Multiple Scattering, and Nuclear Interaction Probability. Part I. For 63 Compounds. *Atomic Data and Nuclear Data Tables*, 27:147, 1982.

[39] E. Pedroni. Treatment delivery systems: pencil beam scattering. In D. T. F. and K. H. M., editors, *Proton and charged particle radiotherapy*, pages 40–49. Lipppincott Williams & Wilkins, Philadelphia, 2008.

[40] T. Bortfeld and W. Schlegel. An analytical approximation of depth - dose distributions for therapeutic proton beams. *Physics in Medicine and Biology*, 41(8):1331–1339, 1996.

[41] D. Jette and W. Chen. Creating a spread-out bragg peak in proton beams. *Physics in Medicine and Biology*, 56(11):N131–N138, 2011.

[42] M. J. Berger, M. Inokuti, H. H. Andersen et al. ICRU report 49. *Journal of the International Commission on Radiation Units and Measurements*, 25(2), 2016.

[43] W. C. Röntgen. Ueber eine neue art von strahlen (ii. mittheilung). *Sonderdruck aus den "Sitzungsberichten der Würzburger Physikal.-medic. Gesellschaft", Würzburg Stahel.*, 1895.

[44] W. R. Leo. *Techniques for nuclear and particle physics experiments: a how-to approach; 2nd ed.* Springer, Berlin, 1994.

[45] G. F. Knoll. *Radiation Detection and Measurement; 3rd ed.* Wiley, New York, NY, 2000.

[46] International Atomic Energy Agency (IAEA). Absorbed dose determination in external beam radiotherapy: an international Code of Practice for dosimetry based on standards of absorbed dose to water. Technical report series 398, 2000.

[47] International Commission on Radiation Units and Measurements (ICRU). ICRU report No. 78, Prescribing, Recording, and Reporting Proton-Beam-Therapy, 2007.

[48] J. T. Randall, M. H. F. Wilkins and M. L. E. Oliphant. Phosphorescence and electron traps - i. the study of trap distributions. *Proceedings of the Royal Society of London. Series A. Mathematical and Physical Sciences*, 184(999):365–389, 1945.

[49] D. W. Rogers and J. E. Cygler. *Clinical Dosimetry Measurements in Radiotherapy.* Medical Physics Publishing, Madison, Wisconsin, 2009.

[50] S. W. S. McKeever. *Thermoluminescence of Solids.* Cambridge Solid State Science Series. Cambridge University Press, 1985.

[51] R. Theinert. *Estimation of fading time and irradiation dose in thermoluminescence dosimetry using uni- and multivariate analysis techniques.* Ph.D. thesis, TU Dortmund, 2018.

[52] S. Devic. Radiochromic film dosimetry: Past, present, and future. *Physica medica : PM : an international journal devoted to the applications of physics to medicine and biology : official journal of the Italian Association of Biomedical Physics (AIFB)*, 27:122–34, 2010.

[53] *Operational health physics during the commissioning phase of the West German Proton Therapy Centre Essen*, Conference Paper: International COnference on Radiation Protection, 2012.

[54] J. Wulff, B. Koska, J. Heufelder et al. Commissioning and validation of a novel commercial tps for ocular proton therapy. *Medical Physics*, 50(1):365–379, 2023.

[55] M. Schippers. Proton accelerators. In H. Paganetti, editor, *Proton Therapy Physics*, pages 61–102. CRC Press, Taylor & Francis Group, Boca Raton London New York, 2012.

[56] H. Krieger. *Strahlungsquellen für Technik und Medizin.* Springer Spektrum, 2 edition, 2013.

[57] F. Hinterberger. *Physik der Teilchenbeschleuniger und Ionenoptik.* Springer, 2 edition, 2008.

[58] R. Slopsema. Beam delivery using passive scattering. In H. Paganetti, editor, *Proton Therapy Physics*, pages 125–156. CRC Press, Taylor & Francis Group, Boca Raton London New York, 2012.

[59] J. Swakon, P. Olko, D. Adamczyk et al. Facility for proton radiotherapy of eye cancer at ifj pan in krakow. *Radiation Measurements*, 45(10):1469–1471, 2010.

[60] A. Kacperek. Ocular proton therapy centers. In U. Linz, editor, *Ion Beam Therapy: Fundamentals, Technology, Clinical Applications*, pages 149–177. Springer Berlin Heidelberg, Berlin, Heidelberg, 2012.

[61] A. Koehler, R. Schneider and J. Sisterson. Range modulators for protons and heavy ions. *Nuclear Instruments and Methods*, 131(3):437–440, 1975.

[62] P. van Luijk, A. A. van 't Veld, H. D. Zelle et al. Collimator scatter and 2d dosimetry in small proton beams. *Physics in Medicine and Biology*, 46(3):653–670, jan 2001.

[63] A. Pérez-Andújar, W. D. Newhauser and P. M. DeLuca. Neutron production from beam-modifying devices in a modern double scattering proton therapy beam delivery system. *Physics in Medicine and Biology*, 54(4):993–1008, jan 2009.

[64] Y. Zheng, E. Ramirez, A. Mascia et al. Commissioning of output factors for uniform scanning proton beams. *Medical Physics*, 38(4):2299–2306, 2011.

[65] J. B. Farr, A. E. Mascia, W.-C. Hsi et al. Clinical characterization of a proton beam continuous uniform scanning system with dose layer stacking. *Medical Physics*, 35(11):4945–4954, 2008.

[66] C. Courtois, G. Boissonnat, C. Brusasco et al. Characterization and performances of a monitoring ionization chamber dedicated to iba-universal irradiation head for pencil beam scanning. *Nuclear Instruments and Methods in Physics Research Section A: Accelerators, Spectrometers, Detectors and Associated Equipment*, 736:112 – 117, 2014.

[67] B. Marchand, D. Prieels, B. Bauvir et al. Iba proton pencil beam scanning: An innovative solution for cancer treatment. *Proc. 7th EPAC (Vienna)*, 01 2000.

[68] M. Durante and J. Loeffler. Charged particles in radiation oncology. *Nature reviews. Clinical oncology*, 7:37–43, 12 2010.

[69] J. Flanz. Particle beam scanning. In H. Paganetti, editor, *Proton Therapy Physics*, pages 157–189. CRC Press, Taylor & Francis Group, Boca Raton London New York, 2012.

[70] D. Jones. ICRU Report 50 Prescribing, Recording and Reporting Photon Beam Therapy. *Medical Physics*, 21(6):833–834, 1994.

[71] T. Landberg, J. Chavaudra, J. Dobbs et al. Report 62. *Journal of the International Commission on Radiation Units and Measurements*, os32(1):NP–NP, 04 2016.

[72] S. Safai, T. Bortfeld and M. Engelsman. Comparison between the lateral penumbra of a collimated double-scattered beam and uncollimated scanning beam in proton radiotherapy. *Physics in Medicine and Biology*, 53(6):1729–1750, mar 2008.

[73] K. Czerska, F. Emert, R. Kopec et al. Clinical practice vs. state-of-the-art research and future visions: Report on the 4d treatment planning workshop for particle therapy – edition 2018 and 2019. *Physica Medica*, 82:54–63, 2021.

[74] D. De Ruysscher, E. Sterpin, K. Haustermans et al. Tumour movement in proton therapy: Solutions and remaining questions: A review. *Cancers*, 7(3):1143–1153, 2015.

[75] P. Tina, A. K. Dalia, A. Myriam et al. Motion effects in proton treatments of hepatocellular carcinoma-4d robustly optimised pencil beam scanning plans versus double scattering plans. *Physics in Medicine and Biology*, 63(23), 2018.

[76] M. C. Harvey, J. C. Polf, A. R. Smith et al. Feasibility studies of a passive scatter proton therapy nozzle without a range modulator wheel. *Medical Physics*, 35(6Part1):2243–2252, 2008.

[77] S. Rana and E. Samuel. Measurements of in-air spot size of pencil proton beam for various air gaps in conjunction with a range shifter on a proteusplus pbs dedicated machine and comparison to the proton dose calculation algorithms. *Australasian Physical & Engineering Sciences in Medicine*, 42, 06 2019.

[78] C. Bäumer, D. Geismar, B. Koska et al. Comprehensive clinical commissioning and validation of the raystation treatment planning system for proton therapy with active scanning and passive treatment techniques. *Physica Medica*, 43:15–24, 2017.

[79] RaySearch Laboratories AB. Proton monte carlo dose calculation in raystation, 2017. URL `https://www.raysearchlabs.com/siteassets/about-overview/media-center/wp-re-ev-n-pdfs/white-papers/proton-monte-carlo-dose-calculation-in-raystation2.pdf`, [Last accessed: 8. April 2021)].

[80] L. Hong, M. Goitein, M. Bucciolini et al. A pencil beam algorithm for proton dose calculations. *Physics in Medicine and Biology*, 41(8):1305–1330, aug 1996.

[81] B. Schaffner, E. Pedroni and A. Lomax. Dose calculation models for proton treatment planning using a dynamic beam delivery system: an attempt to include density heterogeneity effects in the analytical dose calculation. *Physics in Medicine and Biology*, 44(1):27–41, jan 1999.

[82] RaySearch Laboratories AB. Raystation 7 reference manual rsl-d-rs-7.0-ref-en-1.0-2017-12-08, 2017.

[83] J. Saini, E. Traneus, D. Maes et al. Advanced proton beam dosimetry part i: review and performance evaluation of dose calculation algorithms. *Translational Lung Cancer Research*, 7(2), 2018.

[84] RaySearch Laboratories AB. Raystation dose calculation algorithms, 2015. URL `https://www.raysearchlabs.com/siteassets/about-overview/media-center/wp-re-ev-n-pdfs/white-papers/white-paper-7---dose-calculation-aug-2015.pdf`, [Last accessed: 7. April 2021)].

[85] L. Eyges. Multiple scattering with energy loss. *Phys. Rev.*, 74:1534–1535, Nov 1948.

[86] B. Gottschalk, A. M. Koehler, R. J. Schneider et al. Multiple Coulomb scattering of 160 MeV protons. *Nuclear Instruments and Methods in Physics Research B*, 74(4):467–490, June 1993.

[87] B. Gottschalk, E. Cascio, J. Daartz et al. On the nuclear halo of a proton pencil beam stopping in water. *Physics in medicine and biology*, 60:5627–5654, 07 2015.

[88] M. Soukup, M. Fippel and M. Alber. A pencil beam algorithm for intensity modulated proton therapy derived from monte carlo simulations. *Physics in Medicine and Biology*, 50(21):5089–5104, oct 2005.

[89] A. Ferrari, P. R. Sala, A. Fassò et al. *FLUKA: A multi-particle transport code (program version 2005)*. CERN Yellow Reports: Monographs. CERN, Geneva, 2005.

[90] H. Paganetti. Monte carlo simulations. In H. Paganetti, editor, *Proton Therapy Physics*, pages 265–303. CRC Press, Taylor & Francis Group, Boca Raton London New York, 2012.

[91] M. J. Berger. Monte Carlo calculation of the penetration and diffusion of fast charged particles, 1963.

[92] M. J. Berger and S. M. Seltzer. Stopping powers and ranges of electrons and positrons. Unknown, August 1982.

[93] J. Sorriaux, M. Testa, H. Paganetti et al. Experimental assessment of proton dose calculation accuracy in inhomogeneous media. *Physica Medica*, 38:10–15, 2017.

[94] P. Taylor, S. Kry and D. Followill. Pencil beam algorithms are unsuitable for proton dose calculations in lung. *International Journal of Radiation Oncology*Biology*Physics*, 99, 06 2017.

[95] J. Saini, D. Maes, A. Egan et al. Dosimetric evaluation of a commercial proton spot scanning monte-carlo dose algorithm: Comparisons against measurements and simulations. *Physics in Medicine and Biology*, 62, 07 2017.

[96] D. Maes, J. Saini, J. Zeng et al. Advanced proton beam dosimetry part ii: Monte carlo vs . pencil beam-based planning for lung cancer. *Translational Lung Cancer Research*, 7(2), 2018.

[97] B. Emami, J. Lyman, A. Brown et al. Tolerance of normal tissue to therapeutic irradiation. *International Journal of Radiation Oncology*Biology*Physics*, 21(1):109–122, 1991. Three-Dimensional Photon Treatment Planning Report of the Collaborative Working Group on the Evaluation of Treatment Planning for External Photon Beam Radiotherapy.

[98] L. B. Marks, E. D. Yorke, A. Jackson et al. Use of normal tissue complication probability models in the clinic. *International Journal of Radiation Oncology*Biology*Physics*, 76(3, Supplement):S10–S19, 2010. Quantitative Analyses of Normal Tissue Effects in the Clinic.

[99] S. M. Bentzen, L. S. Constine, J. O. Deasy et al. Quantitative analyses of normal tissue effects in the clinic (quantec): An introduction to the scientific issues. *International Journal of Radiation Oncology*Biology*Physics*, 76(3, Supplement):S3–S9, 2010. Quantitative Analyses of Normal Tissue Effects in the Clinic.

[100] RaySearch Laboratories AB. Raystation 7 user manual rsl-d-rs-7.0-usm-en-1.0-2017-12-08, 2017.

[101] IBA Dosimetry GmbH. Product catalog product-catalog-rt-br-e_rev.1_1020_2, 2020.

[102] IBA Dosimetry GmbH. PPC05 Ionization Chamber User's Guide P-PPC05-510-001 01, 2008.

[103] International Electrotechnical Commission (IEC). *Medical electrical equipment –Dosimeters withionization chambers as used in radiotherapy)*. International Electrotechnical Commission (IEC), Geneva, 3.1 edition, 2016.

[104] IBA Dosimetry GmbH. Dose 1 high performance reference class electrometer rt-br-e-dose1 rev.1 0211, 2011.

[105] R. Loevinger. Extrapolation chamber for the measurement of beta sources. *Review of Scientific Instruments*, 24(10):907–914, 1953.

[106] PTW-FREIBURG Physikalisch-Technische Werkstätten Dr. Pychlau GmbH. Beschreibung der ptw-extrapolationskammer 23391.

[107] J. Böhm and U. Schneider. Review of extrapolation chamber measurements of beta rays and low energy x rays. *Radiation Protection Dosimetry*, 14:193–198, 1986.

[108] S. C. Klevenhagen. Determination of absorbed dose in high-energy electron and photon radiation by means of an uncalibrated ionization chamber. *Physics in Medicine and Biology*, 36(2):239–253, feb 1991.

[109] C. E. Zankowski and E. B. Podgorsak. Calibration of photon and electron beams with an extrapolation chamber. *Medical Physics*, 24(4):497–503, 1997.

[110] J. B. Smathers, V. A. Otte, A. R. Smith et al. Composition of a-150 tissue-equivalent plastic. *Medical Physics*, 4(1):74–77, 1977.

[111] Commission of the European Communities EURATOM. *RADIATION PROTECTION PROGRAMME PROGRESS REPORT 1990-91 EUR 14927 DE/EN/FR*. Office for Officiai Publications of the European Communitie Luxembourg, 1993.

[112] PTW-FREIBURG Physikalisch-Technische Werkstätten Dr. Pychlau GmbH. Gebrauchsanweisung tandem t10011, t10015 und t10016 tandem xdr t10037, t10038 und t10039 d562.151.00/06 de, 2013.

[113] PTW-FREIBURG Physikalisch-Technische Werkstätten Dr. Pychlau GmbH. Detectors including codes of practice d165.229.00/12, 2019.

[114] PTW-FREIBURG Physikalisch-Technische Werkstätten Dr. Pychlau GmbH. Gebrauchsanweisung tansoft d573.151.00/04 de, 2009.

[115] IBA Dosimetry GmbH. Giraffe&zebra_rev.1_1119_e i, 2019.

[116] G. Mazza, R. Cirio, M. Donetti et al. A 64-channel wide dynamic range charge measurement asic for strip and pixel ionization detectors. *Nuclear Science, IEEE Transactions on*, 52:847 – 853, 09 2005.

[117] C. Bäumer, B. Koska, J. Lambert et al. Evaluation of detectors for acquisition of pristine depth-dose curves in pencil beam scanning. *Journal of Applied Clinical Medical Physics*, 16(6):151–163, 2015.

[118] S. Dhanesar, N. Sahoo, M. Kerr et al. Quality assurance of proton beams using a multilayer ionization chamber system. *Medical Physics*, 40(9):092102, 2013.

[119] A. Vai, A. Mirandola, G. Magro et al. Characterization of a mlic detector for qa in scanned proton and carbon ion beams. *International Journal of Particle Therapy*, 6:50–59, 09 2019.

[120] IBA Dosimetry GmbH. Zebra, 2021. URL `https://www.iba-dosimetry.com/product/zebra/`, [(Last accessed: 3. June 2021].

[121] IBA Dosimetry GmbH. Omnipro-incline version 1.1 user's guide p-08-007-510-001 08, 2015.

[122] STANDARD IMAGING INC. EXRADIN DETECTORS, 2018.

[123] STANDARD IMAGING INC. EXRADIN ION CHAMBERS Thimble Ionization Chambers User Manual, 2006.

[124] L. Mertens. *Messung der in der Protonentherapie auftretenden Hautdosis mit Thermolumineszenzdosimetern*. Master's thesis, TU Dortmund, 2018.

[125] M. Heiny. *High temperature thermoluminescence peaks – Influence on the albedo principle for personal dosimetry and benefits for the new TL-DOS neutron dosemeter*. Ph.D. thesis, TU Dortmund, 2020.

[126] Materialprüfungsamt Nordrhein-Westfalen. Tl-dos-ticker - news zum kommenden dosimetersystem. URL `https://www.mpanrw.de/dienstleistungen/strahlenschutz/informationsportal/tl-dos-ticker`, [Last accessed: 28. September 2021].

[127] S. F. Kry, P. Alvarez, J. E. Cygler et al. Aapm tg 191: Clinical use of luminescent dosimeters: Tlds and oslds. *Medical Physics*, 47(2):e19–e51, 2020.

[128] Radcard - TLD Dosemeters. Lif:mg,ti thermoluminescent phosphor & pellets. URL `http://www.radcard.pl/det/mtsn.html`, [Last accessed: 28. September 2021].

[129] J. E. Martin. *Neutrons*, chapter 14, pages 571–606. John Wiley & Sons, Ltd, 2013.

[130] J. Walbersloh and F. Busch. A thin-layer LiF thermoluminescence dosemeter system with fast readout for the use in personal dosimetry services. *Radiation Protection Dosimetry*, 170(1-4):191–194, 09 2016.

[131] P. M. Ostwald, T. Kron, C. S. Hamilton et al. Clinical use of carbon-loaded thermoluminescent dosimeters for skin dose determination. *International Journal of Radiation Oncology*Biology*Physics*, 33(4):943–950, 1995.

[132] T. Kron, A. Elliot, T. Wong et al. X-ray surface dose measurements using tld extrapolation. *Medical Physics*, 20(3):703–711, 1993.

[133] J.-P. Lin, T.-C. Chu, S.-Y. Lin et al. Skin dose measurement by using ultra-thin tlds. *Applied Radiation and Isotopes*, 55(3):383–391, 2001.

[134] B. Shachar and Y. Horowitz. Dosimetric Characterisation of the High Temperature Peaks of LiF:Mg,Ti and CaF2:Tm Using Computerised Glow Curve Deconvolution. *Radiation Protection Dosimetry*, 22(2):87–96, 02 1988.

[135] K. Kröninger, F. Mentzel, R. Theinert et al. A machine learning approach to glow curve analysis. *Radiation Measurements*, 125:34–39, 2019.

[136] International Commission on Radiation Units and Measurements (ICRU). Report 16 Linear Energy Transfer, 1970.

[137] S. Devic, J. Seuntjens, W. Abdel-Rahman et al. Accurate skin dose measurements using radiochromic film in clinical applications. *Medical Physics*, 33(4):1116–1124, 2006.

[138] U. Akbas, N. D. Kesen, C. Koksal et al. Surface and buildup region dose measurements with Markus parallel-plate ionization chamber, Gafchromic EBT3 film and MOSFET detector for high-energy photon beams. *Adv. High Energy Phys.*, 2016:8361028, 2016.

[139] M. J. Butson, T. Cheung and P. K. N. Yu. Megavoltage x-ray skin dose variation with an angle using grid carbon fibre couch tops. *Physics in Medicine Biology*, 52(20):N485, oct 2007.

[140] Ashland Inc. Ebt3 atomic composition. E-Mail from 03.03.2017 with Resat Aydin (Ashland).

[141] Ashland Inc. Ebt3 specification and user guide. URL `http://www.gafchromic.com/documents/EBT3$_$Specifications.pdf`, [Last accessed: 24. June 2021)].

[142] Ashland Inc. Gafchromic dosimetry tools, 2016. URL `http://www.gafchromic.com/documents/PC-11802$_$Gafchromic$_$EBT3.pdf`, [Last accessed: 24. June 2021].

[143] Ashland Inc. Efficient protocols for accurate radiochromic film calibration and dosimetry. URL `http://www.gafchromic.com/documents/Efficient%20Protocols%20for%20Calibration%20and%20Dosimetry.pdf`, [Last accessed: 24. June 2021].

[144] Lewis, David F. and Micke, Andre and Yu, Xiang. New performance standard: Multi-channel and one-scan radiochromic film dosimetry, 2012. URL `http://www.gafchromic.com/documents/Lewis$_$Micke$_$Yu$_$New$_$Performance$_$Standard$_$Multi-channel$_$and$_$One-scan$_$Radiochromic$_$Film$_$Dosimetry$_$20120615.pdf`, [Last accessed: 12. September 2021].

[145] Epson. Epson expression 10000xl din a3-grafikscanner. URL `https://www.epson.de/produkte/scanner/business/epson-expression-10000xl/p/313`, [Last accessed: 24. August 2022].

[146] Ashland Inc. Gafchromic hd-v2 film specification and user guide. URL `http://www.gafchromic.com/documents/gafchromic-hdv2.pdf`, [Last accessed: 24. June 2021].

[147] O. E. Belhaj, H. Boukhal and E. M. Chakir. Monte carlo and medical physics. In A. A. Jaoudé, editor, *The Monte Carlo Methods*, chapter 5. IntechOpen, Rijeka, 2022.

[148] A. F. Bielajew. Fundamentals of the monte carlo method for neutral and charged particle transport, 2020.

[149] F. Berumen, Y. Ma, J. Ramos-Méndez et al. Validation of the topas monte carlo toolkit for hdr brachytherapy simulations. *Brachytherapy*, 20(4), 4 2021.

[150] M. B. Hahn and J. M. Zutta Villate. Combined cell and nanoparticle models for topas to study radiation dose enhancement in cell organelles. *Scientific reports*, 11, 2021.

[151] J. Wu, Y. Xie, L. Wang et al. Monte carlo simulations of energy deposition and dna damage using topas-nbio. *Physics in Medicine & Biology*, 65, 09 2020.

[152] W. Huo, T. Zwart, J. Cooley et al. A single detector energy-resolved proton radiography system: a proof of principle study by monte carlo simulations. *Physics in Medicine & Biology*, 64(2):025016, jan 2019.

[153] C. A. S. Dunning and M. Bazalova-Carter. Optimization of a table-top x-ray fluorescence computed tomography (XFCT) system. *Physics in Medicine & Biology*, 63(23):235013, nov 2018.

[154] H. Liu, L. Zhang, C. Zhi et al. A preliminary monte carlo study for the treatment head of a carbon-ion radiotherapy facility using topas. *EPJ Web of Conferences*, 153, 01 2017.

[155] B. Faddegon, J. Ramos-Méndez, J. Schuemann et al. The topas tool for particle simulation, a monte carlo simulation tool for physics, biology and clinical research. *Physica Medica*, 72:114–121, 2020.

[156] S. Agostinelli, J. Allison, K. Amako et al. Geant4—a simulation toolkit. *Nuclear Instruments and Methods in Physics Research Section A: Accelerators, Spectrometers, Detectors and Associated Equipment*, 506(3):250–303, 2003.

[157] Perl, J. et al. Topas documentation release 3.1, 2018.

[158] M. Testa, J. Schümann, H.-M. Lu et al. Experimental validation of the topas monte carlo system for passive scattering proton therapy. *Medical Physics*, 40(12):121719, 2013.

[159] M. Behring. *Monte-Carlo-Simulationen der Pencil-Beam-Scanning-Nozzle der Protonentherapieanlage des Westdeutschen Protonentherapiezentrums Essen.* Master's thesis, TU Dortmund, 2015.

[160] N. Verbeek. *Umsetzung Faraday Cup-basierter Dosimetrie im Nadelstrahlverfahren in der Protonentherapie.* Master's thesis, Heinrich Heine Universität Düsseldorf, 2017.

[161] IBA Dosimetry GmbH. Phantoms for absolute dosimetry rt-br-e-phantoms-for-adrev.20813, 2013.

[162] M.J. Berger, J.S. Coursey, M.A. Zucker2 and J. Chang. Stopping-power range tables for electrons, protons, and helium ions, 2015. URL `https://physics.nist.gov/cgi-bin/Star/compos.pl?refer=ap&matno=222`, [Last accessed: 10. October 2022].

[163] R. Zhang and W. D. Newhauser. Calculation of water equivalent thickness of materials of arbitrary density, elemental composition and thickness in proton beam irradiation. *Physics in Medicine Biology*, 54(6):1383, feb 2009.

[164] D. Lewis, A. Micke, X. Yu et al. An efficient protocol for radiochromic film dosimetry combining calibration and measurement in a single scan. *Medical Physics*, 39(10):6339–6350, 2012.

[165] L. Menegotti, A. Delana and A. Martignano. Radiochromic film dosimetry with flatbed scanners: A fast and accurate method for dose calibration and uniformity correction with single film exposure. *Medical Physics*, 35(7Part1):3078–3085, 2008.

[166] S. Reinhardt, M. Hillbrand, J. Wilkens et al. Comparison of Gafchromic EBT2 and EBT3 films for clinical photon and proton beams. *Medical physics*, 39:5257–62, 08 2012.

[167] L. Paelinck, W. D. Neve and C. D. Wagter. Precautions and strategies in using a commercial flatbed scanner for radiochromic film dosimetry. *Physics in Medicine and Biology*, 52(1):231–242, dec 2006.

[168] J. Sorriaux, A. Kacperek, S. Rossomme et al. Evaluation of Gafchromic (R) EBT3 films characteristics in therapy photon, electron and proton beams. *Physica medica : PM : an international journal devoted to the applications of physics to medicine and biology : official journal of the Italian Association of Biomedical Physics (AIFB)*, 29, 10 2012.

[169] S. Saur and J. Frengen. Gafchromic ebt film dosimetry with flatbed ccd scanner: A novel background correction method and full dose uncertainty analysis. *Medical Physics*, 35(7Part1):3094–3101, 2008.

[170] W. Hanson and W. Grant. Use of axiliary collimating devices in the treatment for breast cancer with 60co teletherapy units. ii. dose to the skin. *American Journal of Roentgenology*, 127(4):653–657, 1976.

[171] B. J. Gerbi and F. M. Khan. Measurement of dose in the buildup region using fixed-separation plane-parallel ionization chambers. *Medical Physics*, 17(1):17–26, 1990.

[172] P. R. T. L. Camargo, H. Yoriyaz, P. T. D. Siqueira et al. Validation of the modeling of a commercial extrapolation chamber using the monte carlo technique.

[173] Standard Imaging Inc. EXRADIN Parallel Plate Ion Chambers User Manual, 2002.

[174] PTW Freiburg GmbH. Detectors for Ionizing Radiation, 2022.

[175] Geant4Collaboration. Geant4: Physics reference manual version: Geant4 10.3 (9 december 2016), 2016. URL `https://geant4-userdoc.web.cern.ch/UsersGuides/PhysicsReferenceManual/BackupVersions/V10.3/fo/PhysicsReferenceManual.pdf`, [Last accessed: 20. October 2022].

[176] J. Wulff, K.-S. Baumann, N. Verbeek et al. Topas/geant4 configuration for ionization chamber calculations in proton beams. *Physics in Medicine Biology*, 63(11):115013, jun 2018.

[177] M. J. Butson, P. K. N. Yu and P. E. Metcalfe. Extrapolated surface dose measurements with radiochromic film. *Medical Physics*, 26(3):485–488, 1999.

[178] C. Bäumer, B. Ackermann, M. Hillbrand et al. Dosimetry intercomparison of four proton therapy institutions in germany employing spot scanning. *Zeitschrift für Medizinische Physik*, 27(2):80–85, 2017.

[179] C. Bäumer, C. M. Bäcker, M. Gerhardt et al. Measurement of absolute activation cross sections from carbon and aluminum for proton therapy. *Nuclear Instruments and Methods in Physics Research Section B: Beam Interactions with Materials and Atoms*, 440:75–81, 2019.

[180] J. C. for Guides in Metrology. Jcgm 100: Evaluation of measurement data - guide to the expression of uncertainty in measurement. Technical report, JCGM, 2008.

[181] A. Micke, D. F. Lewis and X. Yu. Multichannel film dosimetry with nonuniformity correction. *Medical Physics*, 38(5):2523–2534, 2011.

[182] C. Bäumer, C. Fuentes, M. Janson et al. Stereotactical fields applied in proton spot scanning mode with range shifter and collimating aperture. *Physics in Medicine Biology*, 64(15):155003, aug 2019.

[183] B. Arjomandy, N. Sahoo, J. Cox et al. Comparison of surface doses from spot scanning and passively scattered proton therapy beams. *Physics in Medicine Biology*, 54(14):N295, jun 2009.

[184] J. Daartz, M. Engelsman, H. Paganetti et al. Field size dependence of the output factor in passively scattered proton therapy: Influence of range, modulation, air gap, and machine settings. *Medical Physics*, 36(7):3205–3210, 2009.

[185] U. Schneider and R. Hälg. The impact of neutrons in clinical proton therapy. *Frontiers in Oncology*, 5, 2015.

[186] R. A. Hälg and U. Schneider. Neutron dose and its measurement in proton therapy—current state of knowledge. *The British Journal of Radiology*, 93(1107), 2020.

[187] N. Salvo, E. Barnes, J. van Draanen et al. Prophylaxis and management of acute radiation-induced skin reactions: A systematic review of the literature. *Current Oncology*, 17(4):94–112, 2010.

[188] S. Kumar, E. Juresic, M. Barton et al. Management of skin toxicity during radiation therapy: A review of the evidence. *Journal of Medical Imaging and Radiation Oncology*, 54(3):264–279, 2010.

[189] E. G. Russi, F. Moretto, M. Rampino et al. Acute skin toxicity management in head and neck cancer patients treated with radiotherapy and chemotherapy or egfr inhibitors: Literature review and consensus. *Critical Reviews in Oncology/Hematology*, 96(1):167–182, 2015.

[190] C. Yee, K. Wang, R. Asthana et al. Radiation-induced skin toxicity in breast cancer patients: A systematic review of randomized trials. *Clinical Breast Cancer*, 18(5):e825–e840, 2018.

[191] B. D. Lawenda, H. M. Gagne, D. P. Gierga et al. Permanent alopecia after cranial irradiation: Dose–response relationship. *International Journal of Radiation Oncology*Biology*Physics*, 60(3):879–887, 2004.

[192] V. Moskvin, F. Lasley, G. Ray et al. Acute skin toxicity associated with proton beam therapy in spine and brain patients. *Journal of Radiation Oncology*, 3:1–9, 06 2013.

[193] A. Dutz, A. Lühr, L. Agolli et al. Development and validation of ntcp models for acute side-effects resulting from proton beam therapy of brain tumours. *Radiotherapy and Oncology*, 130:164–171, 2019.

[194] P. Pisciotta, A. Costantino, F. P. Cammarata et al. Evaluation of proton beam radiation-induced skin injury in a murine model using a clinical sobp. *PLOS ONE*, 15(5):1–18, 05 2020.

[195] G. Palma, A. Taffelli, F. Fellin et al. Modelling the risk of radiation induced alopecia in brain tumor patients treated with scanned proton beams. *Radiotherapy and Oncology*, 144:127–134, 2020.

[196] C. M. DeCesaris, S. R. Rice, S. M. Bentzen et al. Quantification of acute skin toxicities in patients with breast cancer undergoing adjuvant proton versus photon radiation therapy: A single institutional experience. *International Journal of Radiation Oncology*Biology*Physics*, 104(5):1084–1090, 2019.

[197] S. Gaito, A. Abravan, J. Richardson et al. Skin toxicity profile of photon radiotherapy versus proton beam therapy in paediatric and young adult patients with sarcomas. *Clinical Oncology*, 33(8):507–516, 2021.

[198] ICRP Report No. 59. The biological basis for dose limitation in the skin, 1992.

[199] M. Wang, L. Zhang, J. Zheng et al. Investigating the effects of a range shifter on skin dose in proton therapy. *Nuclear Engineering and Technology*, 55(1):215–221, 2023.

[200] L. J. Radvansky, M. B. Pace and A. Siddiqui. Prevention and management of radiation-induced dermatitis, mucositis, and xerostomia. *American Journal of Health-System Pharmacy*, 70(12):1025–1032, 06 2013.

[201] K. Morgan. Radiotherapy-induced skin reactions: prevention and cure. *British Journal of Nursing*, 23(Sup16):S24–S32, 2014.

# Danksagung

In diesem Abschnitt möchte ich bei allen bedanken, die mich während meiner Promotion in unterschiedlichsten Formen unterstützt haben.
Zunächst möchte ich mich bei Prof. Dr. Kevin Kröninger für die Aufnahme als Dokterand in seiner Arbeitsgruppe bedanken. Weiterhin möchte ich ihm für die ganze organisatorische Unterstützung und den letzen Gesprächen danken. Weiterhin wurde mir der Zugang zum Rechencluster der AG Kröninger für die Monte Carlo Simulationen gewährt. Danke an das tolle und hilfsbereite E4 Team.
Einen sehr großen Dank möchte ich an PD Dr. Christian Bäumer aussprechen, der mir die Möglichkeit gegebenen hatte an diesem tollen Projekt zu arbeiten. Vielen Dank für die Unterstützung, das offene Ohr, den Diskussionen und der gemeinsamen Zeit am WPE. Ich konnte so einiges in dieser Zeit von ihm lernen.
Zunächst möchte ich mich bei Prof. Dr. Beate Timmermann für die Möglichkeit der Forschung am WPE bedanken. Außerdem ein Dankeschön an das komplette Team der Physik und der feinmechanischen Werkstatt des WPE. Besonders hervorheben möchte ich Dr. Jörg Wulff, der ebenfalls für rege Diskussionen und kritischen Anmerkungen in den Publikationen stets zur Verfügung stand. Weiterhin möchte ich mich bei Dr. Nico Verbeek für die gemeinsame Master- und Doktorandenphase danken, bei der wir viel Spaß hatten und uns über TOPAS-Simulationen austauschen konnten. Dr. Paul-Heinz Kramer und Markus Lemke möchte ich für die vielen gemeinsamen Bürostunden danken. Besonders bei Markus, da die Hautdosisuntersuchung seine ursprüngliche Promotionsidee war und von mir realisiert wurde. Dr. Carina Wellers (ehemals Behrends) möchte ich für den Support nach dem Verlassen des WPE danken. Ihr und Dr. Robert Theinert möchte ich für die Unterstützung beim Korrekturlesen danken.
Weiterhin möchte ich Lena Mertens und Alina Landmann für die Zusammenarbeit in Form ihrer Master- und Bachelorthesis danken. An dieser Stelle danke ich Jörg Walbersloh für die Ausleihe der PTW Extrapolationskammer, die ein wesentlicher Teil dieser Arbeit geworden ist. Ich war im MPA immer willkommen und durfte dort nach Lenas Masterarbeit weiterhin TLD Auswertungen durchführen. Danke an dieser Stelle an Dr. Myriam Theinert (ehemals Heiny) für die Unterstützung mit dem TL-Dos.
Zu guter Letzt bedanke ich mich bei meinen Eltern und meinem Bruder, die mich über die Jahre zu jeder Zeit unterstützt hatten. Katharina, dir möchte ich das größte Dankeschön

aussprechen, da du für mich in dieser langen Phase immer an meiner Seite standest und sehr viel Geduld mitgebracht hattest. Das ist nicht selbstverständlich.